

Search for Truth in the $e\mu$ channel at DØ

A Dissertation Presented

by

James Herbert Cochran, Jr.

to

The Graduate School

in Partial Fulfillment of the Requirements

for the Degree of

Doctor of Philosophy

in

Physics

State University of New York

at

Stony Brook

December 1993

State University of New York
at Stony Brook

The Graduate School

James Herbert Cochran, Jr.

We, the dissertation committee for the above candidate for the Doctor of Philosophy degree, hereby recommend acceptance of the dissertation.

dissertation director
Professor Michael Rijssenbeek
Department of Physics

chairman of defense
Professor Guido Finocchiaro
Department of Physics

committee member
Professor George Sterman
Department of Physics

outside member
Professor Stephen J. Wimpenny
Department of Physics
University of California at Riverside

This dissertation is accepted by the Graduate School.

Graduate School

Abstract of the Dissertation
Search for Truth in the $e\mu$ channel at D \emptyset

by

James Herbert Cochran, Jr.

Doctor of Philosophy

in

Physics

State University of New York at Stony Brook

1993

A search for standard model $t\bar{t} \rightarrow e\mu + X$ events in $p\bar{p}$ collisions at $\sqrt{s} = 1.8$ TeV is presented. Results are based on an integrated luminosity of 15.2 ± 1.8 pb $^{-1}$ acquired by the D \emptyset detector at Fermilab during the 1992-1993 collider run. One candidate event was found and a corresponding upper limit on the cross section for $t\bar{t}$ production thus obtained. This limit, together with the theoretical cross section [42] leads to a lower limit on the top mass of 92 GeV/ c^2 at the 95% confidence level.

This dissertation is dedicated to my Father and to the memory of my Mother.

Contents

List of Figures	xiii
List of Tables	xiv
Acknowledgements	xv
1 Introduction	1
1.1 Overview of Particle Physics	3
1.2 Current State of Particle Physics	10
1.2.1 Theoretical Activity	11
1.2.2 Recent Experiments	11
1.2.3 Future Experiments	12
1.3 The Top Quark	13
2 The Tevatron	21
2.1 History	21
2.2 Principles of Operation	23
2.3 Main Injector Upgrade	27

3 The DØ Detector	28
3.1 History	28
3.2 Physics Studied at DØ	30
3.3 Design Principles of Detectors at Colliding Beams	31
3.4 Tracking	32
3.4.1 Principles of operation of wire (drift) chambers	34
3.4.2 Vertex chamber	35
3.4.3 CDC	37
3.4.4 FDC	43
3.4.5 TRD	44
3.4.6 Electronics	47
3.5 Calorimeter	47
3.5.1 Central Calorimeter	53
3.5.2 End Calorimeter	54
3.5.3 ICD and massless gap detectors	56
3.6 Muon System	58
3.7 DAQ/Trigger System	63
3.7.1 LØ	63
3.7.2 L1	65
3.7.3 L2	67
3.8 Offline Reconstruction - DØRECO	69

4 TOP-LEPTONS: the analysis package	78
4.1 Overview	78
4.2 Particle ID	80
4.2.1 Electron/Photon	81
4.2.2 Muon	83
4.2.3 Jets	85
4.2.4 Determination of \cancel{E}_T	86
4.3 Corrections	87
4.3.1 Data	87
4.3.2 Monte Carlo	90
5 Background vs Signal: What do we expect?	91
5.1 Monte Carlo Studies	92
5.1.1 Event Generators - How to simulate the Physics	94
5.1.2 GEANT - How to simulate the Detector	98
5.1.3 TRIGSIM - How to simulate the Trigger	99
5.1.4 Further Refinements	100
5.1.5 Acceptance for $t\bar{t} \rightarrow e\mu$	103
5.1.6 Backgrounds from <i>real</i> physics processes (mc)	108
5.2 Instrumental Backgrounds (fakes)	113
5.2.1 Sources	113
5.2.2 Channels	117
5.2.3 The “fakes” spreadsheet	118
5.3 Summary	122

6 Analysis of Collider data	123
6.1 Data Sample	123
6.1.1 Integrated Luminosity	124
6.2 Triggers	126
6.3 Data Selection	126
6.3.1 Initial DST selection	127
6.3.2 STA selection	128
6.3.3 Cuts/Motivation	130
6.3.4 The Candidate - event 417	133
6.4 Expected number of Background events	143
6.5 Expected $t\bar{t} \rightarrow e\mu$ event yield	145
6.6 The Cross Section Limit	145
6.6.1 $e\mu$ only	146
6.6.2 Combining channels	148
6.6.3 What can we say about a limit on M_t	150
7 Conclusion	153
A Cross Sections and Branching Ratios	156
A.1 Total Cross Sections: σ_{tot}	156
A.2 Branching Ratios: $(BR)_i$	158
A.3 Relevant Cross Sections: $\sigma_i = \sigma_{tot} \cdot (BR)_i$	160
Bibliography	161

List of Figures

1.1	The four fundamental types of force, between a typical pair of particles	4
1.2	Fraction of $q\bar{q}$ (long dashed line) and gg (short dashed line) contribution to $t\bar{t}$ production (NLO) at the Tevatron	14
1.3	Lowest order Feynman diagrams for $t\bar{t}$ production	15
1.4	Higher order Feynman diagrams for $t\bar{t}$ production	16
1.5	Dependence $\sin^2\theta_W(M_Z^2)$ on M_t and M_H using the known value of M_Z . The two bands show the result of varying M_t , with M_H held fixed at the two values 100 and 1000 GeV/c^2 . The width of each band reflects the 1σ error in M_Z (circa 1989 - $M_Z = 91.150 \pm 0.030 \text{GeV}/c^2$, the current value is $M_Z = 91.173 \pm 0.020 \text{GeV}/c^2$)	17
1.6	Fraction of $t\bar{t}$ cross section into the various decay channels	20
2.1	The Fermilab Tevatron (collider mode)	24
3.1	The DØ detector	29
3.2	A Conceptual Detector	32
3.3	DØ Tracking Chambers	33

3.4	End view of one quadrant of the vertex chamber	35
3.5	Plan view of the ends of the vertex chamber showing the active chamber region, the support structure, and the electronics feedthrough bulkhead	37
3.6	End view of one “3/32”nd of the CDC	39
3.7	CDC module	40
3.8	FDC chambers (one side)	44
3.9	Schematic view of a TRD	46
3.10	Tracking Electronics readout path and controls	48
3.11	Schematic of DØ Calorimeter cell	50
3.12	DØ Calorimeter	54
3.13	Side view of the CC and EC	56
3.14	Cross Section view of the DØ Muon system	58
3.15	Extruded aluminum section from which the “B” and “C” layer PDT chambers are constructed. The “A” layer chamber extrusions are similar but have 4 cells instead of 3.	60
3.16	Variation in the detector thickness (in interaction lengths) as a function of polar angle	61
3.17	Perspective view of the CF toroid	62
3.18	Simplified View of DAQ/Trigger System	64
3.19	Level 1 processing stages	66
3.20	χ^2 distribution for test beam electrons (unshaded), test beam pions (shaded), and electrons from W ’s (dots)	71

3.21 Calorimeter \cancel{E}_T resolution function for the D \emptyset detector for QCD dijet data	76
4.1 D \emptyset jet energy correction factor for 0.7 cone jets at $ \eta = 0.0$ and $ \eta = 2.5$	89
5.1 Schematic illustration of a $q\bar{q}$ collision	94
5.2 Efficiency as a function of M_t for standard contribution to $e\mu$ production (errors are RMS statistical plus systematic)	107
5.3 $e\mu$ Physics background events in 15.2 pb^{-1}	111
5.4 Partial view of the Fake's Spreadsheet	119
5.5 $e\mu$ fake background events in 15.2 pb^{-1}	120
6.1 P_T^e vs P_T^μ [top] and $M_{e\mu}$ vs \cancel{E}_T [bottom] for data (15.2 pb^{-1}) [left] and $t\bar{t} \rightarrow e\mu$ Monte Carlo ($M_t = 140 \text{ GeV}/c^2$, 2416 pb^{-1}) [right]; cuts: P_T^e, P_T^μ , and id (58 events)	134
6.2 P_T^e vs P_T^μ [top] and $M_{e\mu}$ vs \cancel{E}_T [bottom] for data (15.2 pb^{-1}) [left] and $t\bar{t} \rightarrow e\mu$ Monte Carlo ($M_t = 140 \text{ GeV}/c^2$, 2416 pb^{-1}) [right]; cuts: P_T^e, P_T^μ , and Initial μ isolation (30 events)	135
6.3 P_T^e vs P_T^μ [top] and $M_{e\mu}$ vs \cancel{E}_T [bottom] for data (15.2 pb^{-1}) [left] and $t\bar{t} \rightarrow e\mu$ Monte Carlo ($M_t = 140 \text{ GeV}/c^2$, 2416 pb^{-1}) [right]; cuts: P_T^e, P_T^μ , Initial μ isolation, and Secondary μ isolation (27 events)	136

6.4 P_T^e vs P_T^μ [top] and $M_{e\mu}$ vs \cancel{E}_T [bottom] for data (15.2 pb^{-1}) [left] and $t\bar{t} \rightarrow e\mu$ Monte Carlo ($M_t = 140 \text{ GeV}/c^2$, 2416 pb^{-1}) [right]; cuts: P_T^e, P_T^μ, μ isolation, and \cancel{E}_T (Calorimeter/ICD/masslessGap) (15 events)	137
6.5 P_T^e vs P_T^μ [top] and $M_{e\mu}$ vs \cancel{E}_T [bottom] for data (15.2 pb^{-1}) [left] and $t\bar{t} \rightarrow e\mu$ Monte Carlo ($M_t = 140 \text{ GeV}/c^2$, 2416 pb^{-1}) [right]; cuts: P_T^e, P_T^μ, μ isolation, \cancel{E}_T (Calorimeter/ICD/masslessGap), and \cancel{E}_T (μ corrected) (8 events)	138
6.6 P_T^e vs P_T^μ [top] and $M_{e\mu}$ vs \cancel{E}_T [bottom] for data (15.2 pb^{-1}) [left] and $t\bar{t} \rightarrow e\mu$ Monte Carlo ($M_t = 140 \text{ GeV}/c^2$, 2416 pb^{-1}) [right]; cuts: P_T^e, P_T^μ, μ isolation, \cancel{E}_T , and small angle brem (5 events)	139
6.7 Event 417 side view	140
6.8 Event 417 end view	140
6.9 Event 417 Lego plot	141
6.10 Various distributions of selection variables for good electrons from the DØ $W \rightarrow e\nu_e$ sample; arrows indicate the values for the electron in event 417	144
6.11 Expected number of $t\bar{t} \rightarrow e\mu$ signal events as a function of M_t and total expected background	147
6.12 DØ cross section upper limit (95 % CL) and Laenen <i>et al.</i> cross section vs $M_t - e\mu$ channel only	151
6.13 DØ cross section upper limit (95 % CL) and Laenen <i>et al.</i> cross section vs $M_t - e\mu, ee, e + \text{jets}$, and $\mu + \text{jets}$ channels combined	152

List of Tables

1.1	“Fundamental” particles of the Minimal Standard Model	9
1.2	Top width and lifetime for $M_t = 100, 150, \& 200 \text{ GeV}/c^2$	19
1.3	Decay modes of W^+W^-	19
3.1	Vertex Chamber Parameters	38
3.2	Central Drift Chamber Parameters	41
3.3	Forward Drift Chamber Parameters	45
3.4	Central Calorimeter Parameters	55
3.5	End Calorimeter Parameters	57
3.6	Muon System Parameters	61
4.1	Simplified schematic view of TOP-LEPTONS	81
5.1	Efficiencies for standard $t\bar{t} \rightarrow e\mu$ production (errors: statistical, systematic)	106
5.2	$e\mu$ Physics backgrounds (errors on cross section are systematic; errors on number of events are systematic and luminosity)	110

5.3 $e\mu$ fake backgrounds ($X(e)$ and $Y(\mu)$ are fake electrons and fake muons respectively, $\tau(e)$ is a tau which fakes an electron (errors on cross section are systematic; errors on number of events are systematic and luminosity)	121
6.1 $e\mu$ triggers (level 1 and level 2) for run 1A	127
6.2 Final Analysis Cuts, cumulative effects	131
6.3 $t\bar{t} \rightarrow e\mu$ efficiency (errors: stat, sys) and expected event yield (errors: stat, sys, lum)	146
6.4 cross section limit from $e\mu$ channel only	148
6.5 Combined $e\mu$ and ee cross section upper limit	149
6.6 Combined $e\mu, ee, e + \text{jets}$, and $\mu + \text{jets}$ cross section upper limit	149
7.1 Run 1A analysis summary	154

Acknowledgements

I must begin by thanking my advisor Michael Rijssenbeek who, over these many years, has taught me much more than just physics. And to Steve Wimpenny I owe a great debt. Without his tireless efforts this work could not have been completed. I feel very honored to be a member of the “DØ family” and I wish to thank everyone in the collaboration for taking part in the creation of such a fine detector. Quite a few individuals, however, deserve special mention: Paul Grannis who has kept several hundred physicists properly focused for nearly 10 years; Guido Finocchiaro who has been an inspiration to us all; Marcel and Qizhong-Li Demarteau who have looked out for me; Kim Kwee Ng who has been a valued friend for so many years; Ties Behnke who I feel very fortunate to have worked with and who I consider a great friend; Vito Manzella who has helped me much more than he knows; Dave Schmid (formerly at the SSC) who produced all of our GEANT data without which this work would not be finished; Dave Hedin and Bob McCarthy who originally suggested this topic to me; Paul Russo who, as system manager for FNALDØ, is the most valuable person at DØ; Meenakshi Narain who has contributed so much to our analysis (in addition to being a good friend); Chris Klopfenstein,

Ray Hall, Thorsten Huehn, Brajesh Choudhary, Terry Heuring, Paul Rubinov, Peter Grudberg (a.k.a. slowpoke), Dhiman Chakraborty, Jae Yu, and Marc Paterno who have provided many stimulating discussions over the years (a special thanks goes to Jae for reading through of the formative scribblings that became this thesis); My housemates, Srini Rajagopalan and Scott Snyder who have made life in our house an “enriching” experience; Joey Thompson who has been like a brother in so many ways (and according to so many people); My parents who always encouraged me in everything I did; and last, but certainly not least, I owe lots of thanks and tozges to Masha who has put up with the search for “Mr. Quark” these last two years.

Chapter 1

Introduction

A certain philosopher used to hang about wherever children were at play. And whenever he saw a boy with a top, he would lie in wait. As soon as the top began to spin the philosopher went in pursuit and tried to catch it. He was not perturbed when the children noisily protested and tried to keep him away from their toy; so long as he could catch the top while it was spinning , he was happy, but only for a moment; then he threw it to the ground and walked away. For he believed that the understanding of any detail, that of a spinning top, for instance, was sufficient for the understanding of all things. For this reason he did not busy himself with great problems, it seemed to him uneconomical. Once the smallest detail was understood, then everything was understood, which was why he busied himself with the spinning top. And whenever preparations were being made for the spinning of the top, he hoped that this time it would succeed: as soon as the top began to spin and he was running breathlessly after it, the hope would turn to certainty, but when he held the silly piece of wood in his hand, he felt

nauseated. The screaming of the children, which hitherto he had not heard and which now suddenly pierced his ears, chased him away [1].

Franz Kafka

The “top” (also known as “truth”) quark is one of the few remaining pieces of the Standard Model yet to be observed. The Standard Model is the most complete theory of elementary particles to date and is briefly reviewed in the next section. This thesis presents the results of a search for the “top” quark in the $e\mu$ channel (this will be defined in section 1.3).

The outline of the thesis is as follows: Chapter 1 (this chapter) briefly reviews the elements of the Standard Model (past, present, and future) and discusses the importance of the top quark. Chapter 2 gives a very brief overview of the Tevatron. Chapter 3 describes the elements of the DØ detector. Chapter 4 covers the initial stages of the analysis, focusing primarily on particle id and corrected energy and momentum measurements. Chapter 5 describes studies (both Monte Carlo and data based) aimed at understanding $t\bar{t} \rightarrow e\mu$ acceptance and all the expected backgrounds. Chapter 6 covers the results of a search for $t\bar{t} \rightarrow e\mu$ events with the DØ detector based on the 1992-1993 collider run of the Tevatron ($15.2 \pm 1.8 \text{ pb}^{-1}$). Finally, Chapter 7 summarizes the earlier chapters and contains the conclusions of the search. The appendix lists the cross sections and branching ratios used in chapter 5.

1.1 Overview of Particle Physics

Particle Physics is concerned with the fundamental units of matter and the nature of the interactions between them. The interactions through which experimentally observed particles interact fall into four markedly different strengths: gravitational, electromagnetic, weak, and strong (see figure 1.1 [2]). Since the early part of this century gravitation has been described by the General Theory of Relativity [3]. Attempts to unify gravity with the other forces have so far been unsuccessful. In the 1860's Maxwell incorporated the observations of Faraday and others into one framework. This theory, which united the previously separate phenomena of electricity and magnetism is known as the "Classical electromagnetic theory" [4]. In the late 1920's and early 1930's Dirac, Heisenberg, Pauli and others extended Maxwell's theory to include the concepts of special relativity and quantum mechanics and thus produced the first theory of quantum electrodynamics (QED)[5]. Unfortunately, this theory only gave meaningful results when calculated to the lowest order in perturbation theory. Higher order terms gave divergent integrals (infinities). This problem was overcome in 1949 when Feynman, Schwinger, and Tomonaga introduced the concept of renormalization into QED. This allowed the divergent integrals to be absorbed into an infinite rescaling of the coupling constants and masses of the theory [6]. That is, when the results were written in terms of the "physical" couplings and masses, all the other physical quantities were finite and calculable. As Feynman wrote in 1983, the precision of QED is unprecedented [7]:

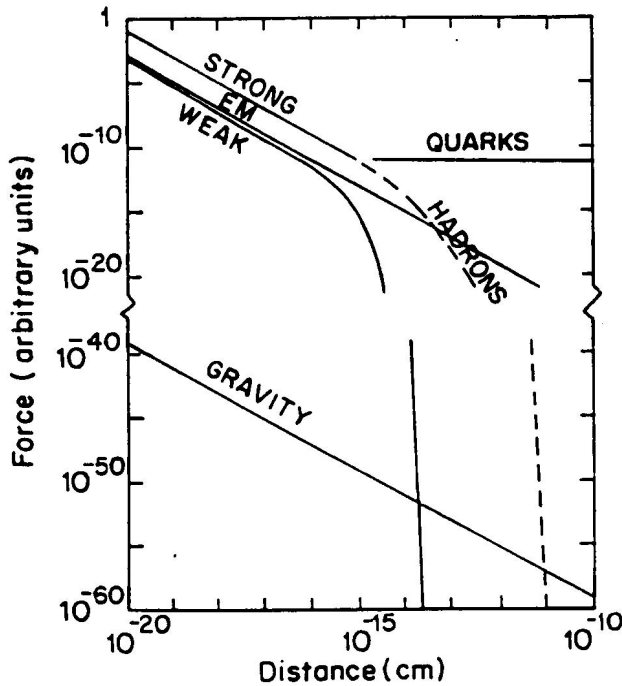


Figure 1.1: The four fundamental types of force, between a typical pair of particles

“Just to give you an idea of how the theory has been put through the wringer, I’ll give you some recent numbers: experiments have Dirac’s number [strength of interaction between magnetic moment of electron and light] at 1.00115965221 (with an uncertainty of about 4 in the last digit); the theory puts it at 1.00115965246 (with an uncertainty of about five times as much). To give you a feeling for the accuracy of these numbers, it comes out something like this: If you were to measure the distance from Los Angeles to New York to this accuracy, it would be exact to the thickness of a human hair. That’s how delicately quantum electrodynamics

has, in the past fifty years, been checked - both theoretically and experimentally. By the way, I have chosen only one number to show you. There are other things in quantum electrodynamics that have been measured with comparable accuracy, which also agree very well. Things have been checked at distance scales that range from one hundred times the size of the earth down to one-hundredth the size of an atomic nucleus.”

The first theory of the weak interactions was introduced by Fermi in 1934 to explain the phenomenon of β decay. His ideas were developed in close analogy to the theory of quantum electrodynamics as it was known at that time (i.e. that of Dirac, Heisenberg, and Pauli) [8]. Elementary particle interactions have been classified into five types: scalar(S), vector(V), tensor(T), pseudoscalar(P), and axial vector(A). These indicate the only ways that one particle’s wave function can transform into another during an interaction and satisfy the constraints of both relativity and quantum mechanics. QED, for example, is a vector(V) interaction, which implies that the transition from one wave function to another is always accompanied by the creation of a virtual particle, the photon, which has a spin of one and negative parity. Therefore, the photon is referred to as a vector particle. Similarly an axial vector(A) is associated with a spin one positive parity interaction and a scalar(S) interaction is associated with a particle of spin zero and positive parity [9]. Fermi’s theory of weak interactions, being very similar to QED was also a vector(V) interaction. However, a number of experiments could not be explained with

the Fermi theory (i.e. Gamow-Teller transitions). In 1956 Lee and Yang, following several experimental clues pointed out that there was no experimental evidence for or against parity conservation (i.e. equivalence of right and left) in weak interactions. Within a few months came the experimental confirmation that indeed parity is violated in weak interactions [10]. By mid 1957 many more experiments had been done and soon two groups of theorists, Marshak and Sudarshan, and Feynman and Gell-Mann proposed the V-A theory [11] [12]. This theory proved to be very successful and survives as the low energy description of weak interactions. However, for a number of reasons, it was clear that the theory was incomplete. By extending a theory of massless interacting vector particles developed by Yang and Mills in 1954, Glashow, Weinberg, and Salam (GWS) produced the “standard model of electroweak interactions” in the 1960’s which unified the weak and electromagnetic theories. This unification is based on the concept of spontaneous symmetry breaking. Within this theory the interactions are invariant under $SU(2)_L$ rotations of “weak isospin” and $U(1)_Y$ phase transformations of “weak hypercharge”(Y). An important feature of the parity violating nature of the theory (and of nature as well!) is that left-handed fermions (L) are treated differently from right-handed fermions. Glashow, Weinberg, and Salam used the Higgs mechanism to achieve this symmetry breaking although other, more complicated, approaches have also been proposed (e.g. technicolor [13]). The most dramatic experimental difference between the Glashow, Weinberg, Salam theory and that of Fermi was the prediction of neutral currents (i.e. $\nu_\mu e^- \rightarrow \nu_\mu e^-$). The experimental search for neutral currents did not begin until t’Hooft showed, in

the early 1970's, that the theory was renormalizable (necessary if infinities which arise in higher order calculations are to be avoided). Neutral currents were observed with the Gargamelle bubble chamber at CERN in mid 1973 [14]. More experiments provided additional circumstantial evidence and measured $\sin^2\theta_W$ (a parameterization of the ratio of the $U(1)$ and $SU(2)$ coupling constants), thus making it possible to predict the masses of the W and Z . In 1983 this prediction was shown to be consistent with the observation of the W and Z resonances (at essentially the predicted masses) by the UA1 and UA2 experiments at the CERN SPS collider [15] [16] [17] [18].

The earliest studies of the strong interaction indicated that the couplings between the particles were large. Therefore, perturbation theory, which worked so well for QED and weak processes could not be applied in a meaningful way. However, many years of experiments produced an extensive amount of data revealing many resonances (given the name hadrons) and regularities of cross section. The first attempt at a theory for the strong interactions came in 1935 when Yukawa proposed the existence of a massive particle which would carry the nuclear force in the same way as the photon carries the electromagnetic force. After many years of confusion, a resonance (hadron) with the mass Yukawa predicted was observed in 1947. By the early 1960's the number of observed resonances had exceeded one hundred and Gell-Mann and Zweig proposed a scheme whereby these resonances could be regarded as composites of more basic objects which they called "quarks" [19]. On the basis of deep inelastic ep scattering, reminiscent of Rutherford scattering, Bjorken and Feynman were able to conclude that the proton was composed of pointlike constituents,

thus giving some support to the “quark” hypothesis. In September of 1972 Gell-Mann presented an almost complete picture of the strong interactions. The quarks were held together by a gauge field whose quanta, gluons, are the vector bosons that mediate the strong force. Whereas the photon comes in only one type and is uncharged, the gluons come in eight types and are colored (color is the strong force analog to charge), like the quarks they interact with. Composite combinations of “up”, “down”, and “strange” quarks could explain all the hadrons discovered up to that time. Within this theory, interactions are invariant under $SU(3)_C$ rotations in “color” space. Gell-Mann called the new theory “quantum chromodynamics” (QCD) [20] [21]. However, the physics community was skeptical since a satisfactory explanation for the lack of observation of free quarks (bare color) was not given. Within a year 't Hooft, Gross and Wilczek, and Politzer were able to show that non-Abelian theories (which QCD was) possess the property of asymptotic freedom [22] [23]. This means, as explained by Politzer, “... that there is a unique class of forces that gets systematically weaker as the separation of the particles gets littler. That allows you to have quarks when they're close together to be weakly interacting, and as they get further apart, their influence on each other gets stronger instead of weaker”[24].

The great successes of the electroweak and QCD theories quickly led to a splicing together of these two theories into what is known as the “Standard Model” which is, of course, based on the $SU(3)_c \otimes SU(2)_L \otimes U(1)_Y$ symmetry group. It is valid (insofar as it has been tested experimentally) up to energies of several hundred GeV (corresponding to a distance of $\sim 10^{-16}$ cm).

		Charge (e)	Mass(MeV/c^2)	Discovery
Quarks (spin $\frac{1}{2}$)	d	$-\frac{1}{3}$	~ 350	~ 1932
	u	$+\frac{2}{3}$	~ 350	~ 1932
	s	$-\frac{1}{3}$	~ 550	1948-1950
	c	$+\frac{2}{3}$	~ 1800	1974
	b	$-\frac{1}{3}$	~ 4500	1977
	t	$+\frac{2}{3}$	$> 120,000$?
Leptons (spin $\frac{1}{2}$)	e	-1	0.511	~ 1900
	ν_e	0	$< 7.3 \times 10^{-6}$	~ 1957
	μ	-1	105.7	1938-1940
	ν_μ	0	< 0.27	~ 1962
	τ	-1	1784	1975
	ν_τ	0	< 35	1975-1978(?)
Gauge Bosons (spin 1)	gluons	0	0	1970's
	γ	0	0	~ 1905
	W^\pm	± 1	80,220	1983
	Z	0	91,173	1983
Higgs Boson (spin 0)	H^0	0	$> 48,000$?

Table 1.1: “Fundamental” particles of the Minimal Standard Model

Fortunately the Standard Model proved to be more than a sum of its parts. The leptons in the electroweak theory were shown to possess “anomalies” (the triangle anomalies) which threatened renormalizability. These potentially fatal anomalies precisely cancel against anomalies coming from the quarks. In other words, the lepton and quark sectors of the Standard Model cure each others diseases [25] [26]. In the minimal version of the Standard Model there are three families of quarks and leptons (and their antiparticles), twelve gauge

bosons and only one Higgs Boson (see table 1.1). Interestingly, the quark mass eigenstates are not eigenstates of the weak interaction. That is, for purposes of the weak interaction, the quark generations are “skewed”. For all three generations this “skewness” is defined by the Cabibbo-Kobayashi-Maskawa mixing matrix [27]. As can be seen in table 1.1, only two particles are yet to be observed: the top quark and the Higgs boson (special mention should be made for ν_τ which has not been observed experimentally but is supported by considerable indirect evidence). The Standard Model requires as input at least nineteen independent parameters: three coupling parameters ($\alpha, \theta_W, \Lambda_{\text{QCD}}$), two Higgs parameters (M_H, λ), the nine fermion masses (assuming all ν ’s to be massless, the three mixing angles and one phase angle associated with the Cabibbo-Kobayashi-Maskawa mixing matrix, and the QCD θ parameter. These parameters are not explained and thus imply the need for a deeper understanding [28].

1.2 Current State of Particle Physics

Particle physics is an active and continually changing field. Although the Standard Model is a tremendous success, theorists continue trying to extend/supersede it and experimentalists continue pushing its integrity to new limits (looking for any deviations).

1.2.1 Theoretical Activity

The theories of Particle Physics (the Standard Model in particular) continue to advance and evolve. From a phenomenological point of view a tremendous amount of work is being done to compute higher order corrections. Indeed, the search for the top quark is hindered by an incomplete understanding of the cross section for $W + \text{multijets}$. Great strides are being made in understanding how to get meaningful numbers out of QCD as well. The development of “Lattice Gauge Theory” promises the calculation of *all* the consequences of QCD in *both* the high and low energy regimes [29]. Attempts to improve upon the Standard Model are many and fall into several categories. Several approaches attempt to supersede (i.e. Technicolor) or extend (i.e. Higgs multiplets) the Higgs mechanism. One of the more interesting ideas to emerge recently has been the idea that the Higgs may actually consist of a $t\bar{t}$ condensate [30]. A more ambitious approach is that of Supersymmetry which attempts to interrelate bosons and fermions [31]. Perhaps the most radical theory to date is String Theory. This theory (in all its many forms) has at its core the idea that elementary particles are not to be considered as points but as extended objects in many dimensions [32] [33].

1.2.2 Recent Experiments

Theory and experiment must go hand in hand and the experimental achievements over the past 10-15 years have been as significant and dramatic as the theoretical developments. The rising complexity of the modern particle

physics experiments is reflected in the number of scientists on a given experiment and the time necessary to bring an experiment to maturity (~ 10 years for DØ). While a great deal has been accomplished in smaller, fixed target experiments, the thirst for higher and higher center of mass energies has made the collider experiment the most common technique. The collider era began in 1972 with the ISR (proton-proton collider) at CERN and was soon followed by the e^+e^- machines of the mid 1970's: SPEAR and PEP at SLAC, DORIS and PETRA at DESY, and CESR at Cornell. The next generation of e^+e^- colliders appeared in the late 1980's: First SLC at SLAC and TRISTAN at KEK and then LEP at CERN. These colliders have supported many significant experiments culminating in the incredibly precise results from the LEP detectors: OPAL, L3, ALEPH, and DELPHI. The first $p\bar{p}$ collider appeared in the early 1980's with the transformation of the CERN SPS. The two large detectors, UA1 and UA2, discovered the W and Z [15] [16] [17] [18]. The Fermilab Tevatron came online in 1987 and during its first two runs had only one collider detector, CDF. For the 1992-1993 collider run DØ has joined CDF. 1992 has also seen the first ep collider, HERA at DESY, and the detectors (H1 and ZEUS) are already producing physics results.

1.2.3 Future Experiments

With construction times on the order of 10 years, experiments must be carefully planned many years in advance. LEP is being upgraded to a higher center of mass energy (LEPII) and will be online by 1997. A number of

e^+e^- “factories” are under construction (or waiting for funding): DAΦNE at Frascati, TRISTAN-B at KEK, CESR-B at Cornell, PEP-II at SLAC, and τ -CHARM in Spain (unlikely to be funded). The Fermilab main injector is slated for an upgrade and the DØ and CDF detectors are to be upgraded in coordination. CERN is planning to build the LHC (Large Hadron Collider), a pp collider which will have a center of mass energy of 15.4 TeV. In Dallas the US began construction on the SSC (Superconducting SuperCollider), a 40 TeV center of mass pp collider, in the mid 1980’s - with an expected completion in the late 1990’s. Sadly, as of this writing, the project has been terminated.

1.3 The Top Quark

The current published experimental limit on the top quark mass is $M_t > 91 \text{ GeV}/c^2$ from the CDF 1989-1990 collider run [34]. The nonobservation of the top at LEP and SLC (from $Z \rightarrow t\bar{t}$) gives a model independent lower limit of $45.8 \text{ GeV}/c^2$ [35]. Similarly, from measurements of Γ_W by UA2, CDF, and DØ an indirect lower limit of $62 \text{ GeV}/c^2$ at the 95% CL is derived (Lepton-Photon conference, 1993). Unpublished limits from CDF and DØ (see section 6.6.2 for update) are around $120 \text{ GeV}/c^2$ (Tsukuba conference).

At the Tevatron and within the standard model, the dominant production channel for top is $p\bar{p} \rightarrow t\bar{t} + X$. This is achieved both through $q\bar{q} \rightarrow t\bar{t}$ and $gg \rightarrow t\bar{t}$. As can be seen in figure 1.2 [36], at next to leading order (NLO) the $q\bar{q}$ channel is the dominant channel for the top masses currently under investigation. The contributions from the qg and $\bar{q}g$ channels are considered

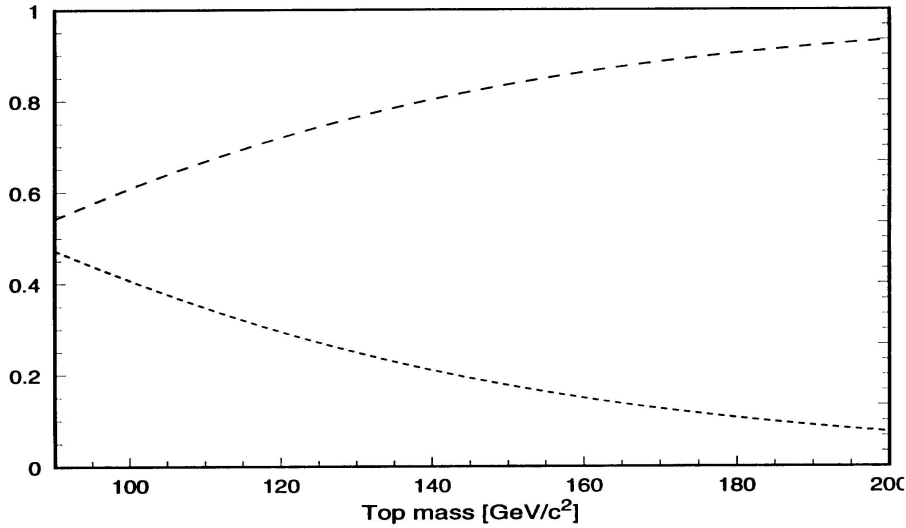


Figure 1.2: Fraction of $q\bar{q}$ (long dashed line) and gg (short dashed line) contribution to $t\bar{t}$ production (NLO) at the Tevatron

to be negligible [37]. The lowest order (order α_s^2) Feynman diagrams for these processes are given in figure 1.3. Similarly, some order α_s^3 and α_s^4 contributions are given in figure 1.4 [38]. The standard predictions for the top quark cross section are based on exact order α_s^2 plus order α_s^3 calculations in perturbative QCD [39] [40]. All such calculations contain a scale factor which estimates the size of the uncalculated order α_s^4 and higher order terms. Typically, this scale factor is determined by varying the renormalization scale (μ) for the α_s^2 plus α_s^3 cross section [41]. Recently, Laenen, Smith, and van Neerven have proposed a technique whereby this scale factor is determined from a resummation of the leading soft gluon corrections in all orders of perturbation theory [42]. All top cross sections used in this thesis are based on these results and a table of values can be found in Appendix A.

As mentioned above, the top and the Higgs are the last two particles of

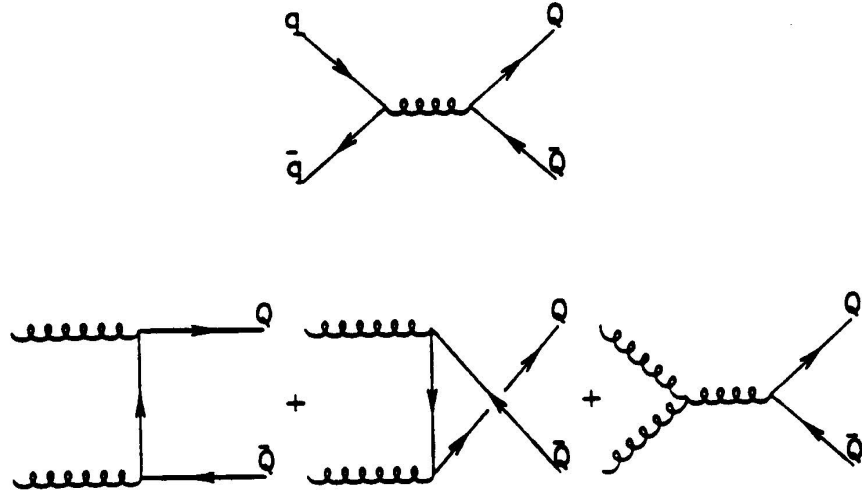


Figure 1.3: Lowest order Feynman diagrams for $t\bar{t}$ production

the Standard Model yet to be detected. The phenomenological features of any (Standard Model or extended model) Higgs sector are intimately tied to the mass of the top [43]. This can be seen in figure 1.5 [44] which shows the dependence of $\sin^2\theta_W$ (at $Q^2 = M_Z$) on the top mass (M_t) for several different values of the Higgs mass (M_H).

All electroweak amplitudes are affected by radiative corrections. Radiative corrections account for the difference between tree level and higher order calculations (loops with virtual fermions). Typically the magnitude of these corrections are defined by the parameter $\Delta\rho$ which is a correction to the parameter ρ which is equal to 1 for tree level diagrams ($\rho \equiv M_W/M_Z \cos\theta_W$). $\Delta\rho$ is usually represented as a power series. Considering just the leading term gives [45][46]

$$\Delta\rho \sim 0.003 \left(\frac{M_t}{100 \text{ GeV}/c^2} \right)^2.$$

Since ρ can be measured to better than one percent the mass of the top will

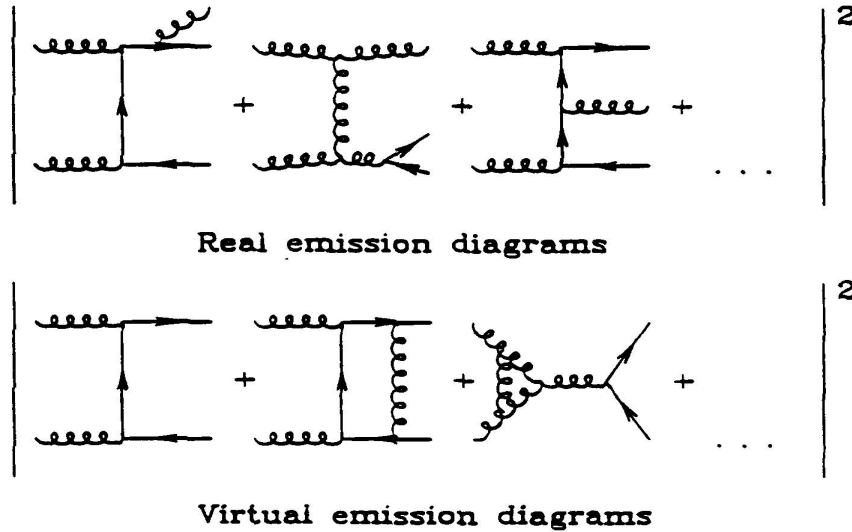


Figure 1.4: Higher order Feynman diagrams for $t\bar{t}$ production

play an increasingly important role as the limit on M_t increases. The above relationship also shows that M_t cannot get too large (due to the definition of ρ).

As pointed out in section 1.1, without the top quark the minimal Standard Model would have anomalies. However, although the top is the simplest way to eliminate these anomalies it may not be the only way. Furthermore, it is not at all clear that these anomalies would be experimentally detectable. So, this argument alone is not sufficiently convincing to justify why there should be a top quark [47]. There are, however, three indirect experimental results which indicate the existence of the top:

1. $B^0 - \bar{B}^0$ mixing : the observed rate of mixing goes as $|V_{td}|^2$ (top is needed in loops). However, other contributions can mimic the

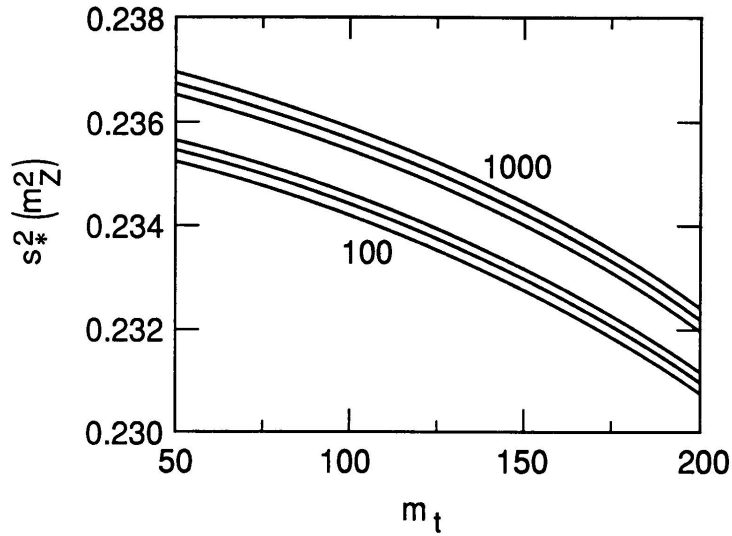


Figure 1.5: Dependence $\sin^2 \theta_W(M_Z^2)$ on M_t and M_H using the known value of M_Z . The two bands show the result of varying M_t , with M_H held fixed at the two values 100 and 1000 GeV/c^2 . The width of each band reflects the 1σ error in M_Z (circa 1989 - $M_Z = 91.150 \pm 0.030 \text{GeV}/c^2$, the current value is $M_Z = 91.173 \pm 0.020 \text{GeV}/c^2$)

top contribution, so this is not unique in general. If the top is very heavy some other states are needed to quantitatively explain $B^o - \bar{B}^o$ mixing [47].

2. Forward-Backward asymmetry in $e^+e^- \rightarrow b\bar{b}$: because of the interference of the γ and Z contributions to $e^+e^- \rightarrow b\bar{b}$ there is a forward-backward asymmetry defined by the quantity $A_{FB} = (N_b^F - N_b^B)/(N_b^F + N_b^B)$ where $N_b^F (N_b^B)$ is the number of b jets produced in the forward (backward) direction [48]. The measurement of this asymmetry provides an indirect measurement of the

weak isospin eigenvalue of the left handed b quark. Correcting for contributions from $B^o - \bar{B}^o$ mixing experiments give a value of $-\frac{1}{2}$ for the weak isospin. Therefore, the b quark must be in a multiplet with one or more other states, one of them having a weak isospin eigenvalue of $+\frac{1}{2}$, which is, by definition, the top quark [47].

3. $\text{BR}(b \rightarrow \ell^+ \ell^-)$: Kane and Peskin have shown [49] that if the b quark is assumed to be an $SU(2)$ singlet, then it will have no charged current interactions and cannot decay via W emission. Since experimentally it is known to decay then it must do so by mixing with the lighter quarks (s and d). This leads to the quantitative prediction $\text{BR}(b \rightarrow \ell^+ \ell^- X) > 0.013$. However, experiments [50] have shown that $\text{BR}(b \rightarrow \ell^+ \ell^- X) < 0.0012$. This establishes that b_L is not an $SU(2)$ singlet and another particle must accompany the b quark.

Because $M_t > M_W + M_b$ and the Cabibbo-Kobayashi-Maskawa element $|V_{tb}|$ is near unity, the dominant decay of the top is the *semiweak* transition $t \rightarrow W^+ + b$ [51]. For the range of top masses currently under study the width is quite large (see table 1.2). For masses in this range the emitted W 's will be predominantly longitudinally polarized, exceeding production of transversely polarized W 's by a factor of $\sim M_t^2/M_W^2$ [51]. A unique consequence of the large $t \rightarrow W^+ + b$ decay rate (and very short lifetime) is that there is not sufficient time for the top quark to form bound state hadrons.

The various analysis channels are determined primarily by how the W 's

M_t (GeV/ c^2)	$\Gamma_{t \rightarrow bW^+}$ (GeV)	τ (10 $^{-25}$ sec)
100	0.093	70.0
150	0.87	7.6
200	2.4	2.7

Table 1.2: Top width and lifetime for $M_t = 100, 150, \& 200$ GeV/ c^2

	($\frac{1}{9}$) $e\nu_e$	($\frac{1}{9}$) $\mu\nu_\mu$	($\frac{1}{9}$) $\tau\nu_\tau$	($\frac{6}{9}$) jets	($u\bar{d}, c\bar{s}$) x 3 colors = 6
($\frac{1}{9}$) $e\nu_e$	$\frac{1}{81}$	$\frac{1}{81}$	$\frac{1}{81}$	$\frac{6}{81}$	
($\frac{1}{9}$) $\mu\nu_\mu$	$\frac{1}{81}$	$\frac{1}{81}$	$\frac{1}{81}$	$\frac{6}{81}$	
($\frac{1}{9}$) $\tau\nu_\tau$	$\frac{1}{81}$	$\frac{1}{81}$	$\frac{1}{81}$	$\frac{6}{81}$	
($\frac{6}{9}$) jets	$\frac{6}{81}$	$\frac{6}{81}$	$\frac{6}{81}$	$\frac{36}{81}$	

Table 1.3: Decay modes of W^+W^-

decay (see table 1.3). Some channels are then further divided on the basis of how the b 's decay (b tagging with soft μ 's or e 's). Practical considerations limit the number of useful channels to five (excluding the additional subdivisions gained from b tagging): $e\mu$, ee , $\mu\mu$, $e +$ jets, and $\mu +$ jets. Just how much of the top cross section “belongs” to each of the decay channels can be seen in figure 1.6. It is clear that most of the cross section is in the more challenging *All Jets* and $\tau+X$ channels. This thesis is concerned with the search for the top in the “ $e\mu$ ” channel (where one W decays to $e\nu$ and the other W decays to $\mu\nu$). The signature is therefore:

- 1 high P_T electron
- 1 high P_T muon

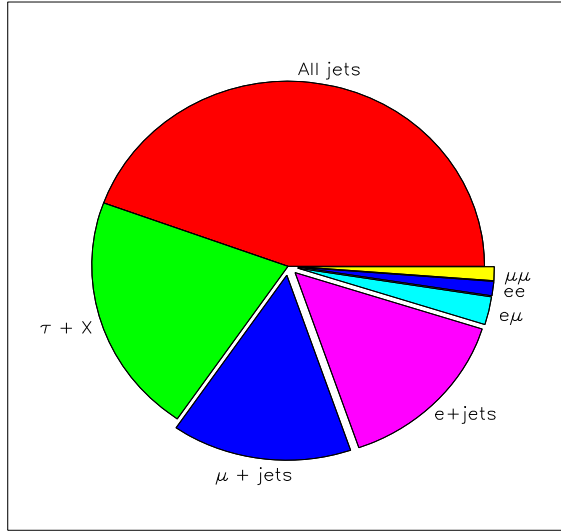


Figure 1.6: Fraction of $t\bar{t}$ cross section into the various decay channels

- Missing E_T (\cancel{E}_T) - from the neutrino's
- 2 jets - from b quark hadronization

As can be seen from table 1.3 the branching ratio for this channel (excluding τ contributions) is $\frac{2}{81}$ (2.47%). The branching ratio for $\tau^- \rightarrow e^- \bar{\nu}_e \nu_\tau, \mu^- \bar{\nu}_\mu \nu_\tau$ is $\sim 17.75\%$ [52]. There are three “ τ contributions” to the $e\mu$ channel: $e\tau[\tau \rightarrow \mu]$ (0.438%), $\mu\tau[\tau \rightarrow e]$ (0.438%), and $\tau\tau[\tau \rightarrow \mu, \tau \rightarrow e]$ (0.078%). This gives an additional 0.95% to the $e\mu$ branching ratio resulting in a total of $2.47\% + 0.95\% = 3.42\%$. Due to possible differences in event characteristics the acceptance for the τ and *standard* channels are considered separately (see section 5.1.5).

Chapter 2

The Tevatron

The Fermilab Tevatron collides protons and antiprotons at a center of mass energy of 1.8 TeV. Until the LHC is built this is the largest center of mass energy available. The Tevatron is among the more recent machines in a long line of accelerators which have contributed tremendously to the development of particle physics [53] [54].

2.1 History

The development of the Tevatron is intimately connected to the evolution of Fermilab and their simultaneous growth can be summarized as a series of milestones:

- December 16, 1966 : AEC chooses Weston Illinois as the site of proposed 200 BeV accelerator
- November 30, 1970 : Linac produces first 200 MeV proton beam [55]

- 1972 - 1982 : Main Ring period - 200 MeV Linac, 8 GeV Booster, and main ring (typically operating at 400 GeV) [56]
- 1976 : Plan to construct Tevatron (then known as the Energy Doubler) and Antiproton Source is proposed by Fermilab Physics Advisory Panel
- 1978 : Bob Wilson resigns as Fermilab Director; Leon Lederman is appointed as the new director one year later
- March 1983 : Last Tevatron Magnet Installed
- June 1983 : Began Tevatron Commissioning
- October 1983 - January 1984 : 400 GeV Fixed Target Physics
- March 1984 - June 1984 : 800 GeV Fixed Target Physics
- July 1984 - November 1984 : Shutdown for CDF overpass construction and Antiproton Source construction
- January 1985 - May 1985 : more 800 GeV Fixed Target Physics
- July 1985 : Antiproton Source Commissioning
- August 1985 - October 1985 : Collider test period
- October 12, 1985 : First Tevatron Collisions seen in the CDF detector
- November 1985 - July 1986 : Shutdown for DØ overpass and DØ Experimental Hall construction
- August 1986 - December 1986 : Accelerator Startup

- June 1988 - May 1989 : Collider run (CDF and DØ tracking ¹)
- July 1989 : Leon Lederman retires as Director and is succeeded by John Peoples
- August 1992 - May 1993 : Run 1A (first run with both CDF and DØ)

2.2 Principles of Operation

The Tevatron is a very complicated device and actually consists of seven separate parts (see figure 2.1): (1) A Cockcroft-Walton accelerator, (2) The Linac, (3) The Booster synchrotron, (4) The Main Ring, (5) The Target Hall, (6) The Antiproton Source, and (7) The Tevatron Ring.

The process begins with a pressurized bottle of hydrogen gas (the original one is still not empty). In the “ion source” electrons are added to the hydrogen atoms thus creating H^- ions. These ions are then released into the Cockcroft-Walton accelerator which produces an static electric field which propels the ions to an energy of 750 keV. The ions are then injected into the 150 meter long Linac. This device induces an oscillating electric field between a series of electrodes thus raising the energy of the ions to 200 MeV. At this stage the H^- ions are sent through a carbon foil which strips off the electrons. The protons are then steered into the Booster synchrotron ring (500 meters in circumference) [57]. A synchrotron is a cyclic machine in which the particles are

¹3 modules of the CDC were installed in the DØ interaction region during the run

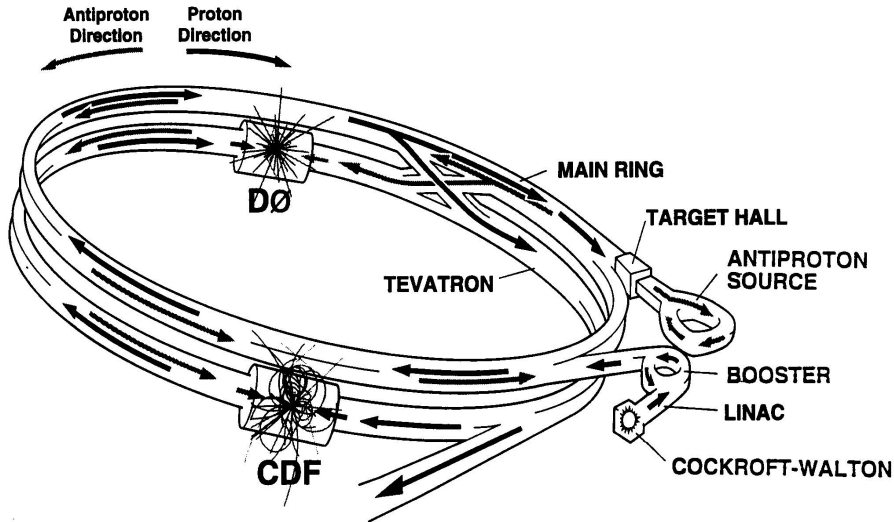


Figure 2.1: The Fermilab Tevatron (collider mode)

confined to a closed orbit by a series of bending magnets. On each pass around the ring the particle's energy is increased by acceleration in a synchronized rf cavity. As the momentum increases, the magnetic field in the bending magnets must be increased if the particles are to remain in the ring (since $p = qB\rho$; where p = particle momenta, q = particle charge, B = magnetic field, and ρ = the radius of curvature) [58]. Thus for a given ring the maximum particle energy is limited by the maximum strength of the magnets and on exiting the booster the protons have an energy of 8 GeV. The protons are then injected into the main ring (a synchrotron consisting of more than 1,000 conventional copper-coiled magnets in a ring of 3.7 miles in circumference). While circulating in the main ring the protons are focused into shorter bunches and raised to an energy of 120 GeV. These bunches are then extracted onto a nickel/copper

target creating about 20 million antiprotons per bunch (for every million protons which strike the target only about 20 antiprotons make it to the next step). The antiprotons of different energies and directions are initially focused using a lithium lens (a cylinder of liquid lithium that transforms a current pulse of 600,000 amperes into a focusing magnetic field) [59] and are injected into the first of two antiproton storage rings.

This first ring is known as the debuncher and uses sophisticated radiofrequency techniques to “squeeze” the incoherent antiproton beam into as compact a phase space as possible. Initially the antiprotons have a large spread in momentum and many are oscillating transverse to the beam direction (not in the ideal orbit). The process whereby the momentum spread and emittance are reduced is known as “cooling”. The debuncher uses two cooling processes. The first, called debunching was invented at Fermilab. As a bunch of antiprotons circulates around the ring complex computer controlled radio frequency techniques act to smooth the antiprotons into a uniform continuous ring (where all the particles have approximately the same momentum). The second process, which reduces the transverse oscillations of the antiprotons, is known as stochastic cooling. Particles whose orbits are not ideal are identified by sensors which send correction signals to kicker electrodes that on the average adjust the path of the wayward particle. When the process is complete the antiprotons are in a single continuous ring at roughly the same momentum and with very little transverse momentum. The above process runs continuously and sends about 20 billion antiprotons into the second antiproton storage ring, the antiproton accumulator (the debuncher and the accumulator are in

the same tunnel which is 520 meters in circumference). Several different systems within the accumulator provide further cooling and increase the density of the antiprotons by a factor of about one million. After four to six hours the population in the accumulator reaches about 200 billion antiprotons which is enough for a “shot” into the main ring.

In the next step the antiprotons are transferred to the main ring, accelerated to 150 GeV and then injected into the Tevatron (travelling in the opposite direction to that of the protons). The Tevatron is in the same tunnel as the main ring but uses much stronger superconducting magnets (operating at a temperature of just 4.7 kelvins they produce a field of ~ 4 Tesla) and can therefore achieve a much higher energy. In the final step the 6 bunches of protons (typically 7×10^{10} protons/bunch) and six bunches of antiprotons (typically 6×10^{10} antiprotons/bunch) are simultaneously raised to full energy (0.9 TeV for run 1A). Once at full energy the beams are squeezed very hard at two beam crossing points BØ (CDF) and DØ. Due to all this manipulation the beams now carry a considerable amount of halo and other debris which must be removed. This is accomplished by a process known as “scraping” whereby metal plates collimate the the beam. This must be performed before the detectors start collecting data. Over time the beams decrease in density due to scattering with residual beam gasses in the vacuum tube and beam beam effects. A typical beam lifetime is approximately 20 hours. During this time the antiproton source runs continuously so that a “stack” of antiprotons is ready when the next shot is needed. Thanks to improvements in several aspects of the accelerator system [60], run 1A saw a record instantaneous lu-

minosity ($7.48 \times 10^{30} \text{ cm}^{-2} \text{ sec}^{-1}$), a record stacking rate ($4.54 \times 10^{10} / \text{hour}$), and a record Integrated Luminosity ($1.48 \text{ pb}^{-1} / \text{week}$). The accelerator is reviewed in “readable” detail in [61].

2.3 Main Injector Upgrade

As noted in section 1.2.3, Fermilab’s future is based on the Main Injector which is being constructed tangent to the Tevatron in a separate tunnel on the southwest corner of the Fermilab site. This ring is approximately half the size of the main ring but will have much greater performance [62] [63]. This will allow luminosities in excess of $5 \times 10^{31} \text{ cm}^{-2} \text{ sec}^{-1}$ and permit the simultaneous operation of fixed target and colliding beam modes. The physics issues which would be made available for study with this device include state of the art CP violation studies, rare kaon decays, searches for transmutation between neutrino generations, and detailed studies of quark properties [64]. This project passed its most significant milestone to date on September 22, 1992 when the DOE (Department of Energy) authorized funding for detailed design and preliminary civil construction. Earth moving began on the Main Injector project soon after on July 24, 1992 [64].

Chapter 3

The D \emptyset Detector

D \emptyset is a multipurpose detector currently in operation at the Fermilab Tevatron. It is a second generation detector (UA1, UA2, and CDF are first generation detectors) which was designed with an emphasis on good electron and muon identification, superior electromagnetic and hadronic energy resolution, and full 4π coverage. In the tradition of UA2, D \emptyset does not have a central magnetic field.

The detector is made up of three primary systems: (1) an inner tracking system which is surrounded by (2) an electromagnetic and hadronic calorimeter which is in turn surrounded by (3) an iron toroid and multilayer muon tracking system (see figure 3.1).

3.1 History

As with the Tevatron, the history of D \emptyset can be summarized as a series of milestones:

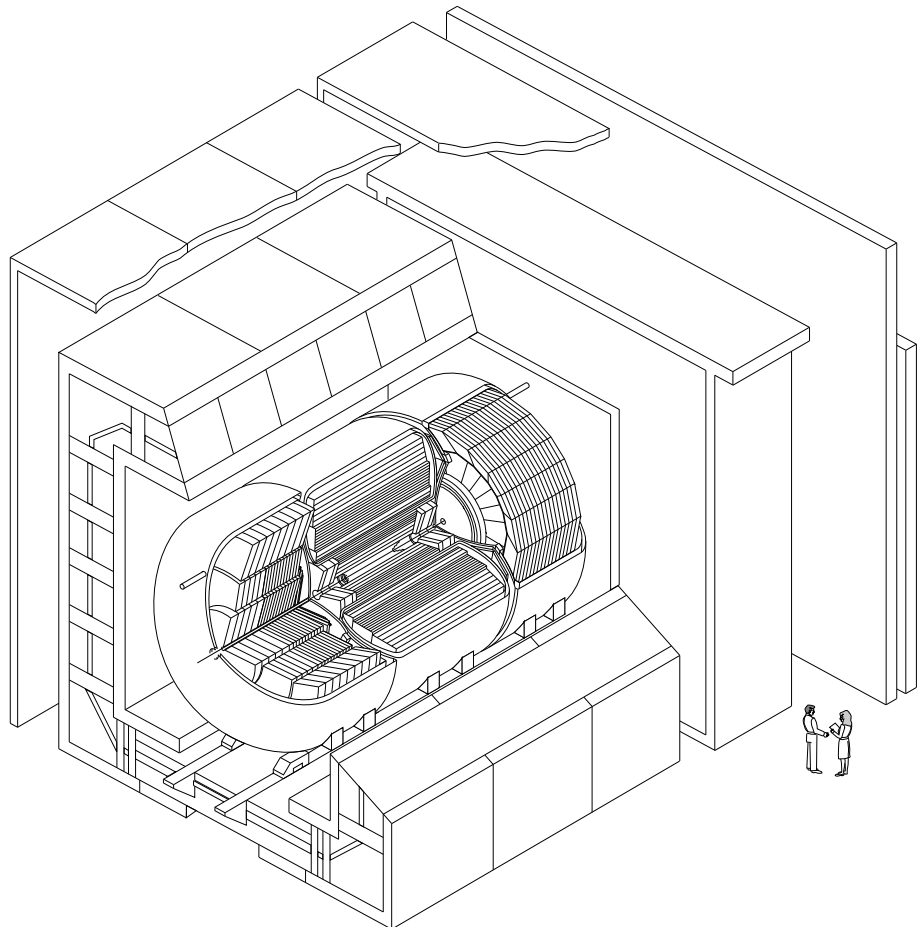


Figure 3.1: The DØ detector

- June 1983 - The PAC turns down several experiments (P714 (aka LAPDØG), P728, P724, P726, ...) with the charge to build a more comprehensive “DØ” detector; these separate groups are thus merged into a single group and Paul Grannis is appointed spokesman and Mike Marx deputy spokesman
- November 1983 - full DØ proposal presented to PAC

- 1983 - 1984 : Initial design period
- November 1984 - First full DOE review
- 1985 : First funding
- 1985 - 1992 : detailed design, construction, and testing
- February - May, 1991 : Cosmic ray commissioning run
- February 14, 1992 : DØ is rolled into the collision hall
- May 12, 1992 : First collisions recorded at DØ
- May 12 - July 20, 1992 : Commissioning run
- July 21 - August 20, 1992 : Tevatron shutdown
- August 21, 1992 - May 31, 1993 : Run 1A, DØ records 15 pb^{-1} on tape

3.2 Physics Studied at DØ

With an emphasis on precision measurements of leptons, photons, and jets, DØ is designed principally to study high P_t physics. The topics to be attacked during DØ's early running are many [65] [66]: the search for the top quark, primarily in the leptonic and semileptonic decay modes; precision mass (and width) studies in the electroweak sector with the stress on a precise determination of the W/Z mass ratio; measurements of the $WW\gamma$ coupling; searches for non-standard top and Higgs particles with W width studies; high P_t QCD physics, in particular direct photon and vector boson plus multijet

studies; b quark studies, particularly in the relatively unexplored forward region (a difficult job); and the combination of good lepton identification and missing E_t determination will be used to raise the search limit for the gluino's expected in the minimal supersymmetric models now popular as candidates for grand unification theories.

3.3 Design Principles of Detectors at Colliding Beams

There are many factors which must be balanced when designing a Colliding Beam detector. Physics objectives must be weighed against practical and monetary limitations. The Physics which is to be emphasized determines the ideal detector. Then compromises and tradeoffs are studied in order to determine the optimal design given the technological and financial limitations. The basic design of all multipurpose collider detectors is based on the signatures of the physics to be studied. An idealized detector is shown in figure 3.2 [67]. Each of these signatures will be discussed in detail with the description of the individual components of the D \emptyset detector (see sections 3.4 to 3.6).

It is clear that detectors of this type are incredibly sophisticated since they are required to simultaneously detect all the different types of particles with very high efficiency and over the full 4π solid angle [67]. It is not uncommon for such a detector to cost 100 million dollars and absorb several thousand man years of labor (from engineers, physicists, technicians, and graduate students).

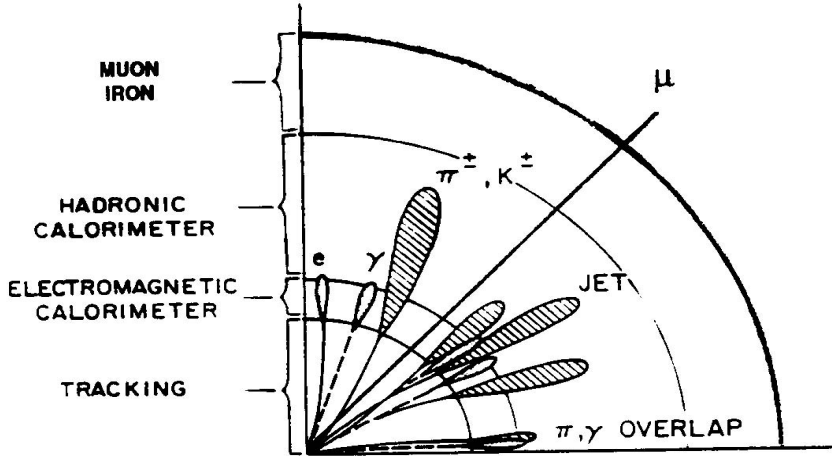


Figure 3.2: A Conceptual Detector

3.4 Tracking

In order to identify electrons and muons it is necessary to reconstruct the path of the particle. Furthermore, track information (dE/dx , track multiplicity) is often used as a confirmation of what is seen in the calorimeter. Additionally, tracking information is essential for the identification of secondary vertices or the identification of τ leptons, where the only signature depends on the number and orientation of charged tracks [68].

There are several types of tracking detectors currently in use: wire chambers, proportional drift tubes, drift chambers, time projection chambers, and silicon detectors.

The DØ tracking detector consists of four subdetectors, three drift chambers (VTX, CDC, FDC) and the TRD (see figure 3.3). The Vertex chamber (VTX) consists of three layers, the innermost of which lies just outside the

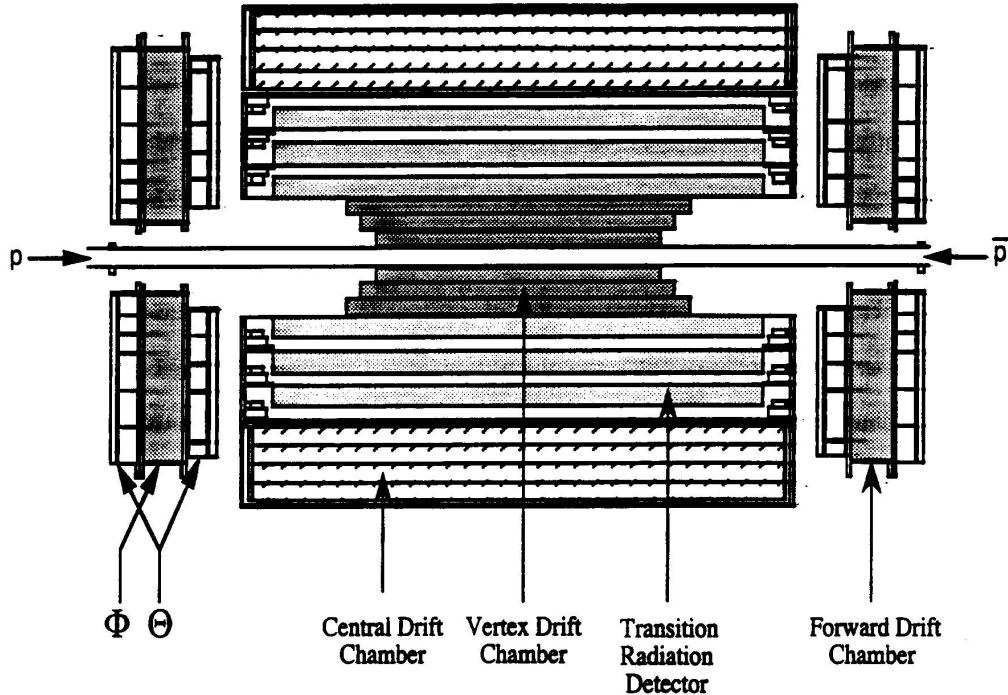


Figure 3.3: DØ Tracking Chambers

beryllium beam pipe. The Transition Radiation Detector (TRD) lies just outside the Vertex chamber and consists of three concentric layers of polypropylene foils followed by radial drift x-ray detectors. Outside the TRD is the Central Drift Chamber (CDC) which consists of four layers of axial wire chambers. Located at the ends of the VTX-TRD-CDC are the two FDC chambers. Each of these consists of two types of chambers, Φ and Θ . The Φ chambers have radial wires and measure the azimuthal angle (ϕ) of a track. The Θ chambers have wires aligned perpendicular both to the beam and to the Φ chamber wires (see figure 3.8).

The design choices for these detectors are based on the fact that DØ

does not have a central magnetic field. In this case the main focus is on good spatial resolution of individual particles, high efficiency, good two-track resolving power, and good dE/dx measurements so as to distinguish between electrons and closely spaced conversion pairs [69]. All the tracking detectors are constrained by the Collider bunch time spacing of $3.5\ \mu\text{s}$. This time allows for relatively long drift cells. Good two track resolving power is obtained by the use of a Flash Analog to Digital Conversion (FADC) system for signal digitization in which the charge is sampled at $\sim 10\ \text{ns}$ intervals (see section 3.4.6). With drift speeds of $10\text{-}35\ \mu\text{m/ns}$ this corresponds to an effective detector granularity of $100\text{-}350\ \mu\text{m}$ [69].

3.4.1 Principles of operation of wire (drift) chambers

A charged particle can interact in several different ways with a medium through which it is passing. At present, tracking detectors only utilize the Coulomb interaction with atoms and nuclei in a medium. Coulomb interactions can be further subdivided into three principal classes: (1) interactions with electrons in individual atoms (ionization), (2) interactions with the nucleus, and (3) collective effects such as Čerenkov radiation and transition radiation (see section 3.4.5). All wire chambers rely on interaction (1), where ionization electrons and ions are created by the passage of a charged particle through a gas. In the presence of an electric field the electrons and ions drift apart. Near the positive electrode wire the electrons can acquire enough energy to create new ion pairs and an avalanche will develop. The separa-

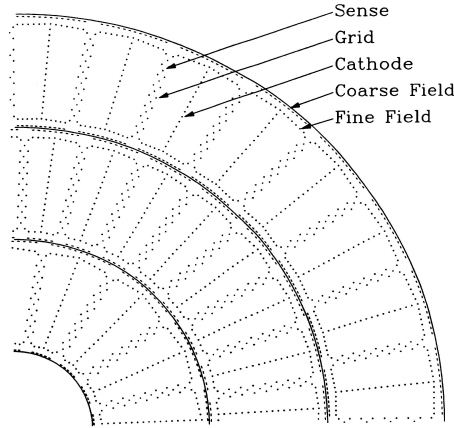


Figure 3.4: End view of one quadrant of the vertex chamber

tion of the ions liberated in this avalanche will then induce a signal on the wire. By measuring the time from some reference to the time the electron pulse is induced on the anode wires (the electron drift time), the track of a charged particle can be reconstructed. The details of drift chamber operation are discussed more fully in [70] [71] and [72].

3.4.2 Vertex chamber

In order to identify secondary vertices from c and b quark decays it is necessary to have a high precision ($5\text{-}50\ \mu\text{m}$) vertex detector. An additional design goal of a vertex chamber is to complement (in track reconstruction, dE/dx , and vertex finding) the other tracking detectors. Experience has shown that it is often necessary to have a considerable degree of redundancy built into any detector.

The basic operation of the vertex chamber is essentially no different than

that of any other wire chamber (see section 3.3). However, to achieve such precision in a high luminosity environment, it is necessary that wire placement accuracy be $< 25 \mu\text{m}$ and that the electronics (see section 3.4.6) be capable of measuring drift times with an accuracy on the order of a few nanoseconds [73].

The DØ vertex chamber has been optimized for good spatial resolution, good track pair resolving power, and large η coverage [74]. The chamber consists of three concentric layers built between four carbon fiber cylinders (see figure 3.4). Not evident in figure 3.4 is the fact that adjacent sense wires are staggered by $\pm 100 \mu\text{m}$ in ϕ to resolve left right ambiguities (see section 3.3). To further aid pattern recognition, the cells of the three layers are offset in ϕ . Note also that the inner layer has 16 cells while the outer two layers each have 32 cells. Coarse field shaping comes from aluminum traces on the carbon fiber cylinders. Finer field shaping comes from the fine field, grid, cathode, and sense wires (see figure 3.4). Wire sizes, composition, and other vital statistics may be found in table 3.1 [75]. The end support is provided by thin G-10 bulkheads attached to the carbon fiber cylinders [76]. Titanium tie rods then connect each bulkhead to the next inner cylinder in order to support the wire tensions (see figure 3.5).

The z coordinate is determined by a method known as charge division. Since the sense wires are resistive, the charge signals from both ends can be used to determine the location of a hit. This method requires that the pulses be fairly well separated and that the cell occupancy not exceed several particles - a situation which is rare in a high multiplicity environment. As an additional

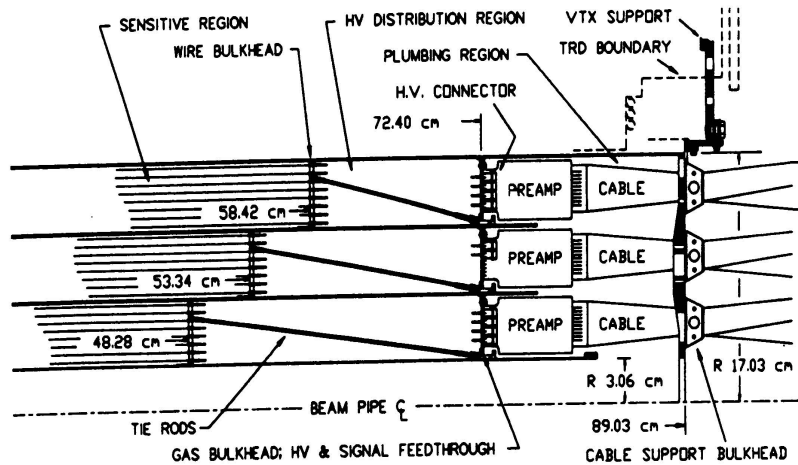


Figure 3.5: Plan view of the ends of the vertex chamber showing the active chamber region, the support structure, and the electronics feedthrough bulkhead

measurement the DØ vertex chamber included in its design rectangular pads that “see” an induced signal from a small portion of several sense wires. The pads are connected together in a helical pattern on the active region side of all the carbon fiber cylinders except for the innermost (due to lack of space) [77]. Due to problems with induced electronic noise it was not possible to make these pads functional and the cables and associated electronics were removed prior to the start of the run to minimize the number of radiation lengths. Overall, the vertex chamber has a resolution in $r\phi$ (plane perpendicular to the beam axis) of $60 \mu\text{m}$ and in z (for isolated tracks) of 1.5 cm [78].

3.4.3 CDC

The Central Drift Chamber provides trajectory information on isolated

Length of active volume: Layer 1	96.6 cm
Layer 2	106.6 cm
Layer 3	116.8 cm
Radial Interval (active)	3.7 - 16.2 cm
Number of layers	3
Radial wire interval	4.57 mm
Number of sense wires/cell	8
Number of sense wires	640
Type of Gas	CO ₂ (95%)-ethane(5%)-H ₂ O(0.5%)
Pressure of Gas	1 atm
Drift Field	1.0-1.6 kV/cm
Average Drift Velocity	7.6-12.8 μ m/ns
Gas Gain at Sense Wires	4x10 ⁴
Sense Wire Potential	+2.5 kV
Diameter of Sense wire	25 μ m NiCoTin
Diameter of Guard wire	152 μ m Au-plated Al

Table 3.1: Vertex Chamber Parameters

charged particles and additional track information (dE/dx , track multiplicity) for the region $|\eta| < 1$. As with the Vertex chamber, for $r\phi$ measurements the CDC relies on information from anode wires which run parallel to the beam direction. As is typical for a drift chamber, a cell is arranged with the anode wires in the center, surrounded by a cathode (see figure 3.6). Since only timing information is obtained, there is no way to distinguish between right and left (i.e. to determine on which side of the wire plane the particle passed). In order to remedy this at the cell level the sense wires are staggered by 0.2 mm. This staggering breaks the symmetry and allows a determination of the correct side. As can be seen in figure 3.6, the cell layers themselves are staggered by one half

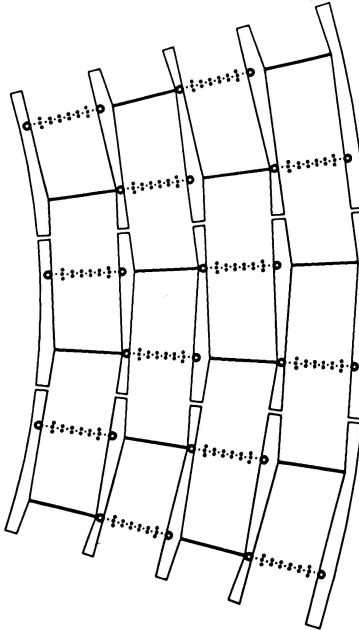


Figure 3.6: End view of one “3/32”nd of the CDC

cell to further aid track reconstruction and minimize dead regions. The CDC is somewhat unique among hadron collider drift chambers in several respects. First, it is constructed of 32 identical modules so that, in principle, problems can be corrected by replacing a single module. Each module (see figure 3.7) is constructed of a set of shelves connected at the ends with plates of G10. The shelves are made from a styrofoam-like material called Rohacell which is covered with an epoxy coated cloth and then wrapped in several layers of 50 μm Kapton. The field shaping is accomplished through a series of voltage dividers connected to resistive epoxy strips which are “silk-screened” onto the shelves. As noted in section 3.4, the entire D \emptyset tracking system is contained within the CDC can. The wire plugs on the ends of the modules fit into holes in the Aluminum CDC endplate and after assembly it supports all of the CDC

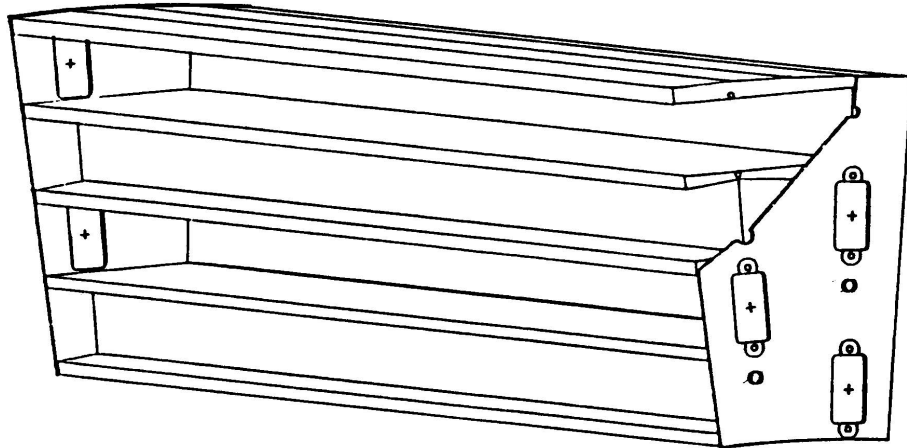


Figure 3.7: CDC module

wire tension. The CDC is also unusual in its use of delaylines for measuring the z position. The delaylines are imbedded in teflon tubes built into the shelves and lie just next to and parallel to the outer sensewires in each cell (see figure 3.6). When an avalanche occurs on an outer sensewire pulses are induced on the delayline and the difference in arrival times at the two ends allows for a determination of the z coordinate. The CDC has a resolution in x, y of 180 μm and in z of 3.5 mm [78] [79]. Wire sizes, composition, and other vital statistics may be found in table 3.2 [75]. Details of the design, construction, and testing of the CDC may be found in [80] and [81].

The precision with which a multiwire chamber can reconstruct tracks depends crucially on an accurate knowledge of the wire locations. A wire with a tension that is too low will mismeasure tracks if that wire is a sense wire and will distort the field if that wire is a potential wire. Additionally wires with

Length of active volume:	179.4 cm
Radial Interval (active)	51.8 - 71.9 cm
Number of layers	4
Radial wire interval	6.0 mm
Number of sense wires/cell	7
Number of sense wires	896
Number of delay lines	256
Type of Gas	Ar(93%)-CH ₄ (4%)-CO ₂ (3%)-H ₂ O
Pressure of Gas	1 atm
Drift Field	620 V/cm
Average Drift Velocity	34 μ m/ns
Gas Gain at Sense Wires	2, 6 \times 10 ⁴
Sense Wire Potential	+1.5 kV
Diameter of Sense wire	30 μ m Au-plated W
Diameter of Guard wire	125 μ m Au-plated CuBe

Table 3.2: Central Drift Chamber Parameters

too low a tension may create instabilities and induce sparking. The wires are usually installed at tensions close to the elastic limit, so, a wire tension which is too large could lead to broken or deformed wires. Therefore, a system was designed and constructed to measure the wire tensions in the CDC. Since the tension of a wire is related to its resonant frequency (first harmonic) by

$$\nu = \frac{1}{2\ell} \sqrt{\frac{T}{\mu}}$$

where ν \equiv resonant frequency, ℓ \equiv length, T \equiv tension, and μ \equiv mass per unit length of the wire, a measurement of the resonant frequency provides an indirect measurement of the wire tension. The actual measurement is made as follows: The wire to be measured is placed in a magnetic field and given a short

current pulse. Due to the Lorentz force law, this effectively gives the wire a “kick” and, like a guitar string, it will then vibrate at its resonant frequency. For a closed loop, Faraday’s law states that

$$E_{\text{emf}} = -\frac{d\Phi}{dt}$$

where E_{emf} is the induced voltage on the loop and Φ is the magnetic flux through the loop. Since the wire is vibrating Φ will oscillate at the resonant frequency. Therefore, the resonating wire will have a voltage induced across it which is oscillating at the resonant frequency. After the wire has been pulsed the resulting (damped harmonic) waveform is amplified and digitized with a CAMAC ADC (analog to digital converter). The digital output of the ADC is read into a PC where it is stored. A PC program then performs a Fast Fourier Transform (FFT) on the voltage waveform to determine the resonant frequency from which it computes the tension. If the value is acceptable the system automatically switches on to the next wire.

The delay lines rely on an induced pulse generated by an avalanche on the neighboring sense wire. The pulse is induced at some position Z (as measured from the center of the delay line) on the delay line and travels towards both ends of the line where it is amplified and shaped and then digitized by the FADCs. Typical signal speeds are ~ 2.4 mm/ns. Taking the sense wire signal arrival time as the time origin, the delay line pulse left and right side arrival times are

$$T_L = (L/2 + Z)/V$$

$$T_R = (L/2 - Z)/V$$

where L is the active length of the delay line and V is the signal propagation speed along the delay line [81]. These equations can be solved to determine Z_L and Z_R , the Z coordinates as measured from the right and left sides of the delay line. However, the V must be obtained by calibration as follows: Each delayline was calibrated before insertion into the modules by inducing a pulse at 16 fixed positions along Z and measuring the arrival times at both ends. A linear fit of the Z position versus time then provides the mean propagation velocity V along the line. Additionally a time offset was computed separately for each side of the delay line to account for the difference between the physical center of the line and the geometric center at $Z = 0$ after installation into the module.

3.4.4 FDC

The FDC chambers perform the same function as the CDC but for $|\eta| > 1$ and down to $\theta \sim 5^\circ$. The location and orientation of the six FDC chambers are described in the introduction to section 3.4 (see figure 3.8). The FDC chambers are constructed with the same materials and in a similar fashion to the CDC. However, in place of the epoxy strips used in the CDC for field shaping the FDC's use 25 μm aluminum etching. As noted in section 3.4, each FDC package is made up of three chambers, two Θ and one Φ . Each Θ module consists of four mechanically separate quadrants, each containing six rectangular cells at increasing radii. All the cells have eight anode wires (wireplane in ϕz) and have one delay line (identical in construction to the

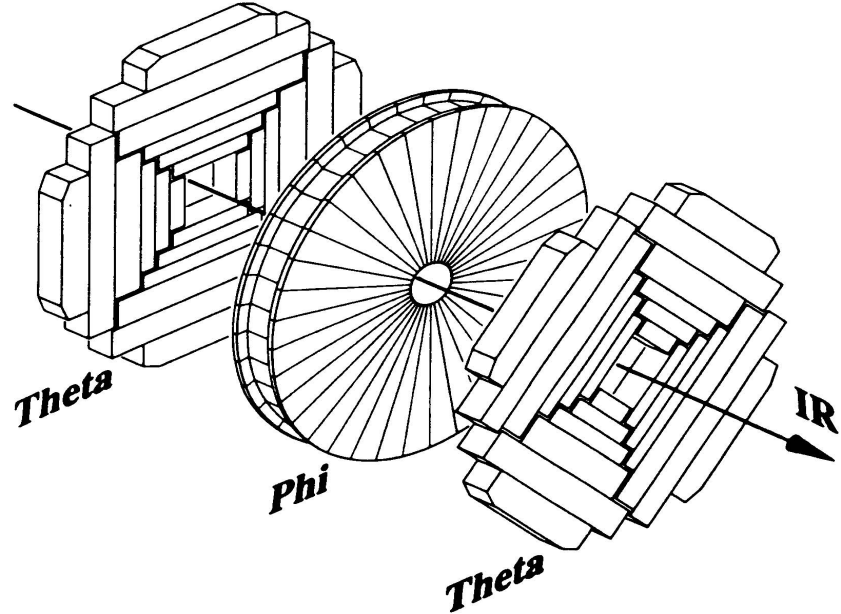


Figure 3.8: FDC chambers (one side)

CDC delaylines) to give a ϕ measurement [82]. Each Φ module is a single chamber containing 36 sectors over the full ϕ range. Each Φ sector consists of 16 anode wires (forming a plane in rz), but there are no delaylines. Wire sizes, composition, and other vital statistics may be found in table 3.3 [75]. Overall, the FDC has a drift resolution in $r\phi$ of $180 \mu\text{m}$ and resolution along the delay lines of 2 mm [78]. Details of the design, construction, and testing of the FDC may be found in [83] and [84].

3.4.5 TRD

When a charged particle passes through an interface between two types of material with different dielectric constants, the requirement that the field

	Θ modules	Φ modules
z interval	104.8-111.2 cm 128.8-135.2 cm	113.0-127.0
Radial Interval	11-62 cm	11-61.3 cm
Number of cells in radius	6	
Maximum Drift Distance	5.3 cm	5.3 cm
Sense Wire staggering	0.2 mm	0.2 mm
Sense Wire separation	8 mm	8 mm
Angular Interval/cell		10°
Number of Sense wires per cell	8	16
Number of Delaylines per cell	1	0
Number of Sense Wires per end	384	576
Number of Delaylines readout/end	96	
Type of Gas	Ar(93%)-CH ₄ (4%)-CO ₂ (3%)	-H ₂ O
Pressure of Gas	1 atm	1 atm
Drift Field	1.0 kV/cm	1.0 kV/cm
Average Drift Velocity	37 μ m/ns	40 μ m/ns
Gas Gain at Sense Wire	$2.3, 5.3 \times 10^4$	3.6×10^4
Sense Wire Potential	+1.5 kV	+1.5 kV
Sense Wire Diameter	30 μ m Au-plated W	
Guard Wire Diameter	163 μ m Au-plated Al(5056)	

Table 3.3: Forward Drift Chamber Parameters

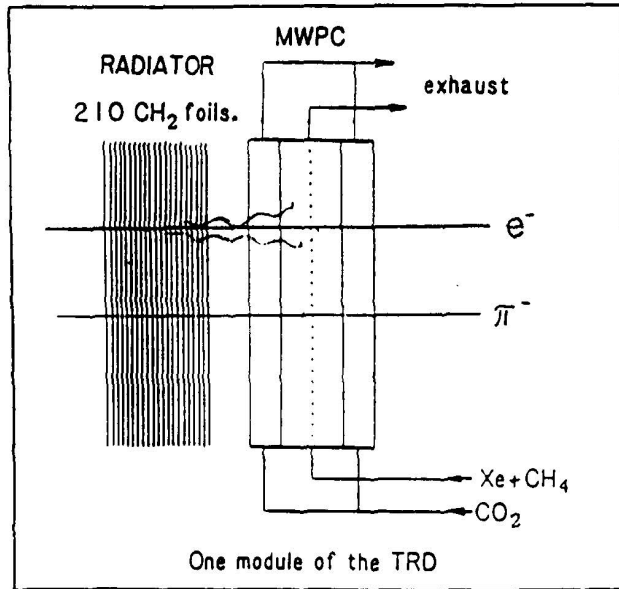


Figure 3.9: Schematic view of a TRD

of the particle satisfy the boundary conditions at the transition point requires a radiative component of the field. Although the effect is weak, if a large number of interfaces are put together in a short distance, sufficient radiation (in the form x-rays) will be produced to be observed [85]. For the DØ TRD the radiators consist of many sheets of 18 μm polypropylene, a material which is low in Z so that the radiated photons are not absorbed by the radiator before reaching the detector. The amount of radiation depends logarithmically on the value of E/m_0c^2 for the particle so that the device primarily separates those particles lighter than a certain mass from those that are heavier [85]. For nonmagnetic detectors such as DØ the TRD is viewed as particularly important for aiding electron identification since the inability to measure the particle momentum results in a significantly larger background from π 's and

π/γ overlaps. A schematic is shown in figure 3.9. For the DØ TRD the x-rays have an energy distribution which peaks at 8 keV. The x-rays convert in the first part of the Xenon filled radial drift chamber and the liberated charge then drifts toward the anode where the avalanche occurs. The location and orientation of the TRD is described in section 3.4. The TRD is discussed in more detail in [76] and [86].

3.4.6 Electronics

The electronics and associated readout for all the tracking chambers is similar. The preamplifiers which are based on the Fujitsu MB43458 [87] quad common base amplifier in a surface mount package, are mounted in groups of eight channels on a hybrid together with input protection circuitry that fits a regular 28-pin DIP socket [77]. All the tracking chambers (VTX,TRD,CDC, and FDC) together have more than eight thousand channels which must be processed in parallel. The signal processing occurs in three stages: the preamplifiers (located on the chambers), the shapers (located in the platform under the DØ detector), and the flash ADC's located in the Movable counting house [88]. An overview of this system is shown in figure 3.10 [89]. The tracking electronics is discussed in great detail in [90] and [88].

3.5 Calorimeter

The calorimeter is, in more ways than one, the centerpiece of DØ. In the absence of a central magnetic field the calorimeter is the only source of precise

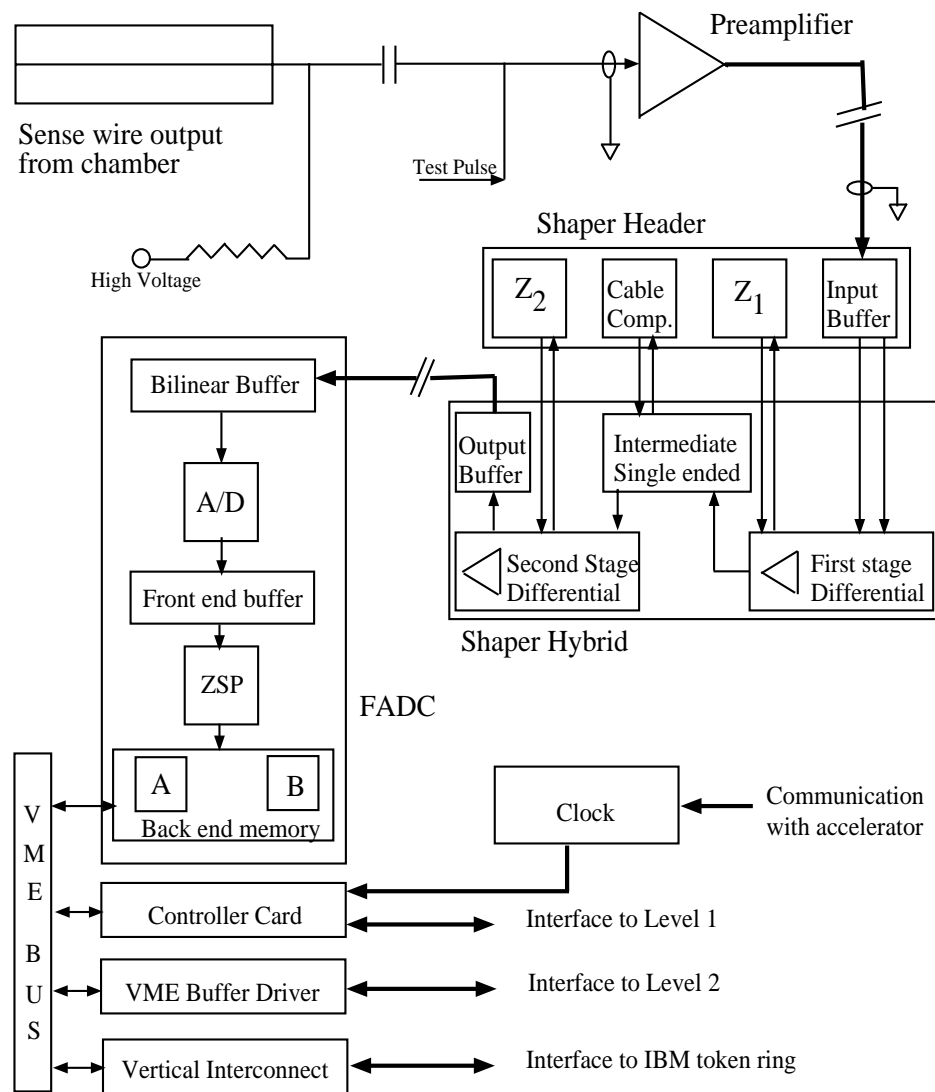


Figure 3.10: Tracking Electronics readout path and controls

energy measurements. Furthermore, it provides much of the information necessary for the identification of electrons, photons, jets, and muons and plays an essential role in the determination of the missing E_T (\cancel{E}_T).

Analogous to the well known laboratory device for measuring heat, a calorimeter is a device that measures the total energy deposited by a particle or cluster of particles. At present this is the best way to detect neutral particles. Within High Energy Physics the primary type of calorimeter is one which samples the development of a shower initiated by an incident particle. There are two types of “sampling” calorimeters, depending on whether the incident particle initiates an electromagnetic or hadronic shower. Each of these types is optimized to maximize the rejection of the other type of shower [91]. Typically sampling calorimeters have a sandwich structure of absorber (i.e. lead, steel, etc.) interlaced with some type of detector (i.e. scintillator/ionization - NaI, BGO, lead glass, liquid argon, etc.) medium. A shower developing in a sampling calorimeter will liberate photons and charged particles which will be detected in the scintillator/ionization medium. As discussed in [91], the total charged track length is proportional to the number of secondaries which is in turn proportional to the incident energy. Thus, a sampling calorimeter converts incident particle energy into scintillator light or collected charge (by some appropriate conversion factor). A full discussion of the use of calorimetry in High Energy Physics is given in [92] and [93].

The desire to construct a calorimeter with good radiation hardness, unit gain, and a straightforward method of calibration led the DØ collaboration to choose liquid argon as the ionization medium. However, the use of liquid

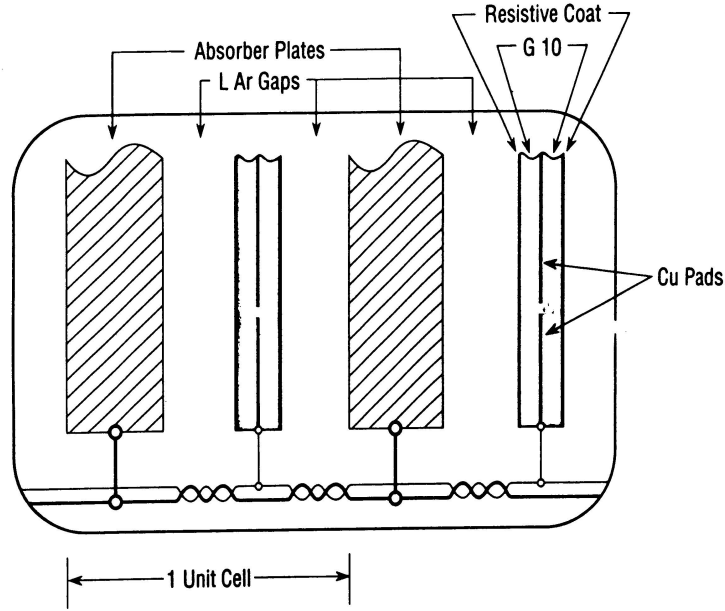


Figure 3.11: Schematic of DØ Calorimeter cell

argon does have a major complication, namely it must be operated cold (86K) and therefore requires a cryostat. Uranium was chosen as the absorber for the sensitive electromagnetic (EM) and fine hadronic (FH) layers. In addition to nearly equalizing electromagnetic and hadronic response, uranium, being very dense, allows the calorimeter, and therefore the complete detector, to be made quite compact (substantially reducing the cost). As can be seen in figure 3.11, a generic calorimeter unit cell consists of alternating layers of absorber and readout boards immersed in liquid argon. The readout board is a copper plate sandwiched between two pieces of G10 (1.3 mm each) which are covered with a resistive epoxy coating [94]. The absorbers are kept at ground and the readout boards are at +2.0 to +2.5 kV. The distance between absorber and readout pad is 2.3 mm. As a shower develops charged particles cross the liquid

argon gaps causing ionization in the liquid argon. The liberated electrons drift toward the resistive anode (typical drifttime of ≈ 450 ns) and induce a pulse on the copper readout pad. The D \emptyset Calorimeter is discussed in considerable detail in [95].

As mentioned above, the final signal is the number of electrons which are registered in the readout pads. The resolution of the calorimeter for measuring the energy of an incident particle is determined by fluctuations in the number of these electrons. These fluctuations have several sources [96]:

- Sampling Fluctuations - fluctuations in the actual energy deposited in the active layers
- leakage of energy out of the calorimeter
- noise in the active layers (e.g. due to natural radioactivity of the depleted uranium plates)
- gain (HV, spacing, electronics, Argon temperature, O_2 contamination) variations
- electronic noise

For D \emptyset the resolution is parameterized as

$$\left(\frac{\sigma}{E}\right)^2 = C^2 + \frac{S^2}{E} + \frac{N^2}{E^2},$$

where C is the “constant” term which represents the calibration (gain) errors, S is the sampling fluctuations term, decreasing with the number of collected charges and thus with E , and N is the noise term (includes electronic and

uranium noise) giving a constant variance. From test beam it is found that [95] [97]

For Electrons:

$$C = 0.003 \pm 0.002, S = 0.157 \pm 0.005(GeV)^{\frac{1}{2}}, N \approx 0.140 \text{ GeV}$$

For Pions:

$$C = 0.032 \pm 0.004, S = 0.41 \pm 0.04(GeV)^{\frac{1}{2}}, N \approx 1.28 \text{ GeV}.$$

The calorimeter has a position resolution of $0.8 - 1.2$ mm for isolated high energy electrons in the central region. This resolution has a energy dependence which varies approximately as $1/\sqrt{E}$. The position resolution (in conjunction with the tracking) is very important to distinguish electrons from π^\pm/π^0 overlaps.

The transverse sizes of the cells were chosen to be comparable with the transverse sizes of showers: $\sim 1\text{-}2$ cm for EM showers and ~ 10 cm for hadronic showers (corresponding to $\Delta R = \sqrt{\Delta\eta^2 + \Delta\phi^2} \sim 0.5$). Longitudinal segmentation within the EM, fine hadronic, and coarse hadronic sections is essential since the longitudinal shower profile helps to distinguish between electrons and hadrons. There are four separate depth layers for the EM modules (CC and EC). The first two layers are typically 2 radiation lengths thick (at 90° incidence) and are included to help measure the longitudinal shower development near the beginning of showers where photons and π^0 's differ statistically. The third layer spans the region of maximum EM shower energy deposition and the fourth completes the EM coverage of approximately 20 radiation lengths. In

addition to the radial variation (see above and tables 3.4 and 3.5) of calorimeter type, the calorimeter is also segmented in η and ϕ . Typically the segmentation is $\Delta\eta \times \Delta\phi = 0.1 \times 0.1$ (see sections 3.5.1 and 3.5.2 for details). However, to achieve a better measurement for EM showers, the EM calorimeters have $\Delta\eta \times \Delta\phi = 0.05 \times 0.05$ for the third layer (typical location of shower maximum). The readout boards are ganged together in a “pseudo”-projective geometry. The geometry is “pseudo”-projective because the centers of the cells at increasing shower depth do indeed lie on rays which project from the interaction point, but the cell boundaries are perpendicular to the absorber plane [95]. For ease of construction and to provide access to the central detectors, the DØ Calorimeter is constructed in three separate parts, each in its own cryostat (see figure 3.12).

3.5.1 Central Calorimeter

The Central Calorimeter covers the region $|\eta| < 1.2$. Much like the CDC the Central Calorimeter is based on a modular construction. Whereas the CDC has just one layer (consisting of four sub-layers) of 32 modules , the Central Calorimeter (CC) has three “concentric” layers of modules: the inner electromagnetic (EM) layer with 32 modules, the middle fine hadronic (FH) layer with 16 modules, and the outer course hadronic (CH) layer with 16 modules. The EM layer measures the energy (and position) of electrons and photons wheres the FH layer measures the energy of more penetrating particles such as pions. To contain the large fluctuations in longitudinal shower

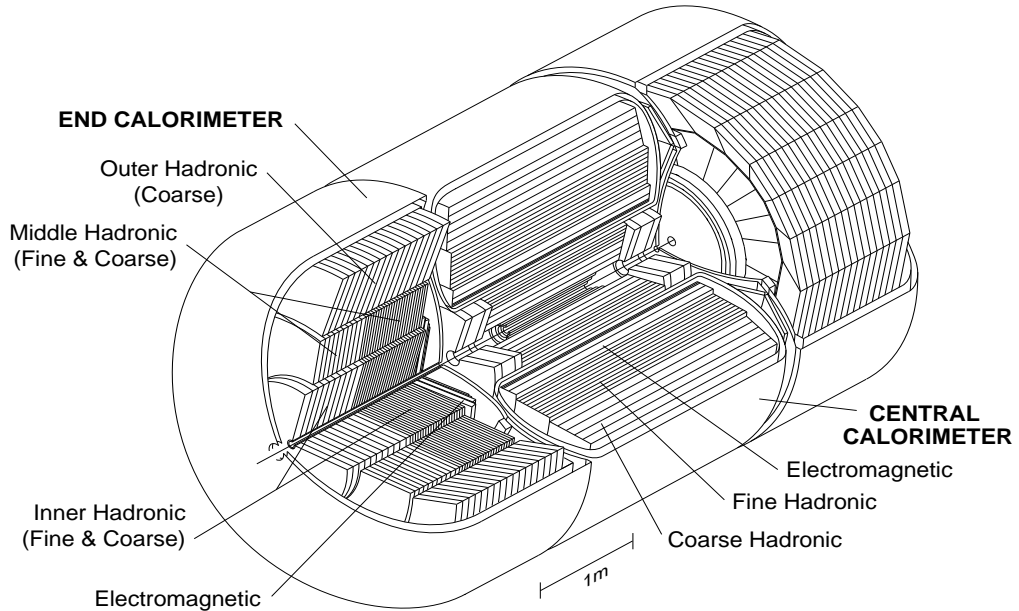


Figure 3.12: DØ Calorimeter

depth of hadrons, DØ has an additional layer, the CH, which protects against punchthrough and leakage. Many vital statistics of the CC are given in table 3.4 [98] [99].

3.5.2 End Calorimeter

The End Calorimeter covers the approximate region $1.1 < |\eta| < 4.5$. Similar to the CC, the EC is subdivided in terms of EM, FH, CH but there are more types of FH and CH modules (see figure 3.12). In the very forward region ($2.0 \leq |\eta| \leq 4.5$) the towers pass through Electromagnetic (EM), Inner Fine Hadronic (IFH), and Inner Coarse Hadronic (ICH) layers. In the region $1.5 \leq |\eta| \leq 2.0$, the towers pass through EM, IFH, Middle Fine Hadronic

	EM	FH	CH
Rapidity coverage	± 1.2	± 1.0	± 0.6
Number of Modules	32	16	16
Absorber ^a	Uranium	Uranium	Copper
Absorber Thickness (inches)	0.118	0.236	1.625
Argon Gap (inches)	0.09	0.09	0.09
Number of cells per module	21	50	9
Longitudinal depth	$20.5 \lambda_0$	$3.24 \lambda_0$	$2.93 \lambda_0$
Number of readout layers	4	3	1
Cells per readout layer	2,2,7,10	20,16,14	9
Total Radiation lengths	20.5	96.0	32.9
Radiation length per cell	0.975	1.92	3.29
Total Absorption lengths (Λ)	0.76	3.2	3.2
Absorption length per cell	0.036	0.0645	0.317
Sampling Fraction (%)	11.79	6.79	1.45
Segmentation ($\Delta\phi \times \Delta\eta$) ^b	0.1×0.1	0.1×0.1	0.1×0.1
Total Number of readout cells	10,368	3000	1224

Table 3.4: Central Calorimeter Parameters

^aUranium is depleted and FH absorbers contain 1.7% Niobium alloy

^bLayer 3 of the EM has 0.05×0.05

(MFH), and Middle Coarse Hadronic (MCH) layers. And finally, in the region $1.0 \leq |\eta| \leq 1.5$ the towers pass through little or no EM layers (only for $|\eta| \leq 1.2$), but primarily through MCH and Outer Hadronic (OH) layers. Clearly this leaves something of a “hole” with respect to electron coverage (see discussion in section 3.5.3. As for the CC, most of the EC has a segmentation of $\Delta\eta \times \Delta\phi = 0.1 \times 0.1$. However, for $|\eta| > 3.2$ the segmentation becomes increasingly larger reaching a maximum of $\Delta\eta \times \Delta\phi = 0.4 \times 0.4$ [100]. A cross sectional view of the CC and EC is shown in figure 3.13. Many vital statistics

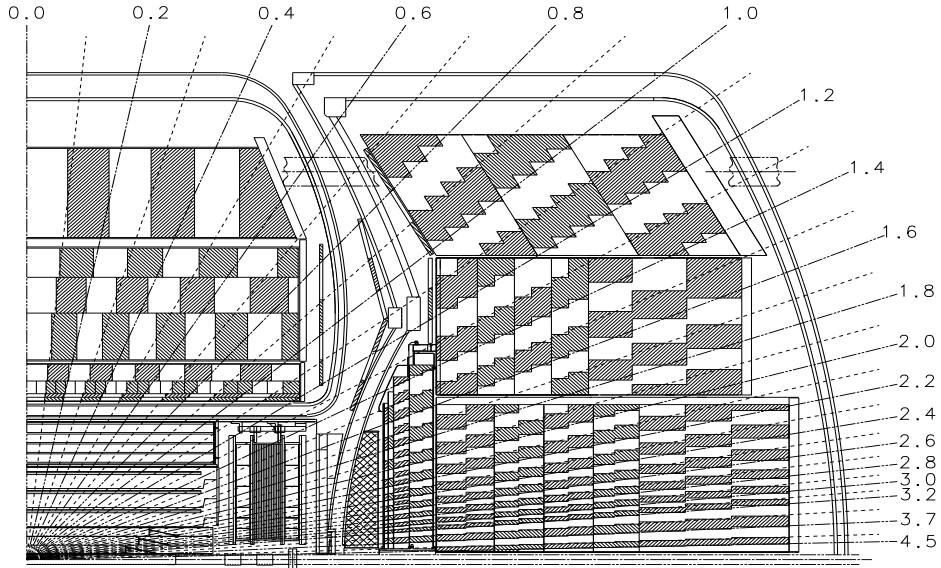


Figure 3.13: Side view of the CC and EC

of the EC are given in table 3.5 [101] [102].

3.5.3 ICD and massless gap detectors

As noted in section 3.5.2 the CC/EC transition region $0.8 \leq |\eta| \leq 1.4$ consists primarily of uninstrumented material (cryostat walls, module end-plates, etc.). Two separate devices, the Intercryostat Detector (ICD) and the massless gaps (MG), have been included to sample the energy which is lost in these uninstrumented regions. The ICD is a set of scintillation counter modules mounted on the CC side of both EC's. On each EC are 384 scintillator tiles of size $\Delta\eta \times \Delta\phi = 0.1 \times 0.1$, matching the “pseudo”-projective towers in the CC and EC. Within both the CC and EC cryostats, mounted on the

	EM	IFH	ICH	MFH	MCH	OH
Rapidity coverage	1.3-3.7	1.6-4.5	2.0-4.5	1.0-1.7	1.3-1.9	0.7-1.4
Number of Modules	1	1	1	16	16	16
Absorber ^a	U	U	SS ^b	U	SS	SS
Absorb Thickness (in)	0.118	0.236	0.236	0.236	1.83	1.83
Argon Gap (in)	0.09	0.082	0.082	0.087	0.087	0.087
No. of cells/module	18	64	12	60	14	24
Longitudinal depth	$20.5X_0$	$4.4\lambda_0$	$4.1\lambda_0$	$3.6\lambda_0$	$4.4\lambda_0$	$4.4\lambda_0$
No. of readout layers	4	4	1	4	1	3
Cells/readout layer	2,2,6,8	16	14	15	12	8
Tot. Rad. lengths	20.5	121.8	32.8	115.5	37.9	65.1
Tot. Absorp. len. (Λ)	0.95	4.9	3.6	4.0	4.1	7.0
Sampling Fraction (%)	11.9	5.7	1.5	6.7	1.6	1.6
$\Delta\phi$ Segmentation ^{c d}	0.1	0.1	0.1	0.1	0.1	0.1
$\Delta\eta$ Segmentation	0.1	0.1	0.1	0.1	0.1	0.1
No. of readout ch. ^e	7488	4288	928	1472	$384 + 64$	$896 + 64$

Table 3.5: End Calorimeter Parameters

^aUranium is depleted and FH (IFH and MFH) absorbers contain 1.7% Niobium alloy

^bstainless steel

^cLayer 3 of the EM has $\Delta\phi \times \Delta\eta = 0.05 \times 0.05$

^dfor $|\eta| > 3.2$, $\Delta\phi \times \Delta\eta = 0.2 \times 0.2$

^eMCH and OH are summed together at $|\eta| \geq 1.4$

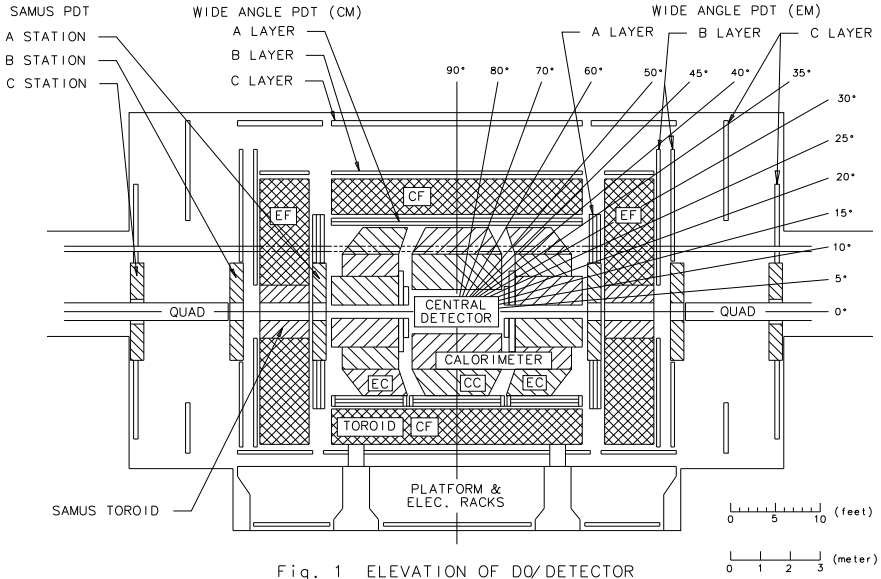


Figure 3.14: Cross Section view of the DØ Muon system

CCFH, ECMH, and ECOH modules, are additional devices, known as Massless Gap (MG) modules. These devices consist simply of two signal boards surrounded, of course, by liquid argon [95] [103]. As expected, the MG have $\Delta\eta \times \Delta\phi = 0.1 \times 0.1$.

3.6 Muon System

Muons are primarily identified by their very penetrating nature. They do not interact strongly and, because they are 200 times heavier than electrons, for energies below ~ 500 GeV do not readily produce electromagnetic showers. They do, however, occasionally produce bremsstrahlung, which in turn initiates an EM shower (see section 5.2.1).

The DØ muon system is built around five iron toroidal magnets, the CF ($|\eta| \leq 1$), two EF ($1 < |\eta| \leq 2.5$), and two SAMUS, Small Angle MUon System toroids ($2.5 < |\eta| \leq 3.6$) (see figure 3.14). Associated with these magnets are several layers of proportional drift tube chambers: one just inside the iron (A layer), one just outside the iron (B layer), and one after an air gap of 1-3 m (C layer) (see figure 3.14). Each of these layers is divided into sublayers of drift tubes: four for the A layer and three each for the B and C layers (see figure 3.15). Due to various practical considerations (i.e. calorimeter and toroid supports), not all regions of $\eta - \phi$ space have full 3 layer (A,B, & C) coverage. The large number of interaction lengths in the calorimeter and muon toroids provide a very clean environment (negligible punchthrough) for the identification and momentum measurement of high P_T muons over most of the η region (see figure 3.16). This allows muons to be identified in the middle of jets with an efficiency much greater than that for electrons. The minimum momentum required for a muon to pass through the calorimeter and iron varies from ~ 3.5 GeV/ c at $\eta = 0$ to ~ 5 GeV/ c at higher η [104]. As can be seen in figure 3.15, the muon system, unlike the other tracking chambers (VTX, CDC, and FDC), has only one wire per drift cell (50 μ m gold plated tungsten). The Field shaping yields a linear space-time relationship to a good approximation. Hits in the bend view (perpendicular to the wires) are determined by measuring the drift time (similar to the technique used in the central tracking chambers). Hits in the other view (parallel to the wires) are obtained by crudely measuring the signal arrival time difference between the two ends of the wire and more precisely with a system of vernier cathode

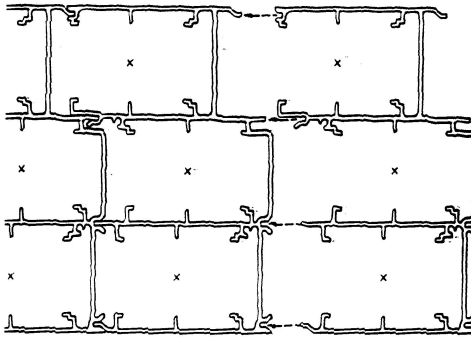


Figure 3.15: Extruded aluminum section from which the “B” and “C” layer PDT chambers are constructed. The “A” layer chamber extrusions are similar but have 4 cells instead of 3.

pads inserted into the top and bottom of each cell [105]. The upper and lower cathode planes are made from two independent electrodes forming the inner and outer portions of a repeating diamond pattern whose repeat distance is 61 cm. The two inner pads of a given cell are added and read independently of the sum of the outer pads. Calculation of the ratio of the sum and difference of inner and outer signals gives a measure of the coordinate along the wire. The resolution of this measurement is $\sim \pm 3$ mm.

As shown in figure 3.17 the B field ($\sim 2T$) is perpendicular to the beam axis. Therefore, muon trajectories are bent in the r-z plane. In order to measure the bend, and thus determine the momentum, the muon trajectory is measured both before and after the iron. The lever arm after the iron is the distance between the B and C layers. Tracks in the A layer are matched to tracks in the central detector and, for isolated muons, often to minimum ionizing traces in the calorimeter. The incident trajectory is then formed from

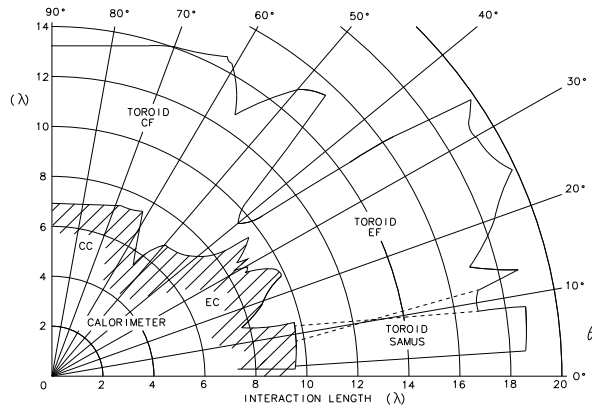


Figure 3.16: Variation in the detector thickness (in interaction lengths) as a function of polar angle

	WAMUS	SAMUS
Rapidity coverage	$ \eta \leq 1.7$	$1.7 \leq \eta \leq 3.6$
Magnetic Field	$2 T$	$2 T$
Number of Chambers	164	6
Interaction lengths	13.4	18.7
bend view resolution ^a	$\pm 0.53 \text{ mm}$	$\pm 0.35 \text{ mm}$
Non-bend resolution	$\pm 3 \text{ mm}$	$\pm 0.35 \text{ mm}$
$\delta P/P$ ^b	18%	18%
Gas	Ar(90%)-CF ₄ (5%)-CO ₂ (5%)	CF ₄ (90%)-CH ₄ (10%)
Avg. Drift Velocity	$6.5 \text{ cm}/\mu\text{s}$	$9.7 \text{ cm}/\mu\text{s}$
Anode Wire Voltage	$+4.56 kV$	$+4.0 kV$
Cathode Pad Voltage	$+2.3 kV$	—
Number of cells	11,386	5308

Table 3.6: Muon System Parameters

^athe diffusion limit is $0.2 - 0.3 \text{ mm}$

^bmultiple scattering limit, assumes 100% chamber efficiency

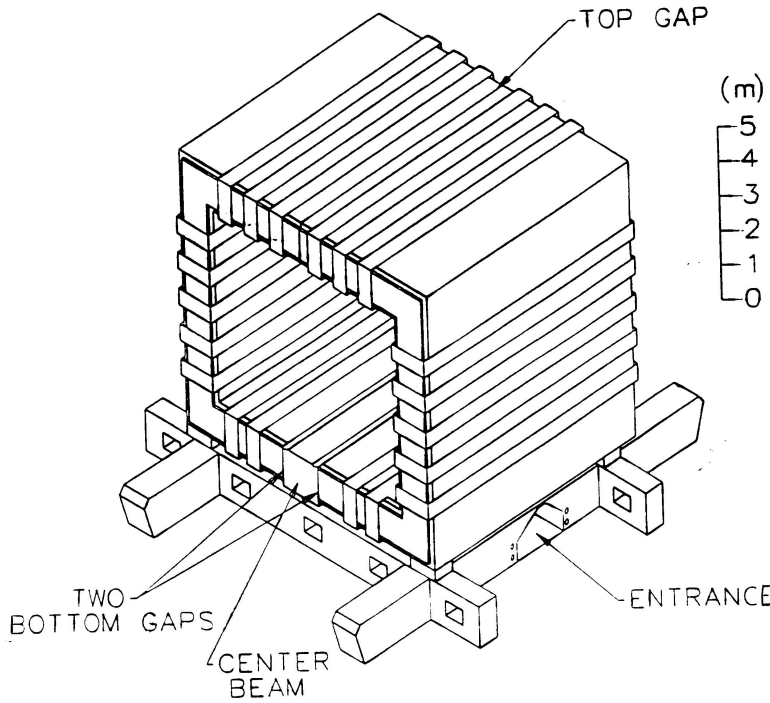


Figure 3.17: Perspective view of the CF toroid

a combination of the primary interaction point, the CD match, and the muon A layer track. The momentum resolution is parameterized as

$$\left(\frac{\delta P}{P}\right)^2 = (0.18)^2 + (0.01P)^2.$$

Multiple coulomb scattering in the iron limits the relative momentum resolution to $\geq 18\%$ up to the limit imposed by the bend coordinate resolution of the proportional drift tubes. The drift resolution is 0.53 mm and the present uncertainty on the “chamber” alignment is ~ 3 mm [106].

Many vital statistics of the muon system are given in table 3.6 [104]. The D \emptyset muon system is discussed in detail in [104] and [107].

3.7 DAQ/Trigger System

A typical Luminosity during run 1A was $5 \times 10^{30} \text{cm}^{-2}\text{s}^{-1}$. At a center of mass energy of 1.8 TeV the total cross section (elastic plus inelastic) for $p\bar{p} \rightarrow X$ is approximately 70 mb ($= 7 \times 10^{-26} \text{cm}^2$) [108]. Therefore, the rate of $p\bar{p}$ interactions is 350,000 Hz. The vast majority of these interactions are uninteresting. Therefore, DØ has a multilevel triggering system which is designed to filter out the unwanted events and keep the interesting ones. The online part of this system is divided into four parts: (1) Level Ø, (2) Level 1, (3) Level 1.5, and (4) Level 2. A simplified overview of the DØ DAQ/trigger system is shown in figure 3.18. This system is discussed in great detail in [109] and [110].

3.7.1 LØ

Level Ø is a series of hodoscopes located close to the beampipe in the forward regions. These hodoscopes are strips of “criss-crossed” scintillators mounted on the surfaces of the end calorimeters. These detectors have partial coverage in the range $1.9 < |\eta| < 4.3$ and almost full coverage in the range $2.3 < |\eta| < 3.9$ [110]. The scintillators are read out through photomultiplier tubes. Level Ø is “triggered” by the presence of simultaneous “activity” in the forward and backward regions. Typically such activity consists of forward particles which signal the presence of a $p\bar{p}$ collision (the spectator quarks and gluons form jets with very little transverse momentum but lots of forward momentum). A measurement of the arrival times at the two ends allows the

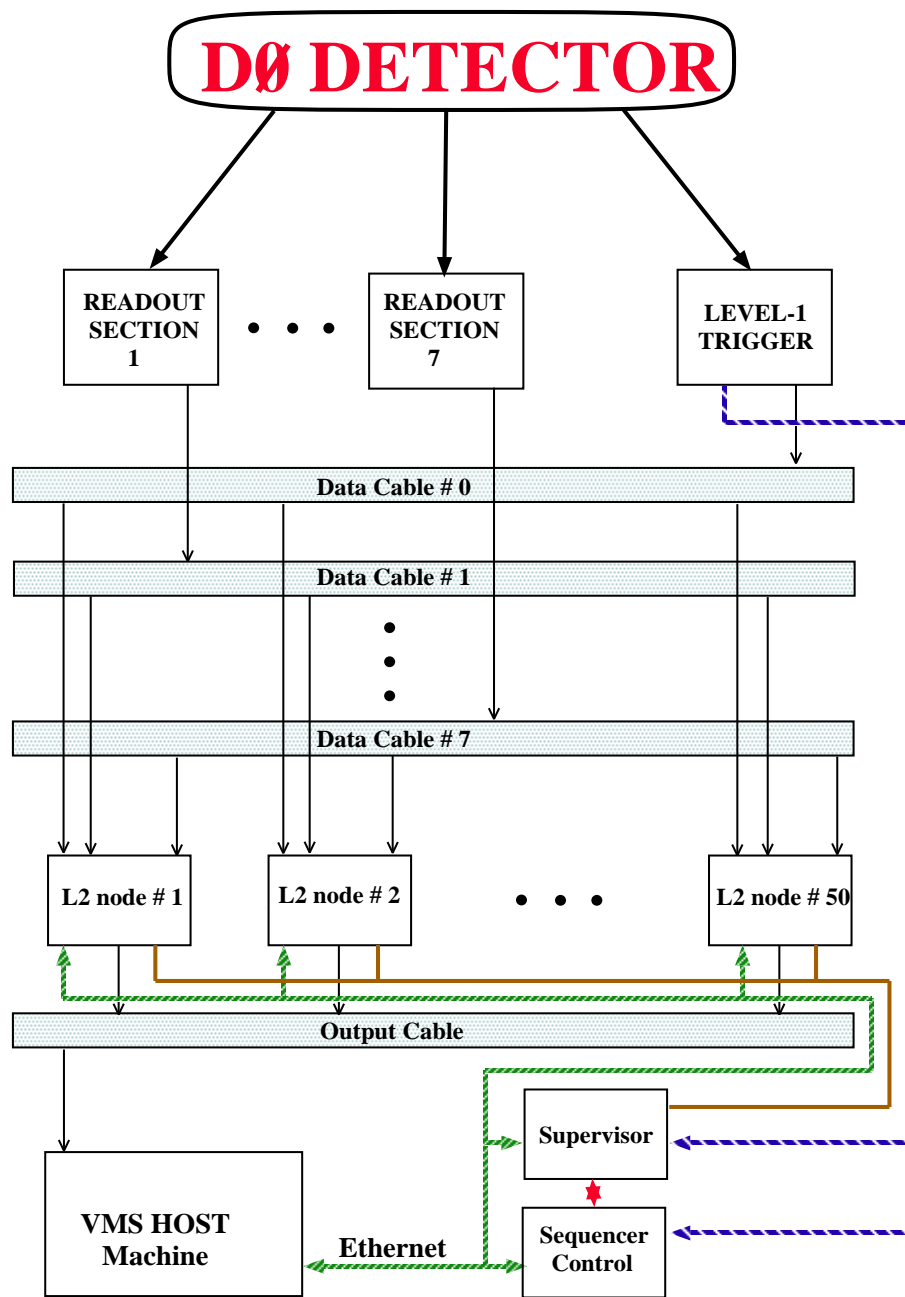


Figure 3.18: Simplified View of DAQ/Trigger System

level \emptyset detector to determine the z position of interaction point. For single interactions (one hard scattering per bunch crossing) the resolution on this measurement is ± 3.5 cm. For multiple interactions the resolution is ± 6 cm [111].

3.7.2 L1

The Level 1 “Trigger Framework” processes digital signals from Level \emptyset , the calorimeter (through the calorimeter level 1 trigger [110] - see below), the muon system (through the muon level 1 trigger [110] - see below), the TRD (through the TRD trigger which was not implemented during run 1A), and timing signals from the accelerator and the host computer. In the time between beam crossings, $3.5 \mu\text{s}$, the Trigger Framework must “decide” whether to keep or reject an event. This decision is *true* if the event passes one or more of the 32 available trigger *bits* (the $e\mu$ analysis requires an OR of three of these trigger bits - see section 6.2). Each of these *bits* is a logical combination of 256 programmable AND-OR input terms. Typical input terms include: Level \emptyset vertex position, calorimeter energy, and number of muon candidates [112]. An overview of the Level 1 trigger system is shown in figure 3.19.

As mentioned above, the level 1 calorimeter trigger feeds digital information into the trigger framework. This digital information is based on the analog information which comes from the first stage of the calorimeter electronics (BLS circuits [110]). These analog signals are read out in terms of “trigger towers”. A trigger tower is formed by summing the output from all

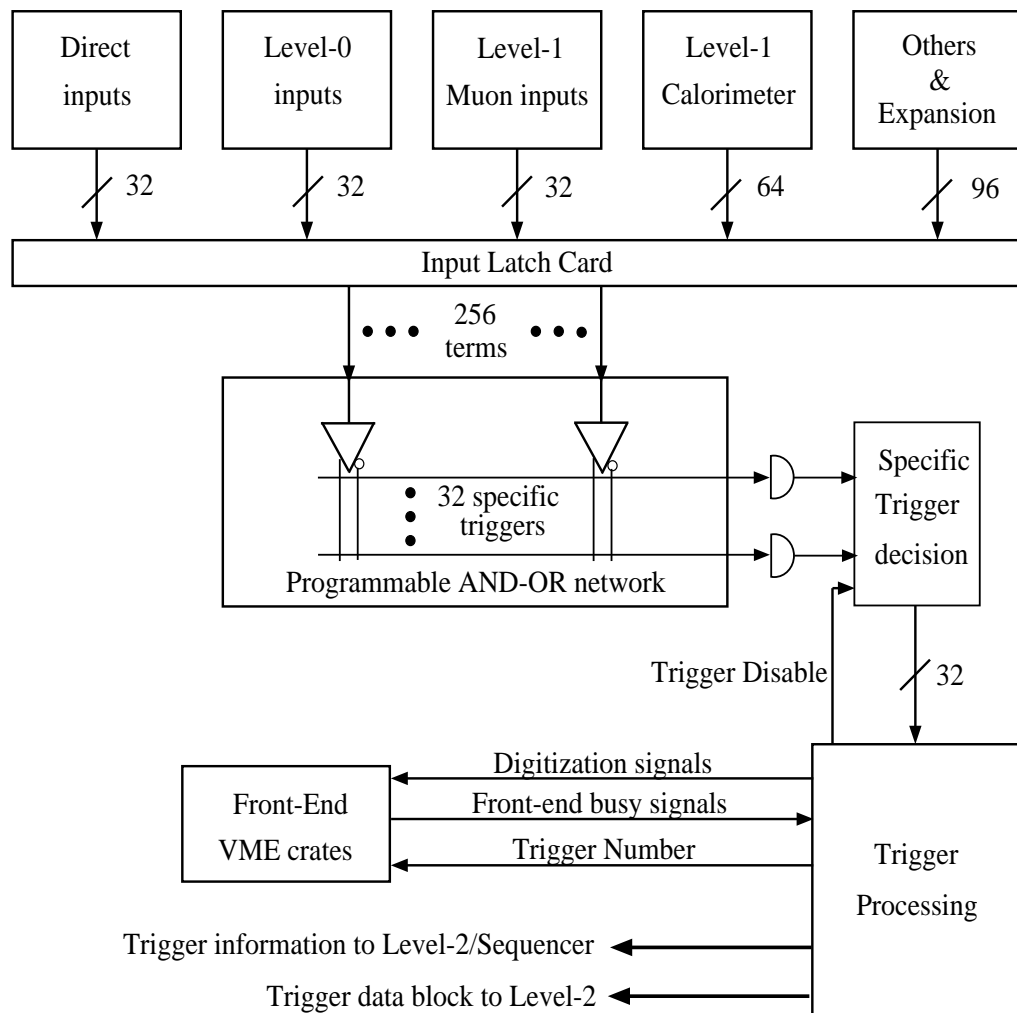


Figure 3.19: Level 1 processing stages

the cells in a region which is $\Delta\eta \times \Delta\phi = 0.2 \times 0.2$ for all EM depths, or all hadronic depths [113]. This is done by using special fast readouts within the first stage calorimeter electronics.

As with the level 1 calorimeter trigger the level 1 muon trigger provides digital information to the Trigger Framework. This information is based on one “latch” bit for each of the 16,700 drift cells of the muon system (a latch bit is *true* if its associated cell has been fired). This gives the bend coordinate of hit drift cells (with a granularity of 10 cm). The final steps in the muon electronics path consists of 24 Motorola 68020 processors and a series of 200 module address cards [110]. It is at this stage that a bit pattern is produced which gives a “coarse” description of the muon content of the event. This bit pattern is then passed on to the trigger framework. An additional muon trigger, level 1.5, provides more precise muon track and P_T information directly to level 2 but at present is only installed for a limited η range and is therefore not used for the $e\mu$ analysis.

3.7.3 L2

Once an event passes level 1 it is shipped to the level 2 system (for run 1A the maximum rate from level 1 into level 2 was 200 Hz). Unlike the first two hardware triggers (L \emptyset and L1), level 2 is a software trigger. The system is based on a farm of VAXstation 4000-60’s (48 for run 1A but to be upgraded for run 1B) which collect and process much of the raw data (including information from the level \emptyset and level 1), perform a fast preliminary reconstruction, and

decide whether or not the event should be kept. For this decision to be true the event must satisfy one of the 128 software filters (the $e\mu$ analysis requires an OR of three of these filters - see section 6.2). These filters are built out of a series of “tools” or algorithms. Typical algorithms are those which look for electromagnetic jets, hadronic jets, muons, missing E_T , etc.

Upon reaching level 2, all of the raw data for the event is put into DØ Zebra format [114]. Zebra is an extension of FORTRAN which allows for dynamic data structuring (i.e. allows data memory usage to be redistributed as the program is running). Then using code which is quite similar to what is used offline certain aspects of the event are reconstructed. The 128 software filters are based on the results of this preliminary reconstruction. If an event passes one or more of these filters, all of the raw data (now in Zebra format) including information from the level Ø, level 1, and level 2 is passed to the host cluster, temporarily stored on hard disk, and then transferred to 8mm tape (see figure 3.18. For run 1A the level 2 produced raw data in multiple data streams. The two primary data streams were the “all” stream and the “expressline”. The “expressline” consisted of those events which were judged, based on the level 2 information, to be of highest interest ($\sim 10\%$ of the full data set). The “all” stream consisted of essentially the full sample (including the complete expressline). The rate from level 2 to the host was dependent on the choice data stream: the all stream wrote at 1-2 Hz whereas the expressline was limited to ~ 0.3 Hz. The $e\mu$ analysis covers the expressline data only.

3.8 Offline Reconstruction - DØRECO

Due to the small amount time, memory, and CPU power available, the “preliminary” reconstruction done in level 2 does not consider a great deal of more subtle information (full tracking, full shower shape, etc) and therefore should not be treated as a final result. The task of performing the full reconstruction for a DØ event is done offline by the software package DØRECO. This package contains more than 150,000 lines of code (excluding utility libraries) [115] and has been “under construction” for many years. A program of this size and complexity (and with many different “physicists as programmers” from all over the globe) undoubtedly requires a significant amount of debugging and testing. In addition, with so many bright and enthusiastic people involved, there is a continuous tendency to implement improvements which themselves require debugging and testing. Indeed run 1A saw many versions of the DØRECO (from version 10.12 to version 11.19). The primary purpose of DØRECO is to “interpret” the raw data (composed of analog and digital signals) in light of all the *a priori* information about the detector (surveys, calibrations, etc.) and provide as accurately as possible all necessary information on the final objects in the event (electrons, muons, jets, etc.). DØRECO produces two types of output files:

- STA files - contain the raw data plus the output from the full reconstruction. These files are quite large (typically 600 kilobytes/event) and are therefore used primarily for event display and reRECOing of events [115]. The $e\mu$ analysis benefitted greatly from having a small number of

candidate events (see section 6.3.1) and could therefore keep the STA’s on local disk for easy event display and rapid reREConstruction (with the latest version of DØRECO).

- DST (Data Summary Tape) files - contains a compressed version of the full reconstruction. A DST contains summaries of CD and muon tracks, calorimeter clusters, all parameters for electron, photon, muon, tau, and jet candidates, and all parameters relevant to the missing E_T [115].

In order to perform its task DØRECO makes an assignment of particle id (i.e. jet, e , γ , μ) to the various entities in an event. In order to accommodate various analyses with different concerns, this particle id is based on relatively loose criteria. However, DØRECO includes along with each object a number of “quality flags” so that there can be some degree of standardization among the particle id algorithms used by different analysis groups. The following paragraphs discuss the particle id and associated “quality flags” output by DØRECO.

Jets DØRECO constructs jets according to several different algorithms. One algorithm is the nearest neighbor algorithm and is not used by the $e\mu$ analysis. The other approach is known as the cone algorithm and is most commonly used for three different cone sizes ($\Delta R (= \sqrt{\Delta\eta^2 \times \Delta\phi^2}) = 0.3, 0.5, \text{ and } 0.7$). The cone construction works as follows: Starting from an E_T ordered list of jet towers (vertex corrected), the towers ($> 1 \text{ GeV}$) are grouped into preclusters (out to $\Delta R \sim 0.3$). The energy in cones of $\Delta R = 0.3, 0.5, \text{ or } 0.7$ around

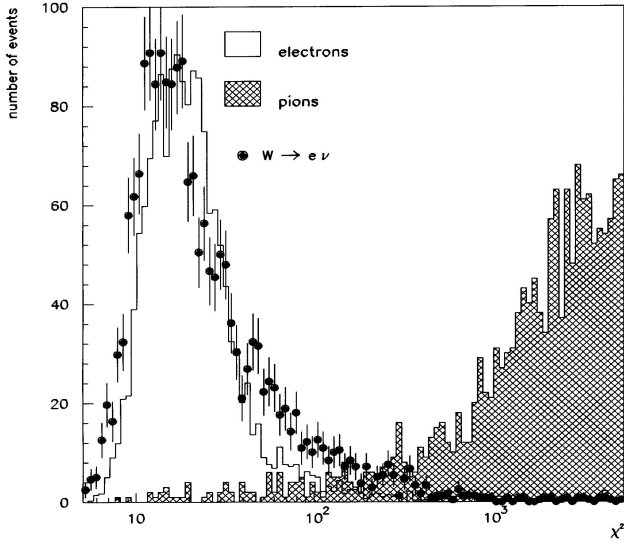


Figure 3.20: χ^2 distribution for test beam electrons (unshaded), test beam pions (shaded), and electrons from W 's (dots)

the precluster center is summed and a new “ E_T weighted” center is obtained. Starting with this new center the process is repeated several times until the center is stable. Once the jet is formed DØRECO requires that the E_T be greater than 8 GeV if the object is to be defined as a jet. Clearly, as with all reconstructed objects, the definition of a jet is not clear cut. For example, a 0.7 cone jet which just passes the E_T threshold will probably not survive as a 0.3 cone jet. The $e\mu$ analysis uses 0.5 cone jets.

Photon/Electron Whereas the nearest-neighbor algorithm is not so commonly used for jet reconstruction it is the algorithm of choice for electron/photon id. The procedure is as follows: All EM towers are first ordered in decreasing

E_T . An EM tower is here defined to be the four layers of the EM calorimeter plus the first layer of the fine hadronic calorimeter. The clustering is based on a purely local algorithm. One loops over all the towers above a threshold of $E_T > 50$ MeV, and finds the nearest-neighbor tower which has the highest transverse energy. These neighboring towers are then linked together. If no nearest-neighbors exist, the cluster is defined by the single tower, else it is the ensemble of towers which have been linked locally [116] [117]. Clusters with a total E_T of less than 1.5 GeV are not included. Once the cluster formation is complete, DØRECO requires that the cluster have at least 90% of its energy in the electromagnetic calorimeter. DØRECO also requires that the fraction of energy outside the central tower must be less than 60%. The cluster centroid is calculated from a $\log(E)$ weighted mean of the cell positions of EM layer 3 (recall from section 3.5 that layer 3 is most finely segmented in $\Delta\eta \times \Delta\phi$). For electrons DØRECO requires that there be at least one matching track in the CD within a road of $\Delta\eta \times \Delta\phi = 0.1 \times 0.1$ which is centered on the reconstructed vertex and the cluster. It is clear that DØRECO makes no attempt to distinguish between electrons/photons and jets, and indeed a high energy electron is most always found as a jet as well. The $e\mu$ analysis corrects for this in the next stage of particle id (see section 4.2.1).

This selection is necessarily loose and DØRECO passes along many quality indicators to allow the user to make tighter cuts for specific analyses. The $e\mu$ analysis takes advantage of 3 of the available indicators:

- cluster EM fraction

$$\frac{\text{EM Energy}}{\text{Total Energy}}$$

DØRECO requires that this be greater than or equal to 0.90 for electron and photon candidates.

- Cluster isolation

$$\frac{E_{\text{Tot}}(\text{cone 0.4}) - E_{EM}(\text{cone 0.2})}{E_{EM}(\text{cone 0.2})}$$

- Cluster shape. The development of electromagnetic and hadronic showers are sufficiently different that shower shape information can be used to differentiate between electrons (or photons) and hadrons. To exploit these differences to the greatest degree DØ uses both longitudinal and transverse shower shapes, and also takes into account correlations between energy deposits in the calorimeter cells [118] [119]. A covariance matrix technique is used to compare the shape of a given shower with the shower shape expected from electrons from both testbeam data and Monte Carlo. The covariance matrix, for a sample of N electrons or photons is defined

$$M_{ij} = \frac{1}{N} \sum_{n=1}^N (x_i^n - \langle x_i \rangle)(x_j^n - \langle x_j \rangle),$$

where x_i^n is the value of observable i for electron (or photon) n and $\langle x_i \rangle$ is the mean value of the observable i for the sample. There are a total of 41 such observables which include total energy fractions in EM layers 1, 2, and 4, and FH layer 1, fractional energy in 6×6 cells in EM

layer 3, the z position of the vertex. Defining $H \equiv M^{-1}$, the degree to which a given shower is electromagnetic is determined by computing the covariance parameter

$$\chi^2 = \sum_{i,j} (x_i^k - \langle x_i \rangle) H_{ij} (x_j^k - \langle x_j \rangle).$$

As seen in figure 3.20, cutting on χ^2 provides good separation between electrons (or photons) and pions.

Muon Muon candidate selection (at the DØRECO level) proceeds via three primary steps [120]:

- Hit Sorting - Takes the raw data (hits, timing signals, analog pulses, etc.) and puts it together with the calibration and survey constants to create points in the DØ global coordinate system.
- pattern recognition - Takes the hits in the DØ global coordinate system and using various pattern recognition techniques recognizes that certain groups of hits make up a muon track. A preliminary fit is then performed (note that thus far only information from the muon system has been used). The momentum of each track is corrected for the average expected muon energy deposition in the calorimeter (estimated from Monte Carlo detector simulations), that is, $P^\mu = P^{\mu, \text{meas}} + E^{\text{dep}}$.
- Global Fitting - Takes the muon track and links it with appropriate information from the central tracking system (and in the future the calorimeter as well) and performs a complete least squares fit [121].

Due to the large number of accidental hits in the muon chambers, many “fake” muon tracks will satisfy the above criteria. Therefore, as is the case with electrons and photons, DØRECO passes along many quality indicators as well. These indicators can be divided into three classes: (1) Cosmic ray flags; (2) Muon track quality (relying on muon and CD track information as well as Calorimeter mip deposition information); and (3) Fiducial quantities (i.e. did the muon go through the gap between the toroids). A breakdown of these classes is given in [122].

Missing Et Since neutrinos are not directly detected, their presence is inferred by the existence of “missing energy”. Conservation of momentum is assumed and the vector sum of all observed entities is calculated; any deviation from zero is defined as missing momentum. However, due to the fact that the forward component of the final state cannot be accurately measured (due to highly energetic particles escaping down the beam pipe), missing momentum can only be calculated in the transverse plane. DØRECO produces three different types of missing transverse momentum measurements. The first is based on calorimeter measurements only, the second supplements this with information from the ICD and massless gaps, and the third incorporates muons into the calculation.

Since a calorimeter measures energy and not momentum, it is customary to define the calorimeter missing transverse energy as follows [123]:

$$\not{E}_x^{\text{cal}} = - \sum_{i=1}^n E_i \sin\theta_i \cos\phi_i$$

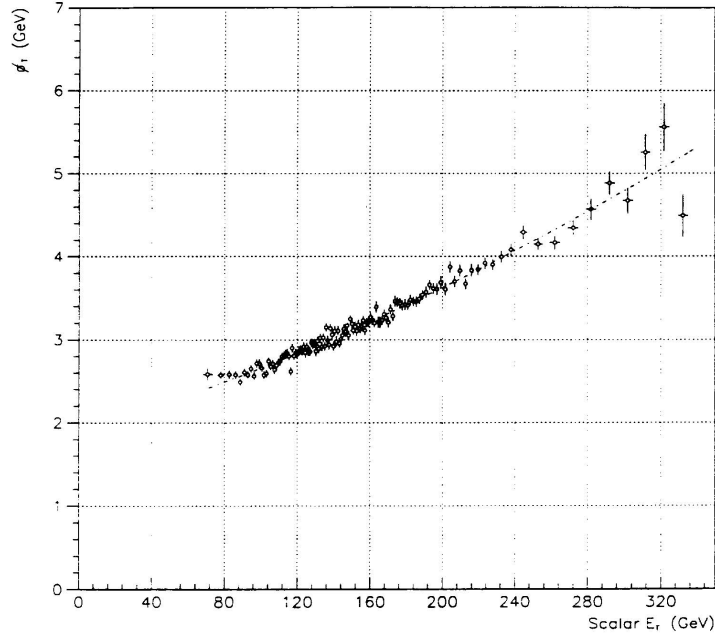


Figure 3.21: Calorimeter \cancel{E}_T resolution function for the DØ detector for QCD dijet data

$$\cancel{E}_y^{\text{cal}} = - \sum_{i=1}^n E_i \sin\theta_i \sin\phi_i$$

$$\cancel{E}_T^{\text{cal}} = \sqrt{(\cancel{E}_x^{\text{cal}})^2 + (\cancel{E}_y^{\text{cal}})^2}$$

where i runs over all cells in the calorimeter, E_i is the energy deposited in cell i with θ_i and ϕ_i as the polar and azimuthal angles, respectively, of the center of cell i as measured from the vertex of the event. For the ICD and massless gap correction to the calorimeter missing E_T the cells in the ICD and massless gap are included in the summed cells. It is this value of \cancel{E}_T which is typically quoted as the calorimeter missing E_T . For the muon corrected \cancel{E}_T the momenta of all muons are added vectorially to the above sum, while

the expected muon energy deposition (estimated from detector Monte Carlo studies) in the calorimeter must be subtracted since it has already been accounted for in the calorimeter sum. Therefore, the muon corrected missing E_T is defined as follows:

$$\begin{aligned}\cancel{E}_x &= \cancel{E}_x^{cal} - \sum_{\mu} (P^{\mu} - E^{dep}) \sin \theta_{\mu} \cos \phi_{\mu} \\ \cancel{E}_y &= \cancel{E}_y^{cal} - \sum_{\mu} (P^{\mu} - E^{dep}) \sin \theta_{\mu} \sin \phi_{\mu} \\ \cancel{E}_T &= \sqrt{\cancel{E}_x^2 + \cancel{E}_y^2}\end{aligned}$$

where P_{μ} , E^{dep} , θ_{μ} , and ϕ_{μ} are the muon momentum, expected muon calorimeter energy deposition, and muon's polar and azimuthal angles, respectively,

The \cancel{E}_T resolution of the DØ calorimeter has been parameterized as [124]

$$\phi_T = a + b \cdot S_T + c \cdot S_T^2$$

with $a = (1.89 \pm 0.05) \text{ GeV}$, $b = (6.7 \pm 0.7) \times 10^{-3}$, $c = (9.9 \pm 2.1) \times 10^{-6} \text{ GeV}^{-1}$, and where S_T is the summed transverse energy in the calorimeter. This parameterization is based on QCD dijet data. The \cancel{E}_T resolution as a function of S_T is given in figure 3.21 [124].

Chapter 4

TOP-LEPTONS: the analysis package

As noted in section 3.8, DØRECO converts the raw data into loosely defined physics objects. To obtain a tighter, analysis specific, definition of these physics objects and to perform the selection of interesting events, an additional analysis package is necessary. At this stage the $e\mu$ analysis relies on the software package TOP-LEPTONS [122].

4.1 Overview

The TOP-LEPTONS package was initially written for use in the top to dilepton analyses but was later expanded to cover several other physics topics. The package is very general and is used by several different physics analyses (including $t\bar{t} \rightarrow \mu\mu$, $t\bar{t} \rightarrow \mu + \text{jets}$, and various topics in WZ and b physics). It is a single package that can read DST's or STA's and will operate on real or Monte Carlo data. A package of such complexity requires many “switches” to control the output, set the thresholds, etc. TOP-LEPTONS

uses a set of ASCII files known as RCP (Run Control Parameter) files for this purpose. Such files are standard within the DØ software environment. The great advantage to such files is that the program does not have to be recompiled and relinked each time a switch or threshold is changed. TOP-LEPTONS is controlled by 5 of these files:

- TOP-LEPTONS : contains all analysis level thresholds, switches to select physics channel finder(s), and controls for choosing the types of output (summaries, event dumps, histograms, ntuples, etc.)
- CLEANEM : contains all electron/photon id thresholds and switches
- Muon-select : contains all muon id thresholds and switches
- QCD-Jet-correction : contains input values for jet corrections (see section 4.3)
- Bad-run : contains the list of collider runs where some part of the detector or data aquisition was known to be functioning incorrectly (these runs are discarded from the final data set)

As can be seen in table 4.1, the TOP-LEPTONS package consists of three primary parts: The Initialization, The Event Loop, and The End. The Initialization and End perform administrative tasks (booking histograms, closing ntuples, etc.). Each event which is being analyzed passes through the event loop. The specific calls made during the event loop depend on the settings in the TOP-LEPTONS run control file. The overall structure is as follows: (1) If specified in the run control file, check on run number, trigger bits passed,

and vertex position; (2) Perform corrections (see section 4.3) to RECO electrons and then select those which pass the CLEANEM electron thresholds and settings; (3) Perform corrections (see section 4.3) to RECO photons and then select those which pass the CLEANEM photon thresholds and settings; (4) Perform corrections on the jets found by DØRECO; (5) Select those jets which pass the jet thresholds and settings specified in the TOP-LEPTONS run control file; (6) Select those muons which pass the muon thresholds and settings specified in the Muon-select run control file; (7) Correct the missing E_t found by DØRECO; (8) Subject the entities found in (1)-(7) to the criteria specified for the desired physics finder(s).

It is the proliferation of these physics finders which has put TOP-LEPTONS into widespread use. The available finders are many: $t\bar{t} \rightarrow e\mu$, $t\bar{t} \rightarrow ee$, $t\bar{t} \rightarrow \mu\mu$, $t\bar{t} \rightarrow e + \text{jets}$, $t\bar{t} \rightarrow \mu + \text{jets}$, $W \rightarrow e\nu_e$, $W \rightarrow \mu\nu_\mu$, $Z \rightarrow ee$, $Z \rightarrow \mu\mu$, $W\gamma \rightarrow e\nu_e\gamma$, $W\gamma \rightarrow \mu\nu_\mu\gamma$, $WW \rightarrow e\nu_e\mu\nu_\mu$, $WW \rightarrow e\nu_e e\nu_e$, $WW \rightarrow \mu\nu_\mu \mu\nu_\mu$, and QCD $\rightarrow e\mu$. This large community of users, being considerably larger than the one or two individuals typical of a single analysis, has allowed TOP-LEPTONS to undergo greater scrutiny, more debugging, and receive more enhancements than would otherwise have been the case.

4.2 Particle ID

As seen in section 4.1, a large part of TOP-LEPTONS is devoted to performing particle id beyond that done in DØRECO. Note that before any offline selection can be made one must decide how the quantities of interest

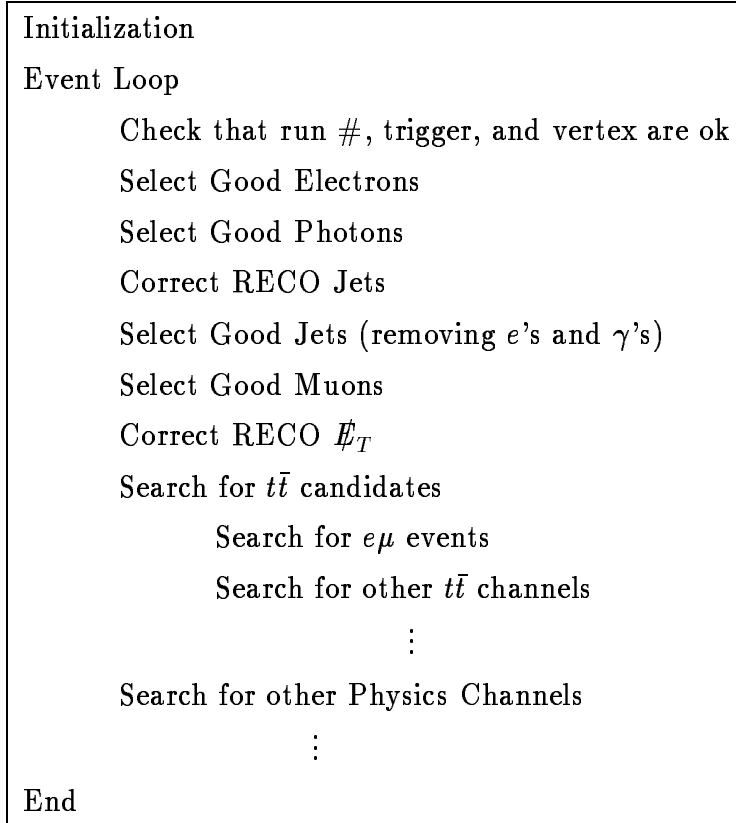


Table 4.1: Simplified schematic view of TOP-LEPTONS

are defined; DØRECO does the first (loose) stage of this. Since the final result will depend critically on what criteria are used for selecting electrons, photons, muons, and jets, these definitions must be chosen with great care. The following sections describe the choices made for the $e\mu$ analysis.

4.2.1 Electron/Photon

The initial stages of the $e\mu$ analysis did not distinguish between electrons and photons. The primary reason for this was so that no “good” events were lost due to tracking inefficiencies. However, the final stage of the analysis does

indeed require electrons.

The criteria DØRECO uses to select photons and electrons is discussed in section 3.8. The quality flags which DØRECO passes along are reviewed as well. TOP-LEPTONS makes use of the standard DØ electron/photon package “CLEANEM” to perform the next level of selection based on these quality flags. For the $e\mu$ selection the photon requirements are as follows:

- require that calorimeter cluster have high EM fraction (this is actually done by DØRECO)

$$\frac{\text{EM Energy}}{\text{Total Energy}} \geq 0.90$$

- require that the cluster be isolated

$$\frac{E_{\text{Tot}}(\text{cone 0.4}) - E_{EM}(\text{cone 0.2})}{E_{EM}(\text{cone 0.2})} \leq 0.10$$

- require that cluster shape be consistent with that found in electron test-beam and mc studies (see section 3.8). This is done by using a covariance (H) matrix χ^2 test:

$$\chi_H^2 < 100 \quad \text{for} \quad |\eta| < 1.2$$

$$\chi_H^2 < 200 \quad \text{for} \quad 1.2 < |\eta| < 4.0$$

Electrons have identical cluster requirements but require, in addition, a CD track match. Although the track match significance is passed along with the electron candidates the $e\mu$ analysis relies only on the track match provided by DØRECO (see section 3.8). Also, in the final stages of the analysis, background (from fake electrons, see section 5.2.1) suppression is optimized by restricting electron and photon candidates to have $|\eta| < 2.5$.

4.2.2 Muon

As noted in section 3.8, the criteria used by DØRECO is necessarily very loose. There are many quality indicators which DØRECO passes along with each muon candidate which allow the user to make a more restrictive selection. TOP-LEPTONS performs this selection using the standard DØ muon package, CLEANMU. In 3.8 these indicators were broken up into three classes. The muon id criteria used by the $e\mu$ analysis in each class are as follows:

- Cosmic Ray Rejection : Four separate cuts are used to suppress cosmics
 1. Reject tracks and hits which are back to back (in θ “and” ϕ). During the later part of run 1A this cut was made in Level 2 as well.
 2. Reject tracks which cross octant boundaries. Such tracks cannot come from the vertex and must therefore be cosmics or accidentals.
 3. Reject tracks which have back to back (in both θ “and” ϕ) depositions in the calorimeter which are consistent with a muon mip trace. This is to remove cosmic ray muons which range out in the calorimeter and are not seen by the muon system. This cut is done with a combination of software selection and eye-scan verification.
 4. Require that the muon track be consistent with the primary vertex. This is done by making a 22 cm cut on the 3d impact parameter which is formed by extrapolating the track segment found by the muon chambers back to the interaction region and calculating the minimum distance to the reconstructed vertex (found by the CD).

The cut has been optimized by studying single muon and cosmic ray tracks with momenta greater than $7 \text{ GeV}/c$.

- Muon Track Quality : Several criteria are used to ensure that only “good” muons are kept. First the requirement is made that each track segment have a good χ^2 . This implies that the segment is consistent with the reconstructed vertex in both the bend and non-bend views. Further verification requires that the track be consistent with information from the central tracking chambers and the calorimeter. This is done by requiring signals in the calorimeter which are consistent with the passage of a 1 mip track in the direction of the muon chamber track. To determine energy deposition a sum is performed of the calorimeter cells traversed by the muon and their two nearest neighbors. The threshold is different, depending on whether or not a matching CD track exists:

- a. For muon track segments which match to a CD track,

Calorimeter muon energy deposition $> 0.5 \text{ GeV}$.

- b. For muon track segments with no matching CD track,

Calorimeter muon energy deposition $> 1.5 \text{ GeV}$.

Both a. and b. are included to improve the acceptance for muons which pass through the “corner” region and do not traverse enough of either the CDC or FDC to be reconstructed as a track. The increased mip energy threshold is needed to reject against residual cosmic ray and combinatoric fake muon tracks from the CF-EF transition region.

- Fiducial Requirements : Muons which pass through the thin part of the iron (and thus through an insufficient amount of magnetic field) will be poorly measured and could possibly be due to punchthrough. To reject such muons a cut is made on the minimal value of the total amount of magnetic field “seen” by the muon:

$$\int B \cdot dl > 0.55 \text{ Tm}$$

This effectively removes tracks which pass through the inter-toroid gaps ($0.8 < |\eta| < 1.0$). Since the detector is only ~ 9 interaction lengths at this point (it is typically 13-18 interaction lengths elsewhere - see figure 3.16) there is also a significant increase in jet leakage and punchthrough in this region. Therefore, this cut also serves to remove background from this source. In addition, the $e\mu$ analysis rejects muons with $\eta > 1.7$. This is because of the large number of accidentals which appear in the forward region (which leads to uncertainties in trigger and reconstruction efficiencies). Furthermore, the leptons from top decay are expected to be central so this restriction does not have a significant effect on the acceptance.

4.2.3 Jets

As covered in section 3.8, DØRECO finds electrons and photons as jets. Therefore, after correcting the jet energy (see section 4.3), TOP-LEPTONS removes from the analysis all jets which match (in η and ϕ) to an electron or photon. Unlike the case for electrons, photons, and muons, DØRECO does

not pass along a large number of quality indicators for jets. The user may select jets on the basis of four jet definitions: (1) 0.7 cone algorithm, (2) 0.5 cone algorithm, (3) 0.3 cone algorithm, and (4) nearest neighbor algorithm. In order to minimize the probability of jet merging and the selection of soft “fake jets” the $e\mu$ analysis uses the $\Delta R = 0.5$ cone jet algorithm for jet finding. The minimum E_T threshold for such an object to be classified as a jet is 8 GeV. In order to avoid “edge” effects in jet finding in the very forward region the initial $e\mu$ analysis restricted jets to be within the detector eta range $|\eta| < 4.0$. To reduce QCD background and maintain consistency with the ee analysis, the later stages of the $e\mu$ further restricted jets to $|\eta| < 2.5$. This cut has no effect on the top acceptance.

4.2.4 Determination of \cancel{E}_T

Due to the very loose muon definition within DØRECO, it is often the case that the muon corrected missing E_T is calculated incorrectly since it may include fake muons. TOP-LEPTONS attacks this problem by recalculating the muon corrected missing E_T using only validated muon tracks. If the settings in the TOP-LEPTONS run control file indicate that corrections should be made (see sections 4.1 and 4.3), TOP-LEPTONS correctly includes these corrections in the recalculation of the muon corrected missing E_T .

4.3 Corrections

A number of deficiencies are known to exist for the output produced by DØRECO. While correction routines exist, the relatively long lead time involved in safely installing new code into DØRECO has precluded their inclusion at this time. Therefore, these corrections must be made to the DØRECO output. TOP-LEPTONS implements a number of these routines to correct both real and Monte Carlo data (although not in the same way).

4.3.1 Data

Unfortunately, the jet and electromagnetic energy scales used by DØRECO to translate calorimeter response into “observed” energy lead to results which are inconsistent with known physics (i.e. E_T balance in direct photon events, W and Z mass, etc.). Imprecise energy scales were expected prior to construction and provided the impetus for the detailed calibration techniques employed by DØ. The corrections to the jet energy scale and the electromagnetic energy scale are performed separately.

By requiring E_T balance for direct photon events (events where a photon is back to back with a jet) in real data, a “true” jet energy scale has been determined. It is assumed that the “true” $\langle \cancel{E}_{x,y} \rangle$ is ~ 0 and that the electromagnetic response is correctly calibrated (this is not entirely correct, see below). Therefore, the average measured \cancel{E}_T is assumed to be due to incorrect response of the calorimeter to the jet as compared its response to the photon. That is, for the jet, the difference between the measured energy (E_T^{jet}) and

the correct energy (E_T^{corr}) is equal to the component of the missing E_T vector along the direction of the jet (\hat{n}_T^{jet}),

$$\vec{E}_T \cdot \hat{n}_T^{\text{jet}} = E_T^{\text{corr}} - E_T^{\text{jet}}.$$

The correction factor (f^c) which is needed to convert from measured jet energy to corrected jet energy is defined by $E_T^{\text{corr}} \equiv f^c \cdot E_T^{\text{jet}}$. Therefore,

$$f^c = 1 + \frac{\vec{E}_T \cdot \hat{n}_T^{\text{jet}}}{E_T^{\text{jet}}} = 1 + \text{MPF},$$

where MPF is known as the missing E_T projection fraction. These correction factors vary with η and jet E_T . TOP-LEPTONS selects the relevant quantities from the QCD-jet-correction run control file (see section 4.1). This technique was originally developed by the CDF collaboration [125], and its application within DØ is discussed in great detail in [126]. By balancing the P_T along the direction of the jet this method has the advantage that it minimizes effects due to soft radiation and leakage out of the jet cone. Additional corrections for EM scale (see below), zero suppression, jet cone leakage, and underlying event effects [126] are also included. This factor as a function of jet E_T for two values of η is shown in figure 4.1. These corrections apply to jets of cone $\Delta R = 0.7$ whereas the $e\mu$ analysis uses cones of $\Delta R = 0.5$. However, as noted in section 4.2.3, the cone size of 0.5 was chosen to minimize the probability of jet merging. The energy which is sought, of course, is that of the parton which produced the jet. TOP-LEPTONS corrects a given 0.5 cone jet as follows. A match (in $\eta\phi$) with a 0.7 cone jet is searched for, and if a match is found then the corrected 0.7 cone energy is set as the energy of the jet. If no 0.7 cone

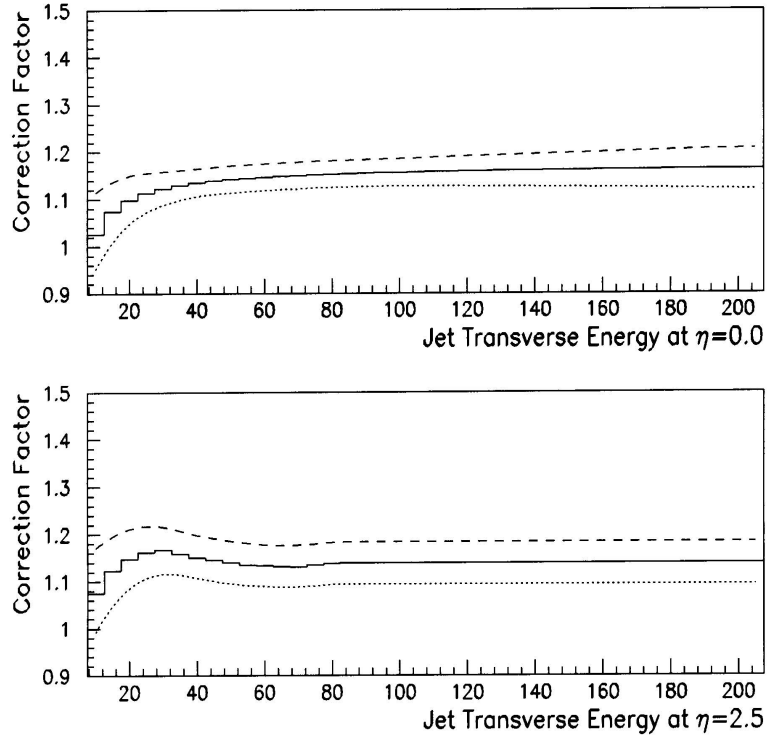


Figure 4.1: DØ jet energy correction factor for 0.7 cone jets at $|\eta| = 0.0$ and $|\eta| = 2.5$

match is found then the standard 0.7 cone response curve is used to scale the 0.5 cone jet.

The correction made to the electromagnetic scale is determined by scaling the reconstructed energy of the EM clusters to make the Z peak in the dielectron mass spectrum agree with the measured LEP value [127]. Detailed studies indicate that the necessary correction is multiplicative (and not additive) in nature. A separate correction for each cryostat has been determined and TOP-LEPTONS applies the appropriate (depending on $\eta^{e/\gamma}$ value) scale

factor to the reconstructed electron and photon energies:

1.072 ± 0.002 , for CC;

1.025 ± 0.005 , for ECN;

1.012 ± 0.007 , for ECS.

As noted above (see section 3.8) the DØRECO corrects the muon P_T determined from the bend angle for the expected energy loss in the calorimeter. This expected energy loss is based on GEANT Monte Carlo studies. For isolated muons, TOP-LEPTONS replaces this expected dE/dx with the actual dE/dx observed in the calorimeter. For non-isolated muons TOP-LEPTONS makes no change and the GEANT dE/dx is used.

When all these corrections are complete TOP-LEPTONS uses the “new” values to recalculate both the calorimeter and muon corrected missing E_T .

4.3.2 Monte Carlo

Monte Carlo jets are also corrected by a multiplicative correction factor. These factors are determined by a scheme which matches RECO jets to the corresponding parton (supplied by the event generator). The difference in energy determines the scale factor. As with the jet corrections for data, these factors also vary with η and jet E_T .

For Monte Carlo data TOP-LEPTONS makes no corrections to EM objects and corrects isolated muons in exactly the same way as it corrects real muons.

Chapter 5

Background vs Signal: What do we expect?

The most important quantity associated with the discovery of any new process is the *observed* ratio (and its error) of signal to background. All processes which can produce signatures similar to that of the “signal” must be investigated. It is always preferable to measure these backgrounds directly from the data, and for high statistics searches (i.e. looking for a resonance) this is what is done. $t\bar{t}$ production and its subsequent decay can be considered as a type of resonance. Although it is not an extremely sharp resonance [51], the principle is the same. The top will show its existence through an “enhancement” in the number of events in some region or regions of phase space. Of course, this excess of events can only be detected if the background is well understood. If the number of observed events is only one or two, then both background and signal must be understood with an uncertainty of much less than one event. A first order approximation to the background is given by the search itself. More precise background estimates must rely on *both* data and Monte Carlo studies (see section 5.1). This stems from the fact that to

fully understand the background it is necessary to understand its components. For very rare signatures these components are of two primary types: (1) very rare physics processes, and (2) tails of more common distributions. Type (1) cannot fully be understood from data studies alone (as is the case with the signal). Type (2) is more approachable from data analysis but far out on the tails it will run out of statistics. The approach taken for the $e\mu$ background analysis is to use a combination of data normalized monte carlo studies and data only studies.

There are many factors which must be considered when estimating the expected number of signal and background events for a given signature. Any given physics event is seen through a “not quite perfect” detector and cross section estimations must include corrections for underlying event, pileup, detector acceptance, detector smearing, trigger bias, and offline inefficiencies (see section 5.1.1 - 5.1.4).

Practical considerations divide the backgrounds to $t\bar{t} \rightarrow e\mu$ into two classes: (1) Those which can be simulated by standard Monte Carlo techniques (see section 5.1.6), and (2), those which at present cannot (see section 5.2).

5.1 Monte Carlo Studies

In the field of High Energy Physics the term “Monte Carlo” is used to refer to any random number based simulation technique. These simulations are of two general types: (1) simulations of beam particle collisions, usually

referred to as physics, and (2) simulations of particles passing through the detector. With the complexity of the physics at 2 TeV (hundreds of particles produced/event) and the sophistication of the apparatus (\$ 100M and 1000 man years) it is necessary to rely heavily on such techniques. However, the output from such complicated sets of programs must be carefully crosschecked if the predictions are to be useful. Bjorken comments on the growing dependence on Monte Carlo data [128]:

“Another change that I find disturbing is the rising tyranny of Carlo. No, I don’t mean that fellow who runs CERN, but the other one, with first name Monte. The simultaneous increase in detector complexity and in computation power has made simulation techniques an essential feature of contemporary experimentation. The Monte Carlo simulation has become the major means of visualization of not only detector performance but also physics phenomena. So far so good. But it often happens that the physics simulations provided by the Monte Carlo generators carry the authority of data itself. They look like data and feel like data, and if one is not careful they are accepted as if they were data. All Monte Carlo codes come with a GIGO (garbage in, garbage out) warning label. But the GIGO warning label is just as easy for a physicist to ignore as that little message on a pack of cigarettes is for a chain smoker to ignore. I see nowadays experimental papers that claim agreement with QCD (translation: someone’s simula-

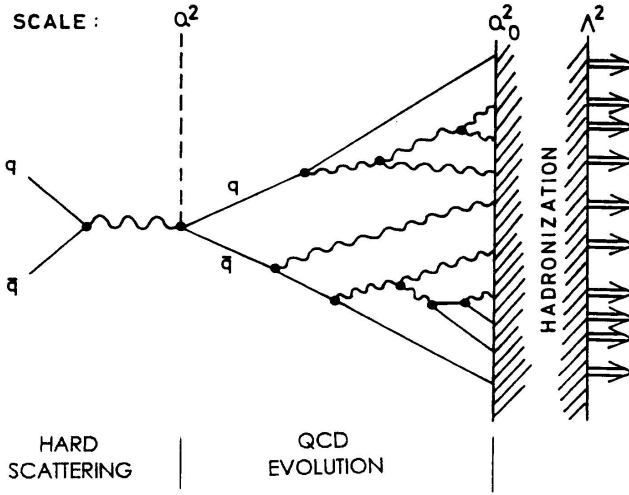


Figure 5.1: Schematic illustration of a $q\bar{q}$ collision

tion labeled QCD) and/or disagreement with an alternative piece of physics (translation: an unrealistic simulation), without much evidence of the inputs into those simulations.”

5.1.1 Event Generators - How to simulate the Physics

Within high energy physics, Monte Carlo techniques are usually attempts at a direct simulation of what happens physically. For a quantity of interest, \bar{f} , (i.e. a cross section) multiple integrations arise from final phase space and other continuous variables (such as momentum fractions of incident partons). The integrand, f , can include not only theoretical cross sections but typically kinematic and geometrical restrictions. Mathematically \bar{f} is an integral of a weight function $f(x_1 \dots x_n)$ over the variables $x_1 \dots x_n$ that parameterize the physics. Monte Carlo methods calculate this integral by generating a random

sample of configurations and averaging the integrand [130].

For hadron-hadron collisions the most commonly used event generators follow the same four basic steps (see figure 5.1) [129]:

1. **Hard Scattering** - Starting with the cross section for simple two body scattering, $\hat{\sigma}_{ij \rightarrow k}$, based on first order (Born) Feynman diagrams, calculate the contribution to the $p\bar{p}$ cross section with the convolution integral

$$\sigma_{ij \rightarrow k} = \int dx_1 \int dx_2 f_i^1(x_1, Q^2) f_j^2(x_2, Q^2) \hat{\sigma}_{ij \rightarrow k}$$

where $x_i = p_i/p$ is the momentum fraction of parton i , Q^2 is the momentum transfer, and $f_i^1(x_k, Q^2)$ and $f_j^2(x_k, Q^2)$ are the structure functions in $p(1)$ and $\bar{p}(2)$ [129]. If the value of Q^2 is assumed to be of the order of the scale of the hard scattering, then there would be no large logarithms in the perturbation expansion, and it is reasonable to truncate the expansion at low order [131].

2. **QCD Evolution** - All partons which participate in the hard scattering are then evolved through repeated parton branchings [131]. The probability \mathcal{P} that a branching $a \rightarrow bc$ will take place during a small change in the evolution parameter dt ($t = \ln(Q^2/\Lambda^2)$) is given by the Altarelli-Parisi equations [132] [133]

$$\frac{d\mathcal{P}}{dt} = \int dz \frac{\alpha_s(Q^2)}{2\pi} P_{a \rightarrow bc}(z)$$

where $P_{a \rightarrow bc}(z)$ are the standard Altarelli-Parisi splitting functions, z is the energy/momentum fraction, and $\alpha_s(Q^2)$ is the strong cou-

pling constant (typically evaluated only to first order). Starting at the maximum allowed mass for parton a , t is successively degraded until a branching occurs. The products , b and c , are then allowed to branch and so on. This branching stops when a parton mass is evolved below some minimum value (i.e. $t < t_{\min} = \ln(Q_{\min}^2/\Lambda^2)$). Of course, allowances must be made for quark masses [134]. This procedure generates both initial and final state radiation.

3. **Hadronization** - Due to the phenomenon of color confinement discussed in chapter 1, the quarks and gluons which emerge from the QCD evolution cannot continue in color singlet states. Virtual quarks and gluons are pulled from the vacuum (always conserving color, charge, etc.) to bind with the original partons and form colorless states. This process is known as fragmentation or hadronization and is not calculable in perturbative QCD. There are several empirical schemes whereby the final state partons are transformed into experimentally observed particles. With the exception of the standard Lund string fragmentation [135] used in PYTHIA, most event generators use the Feynman-Field fragmentation scheme [136]. This approach was designed to reproduce the limited transverse momenta and approximate scaling of energy fraction distributions observed in quark jets. In this scheme the fragmenting quark is combined with an antiquark from a $q\bar{q}$ pair pulled from the vacuum to produce a meson with energy fraction z . The

leftover quark, assumed to have energy fraction $(1 - z)$, is fragmented in the same way. This process continues until the leftover energy falls below some cutoff. Scaling follows from the energy independence of the distribution assumed for z , which is known as the fragmentation function [137]. As discussed in [138], such schemes are conceptually inconsistent. The methods by which restrictions such as energy conservation are dealt with can greatly alter the physics predictions [131].

4. Beam Fragmentation - Among the different generators there is no consensus as to how the leftover beam partons should be evolved and hadronized. PYTHIA uses an extension of the Lund colored string scheme. In ISAJET a minimum bias event is simply superimposed on top of the hard scattering event [131]. The minimum bias event is generated with multi-pomeron chains which gives scaling and long range correlations [129].

While a number of event generators exist, only three (ISAJET, PYTHIA, and HERWIG) have had modified versions created which will output data in a form which is compatible for input to DØGEANT. For the $e\mu$ analysis, all $t\bar{t}$ simulation is done with ISAJET and background samples are produced with ISAJET or PYTHIA (or both).

5.1.2 GEANT - How to simulate the Detector

A simulation of the detector is necessary to understand the acceptance, smearing, and other systematic effects and is also critical in the design of the apparatus. DØ's primary package for detector simulation (and the only one which will be discussed here) is based on version 3.14 of the CERN program GEANT [139]. This program tracks particles through volumes containing user specified materials and correctly performs scattering and interaction processes. These processes include δ -ray production, multiple coulomb scattering, full electromagnetic and hadronic showering, decays, and electron and muon bremsstrahlung [140]. GEANT collects the detector response from all these processes (for all primary and secondary tracks) and converts them to simulated digitized signals.

The most critical step in using GEANT for any detector is the coding of the geometrical model through which GEANT tracks the particles. DØ has removed the complexities of the geometry from the Fortran code (the standard) and placed them in several ASCII geometry files which are read by the program. This avoids having any hard coded constants and permits easier editing and alteration of the geometry [141]. The DØGEANT geometry simulates the muon and tracking chambers in great detail down to the level of sense wires, cathode material, support structures, etc. (preamps, cables, and electronics are not specified in detail). However, the calorimeter must be treated somewhat differently. A full simulation including all the uranium plates and argon gaps spends an inordinate amount of time generating and tracking hundreds

of secondaries through the calorimeter volumes. Therefore, the full structure of the supports and individual modules is present but the calorimeter itself is modelled as homogenous blocks of uranium-G10-argon mixture. This greatly reduces the number of volumes and hence speeds up tracking [141]. However, the sampling fluctuations and attenuation of electromagnetic energy must be put in “by hand” after the showering for each track. Electromagnetic showers are allowed to evolve until the individual secondary particle energies fall below 200 MeV at which point the energies are determined from simple parameterizations.

5.1.3 TRIGSIM - How to simulate the Trigger

Due to the fact that the signal efficiency must be determined from Monte Carlo data (due to the small number of $t\bar{t} \rightarrow e\mu$ events in real data), it is necessary to simulate not only the detector but the trigger as well. DØ has produced two packages, L1SIM and L2SIM, which typically operate as a single entity (TRIGSIM). L1SIM operates on real or Monte Carlo raw data events and uses simulated Level 1 trigger elements and a simulated AND-OR network. As discussed in section 3.7.3, Level 2 is a software trigger and is similar in complexity and task to DØRECO. As such, the simulation (L2SIM) involves only a transfer of code from the compact level 2 language (VAXELN) to standard VMS. To avoid confusion, the simulators use the exact same configuration files as are used for the real data [142].

5.1.4 Further Refinements

In addition to the inefficiencies due to detector and trigger acceptance discussed above, there are a number of steps which must be taken to make Monte Carlo data a more accurate representation of real data.

MU-SMEAR

As discussed in section 3.6, the present resolution of the muon system is parameterized as

$$\left(\frac{\delta P}{P}\right)^2 = (0.18)^2 + (0.010P)^2.$$

DØGEANT, by design, assumes that the muon system operates at the design resolution of

$$\left(\frac{\delta P}{P}\right)^2 = (0.18)^2 + (0.001P)^2.$$

For low momentum ($< \sim 10$ GeV/c) muons this difference is of little consequence. However, for high momentum muons the difference becomes quite significant. For example, for $P^\mu = 50$ GeV/c, the “true” resolution is $\delta P/P = 50\%$ while DØGEANT uses a resolution of $\delta P/P = 19\%$. The differences are due primarily to factors such as alignment uncertainties, drift time resolutions, pad latch inefficiencies and inefficiencies due to gas leaks or voltage problems which are not easily implemented in GEANT. In order to correct for these effects the MU-SMEAR package was created. This package has the purpose of doing further smearing to GEANT data in order to mimic the real detector resolution and to account for the above inefficiencies [143].

Since MU-SMEAR modifies raw data, it must have a raw (Monte Carlo) file input and will output a raw data file, which must then be put through DØRECO (or TRIG-SIM if the effect of MU-SMEAR on the trigger is desired). For each of the 11,386 WAMUS drift tubes MU-SMEAR maintains the following information [143]:

- Fraction of time drift tube ON/OFF
- Pad Latch efficiency (inefficiency drops hits)
- Drift Time signal efficiency
- Drift Resolution in cm
- Δ -Time efficiency
- Δ -Time resolution in cm
- Additional chamber offset in alignment

MU-SMEAR uses this information to smear the resolutions, drop hits, and offset the drift tubes, thus modifying the raw data. It then writes this “new” data in place of the uncorrected raw muon data.

MU-SMEAR has been tuned so that it correctly reproduces the observed width and tails of the $Z_0 \rightarrow \mu\mu$ mass peak. The chamber inefficiency correction is input by applying a global 90% chamber efficiency to the hits created by GEANT. This alone is not sufficient to explain the observed muon momentum resolution. A major improvement is gained by including the chamber mis-alignment term (based on a gaussian smearing of the positions of the

muon modules). This is done by applying shifts which correspond to a gaussian distribution of width x mm to the muon geometry constants file used by DØRECO. From studies of the Z_0 data, the misalignment correction, x , is estimated to be 2-3 mm. This is in good agreement with current estimates of the accuracy to which the module positions are known.

Noisy

Not included in the event generation and detector simulation are effects due to multiple interactions and calorimeter noise. At the typical run 1A luminosities, there are on average 1.2 hard scatterings per beam crossing. Although the probability of obtaining two “interesting” hard scatterings per beam crossing is extremely low, “interesting” events can be accompanied by an “uninteresting” minimum bias event. Also, for real data the calorimeter signal is “polluted” with noise from the uranium and fluctuations in the electronics. Although these effects are not very large DØ has produced a package called NOISY [144] which is designed to incorporate these effects into Monte Carlo data.

This package incorporates multiple interactions by using a second event input stream which can be either real or (fully simulated) Monte Carlo minimum bias data. A weight is determined based on the Poisson probability $P(N, \bar{N})$ for getting N additional interactions per beam crossing. Based on this weight and the wanted \bar{N} , events are then read in from the minimum bias stream and added cell by cell to the current Monte Carlo event.

NOISY gives the user a choice of two methods for the simulation of detec-

tor and uranium noise. The first method models electronic plus uranium noise as a Gaussian of width and average (set by the user) and adds these values to the calorimeter cells. A second data model is based on pedestal distributions from the cosmic ray commissioning run. The ADC counts are then converted to energy and added to the cell noise array.

The output of the NOISY package is a new raw data (or STA) file which must be run through DØRECO. As far as the $e\mu$ analysis is concerned, only very preliminary NOISY studies have been completed. These studies show that the above contributions have no effect on the $t\bar{t} \rightarrow e\mu$ signal and the effect on the backgrounds is expected to be small as well.

5.1.5 Acceptance for $t\bar{t} \rightarrow e\mu$

To estimate the $t\bar{t} \rightarrow e\mu$ acceptance, event samples for ten different top masses ($M_t = 70, 80, 90, 100, 110, 120, 140, 160, 180$, and 200 GeV/c^2) were generated using ISAJET and then put through DØGEANT and DØRECO. Although ISAJET is used as the generator, the input cross sections are those of Laenen *et al.* (as discussed in section 1.3). A systematic error of 10% is assumed on these cross sections. From these data sets, using the final set of cuts described in section 6.3.3, the efficiencies in table 5.1 are obtained where a systematic error due to DØGEANT and DØRECO of 10% is assumed. These numbers include the following corrections and systematic errors:

- MU-SMEAR:

As discussed above Monte Carlo data does not include an accurate representation of the muon chamber inefficiencies and muon smearing/resolution.

These corrections are estimated by applying the MU-SMEAR package (see section 5.1.4) to the GEANT output prior to running DØRECO.

By comparing results with and without the application of MU-SMEAR a correction to Monte Carlo acceptances of

$$91\% \pm 5\%$$

is estimated [145]. This includes both the chamber inefficiency contributions and muon momentum resolution effects. Studies indicate that this efficiency is independent of top mass (within errors).

- **Trigger Efficiencies (TRIGSIM)**

As discussed above, trigger efficiencies are based on TRIGSIM studies.

The three triggers used for collider data are discussed in section 6.2. TRIGSIM studies based on the OR of these three triggers give an efficiency of

$$90\%_{-15\%}^{+10\%}.$$

During the course of run 1A the actual code used in the L1 and L2 filters changed a number of times. To achieve the most accurate simulation of run 1A it is necessary to run versions of TRIGSIM corresponding to each of the different versions of the L1 and L2 code and determine the

efficiency from a luminosity weighted mean. The $e\mu$ analysis has only been able to obtain functioning versions of TRIGSIM for 11.7 pb^{-1} of the total 15.2 pb^{-1} run 1A data. This inadequacy is reflected in an error on the trigger efficiency which is slightly inflated. Within the present errors, this efficiency is independent of top mass (for the range of top masses studied).

- **Electron id efficiencies**

In addition to the inaccurate modeling of muon chamber efficiency and resolution there are also differences between the electron/photon id efficiencies in data and Monte Carlo (i.e. due to tracking inefficiencies etc.). These differences vary with cryostat (CC and EC) and depend on the choice of electron/photon id (i.e. different choices of quality cuts etc.). To incorporate data based efficiencies the procedure is as follows: The Monte Carlo efficiencies are determined without any electron id requirements and then multiplied by the appropriate electron id efficiency determined from the data (CC and EC values weighted by the number of CC and EC events). That is,

$$\varepsilon^e = \frac{N_{CC} \cdot \varepsilon_{CC}^e + N_{EC} \cdot \varepsilon_{EC}^e}{N_{CC} + N_{EC}}$$

where ε^e is the overall electron id efficiency, ε_{CC}^e , N_{CC} , ε_{EC}^e , and N_{EC} are the id efficiencies (from data) and number of Monte Carlo events in the CC and EC respectively. The data efficiencies have been determined from $Z \rightarrow ee$ data for most common electron id definitions [146]. For the CC and EC electron id criteria specified in section 4.2.1 the values

M_t (GeV/c ²)	ε (standard)[%]	M_t (GeV/c ²)	ε (standard)[%]
70	$7.88 \pm 0.05 \pm 1.48$	80	$11.06 \pm 0.03 \pm 2.07$
90	$13.48 \pm 0.03 \pm 2.52$	100	$14.63 \pm 0.04 \pm 2.74$
110	$15.78 \pm 0.03 \pm 2.96$	120	$16.96 \pm 0.04 \pm 3.18$
140	$18.77 \pm 0.06 \pm 3.52$	160	$19.59 \pm 0.05 \pm 3.67$
180	$19.97 \pm 0.05 \pm 3.74$	200	$20.51 \pm 0.05 \pm 3.84$

Table 5.1: Efficiencies for standard $t\bar{t} \rightarrow e\mu$ production (errors: statistical, systematic)

are: $\varepsilon_{CC}^e = 88.9 \pm 1.8\%$ and $\varepsilon_{CC}^e = 94.3 \pm 1.3\%$. This method has the advantage that it is more accurate than using Monte Carlo data only. Additionally, by decoupling the electron id efficiency from the Monte Carlo machinery, the effects of different electron definitions can be seen with a minimum of effort and CPU time.

Tau channel contributions to $e\mu$ production

As discussed in section 1.3, if the “standard” definition of the $e\mu$ channel is expanded to include contributions from $W \rightarrow \tau\nu_\tau$ decays, then the branching ratio is larger by an additional 0.95%. So that the different characteristics between “tau” and “non-tau” $t\bar{t} \rightarrow e\mu$ events can be studied it is necessary to generate these samples separately. Due to limitations in CPU time the tau contributions to the $e\mu$ channel ($t\bar{t} \rightarrow e\tau[\tau \rightarrow \mu], t\bar{t} \rightarrow \mu\tau[\tau \rightarrow e]$, and $t\bar{t} \rightarrow \tau\tau[\tau \rightarrow \mu, \tau \rightarrow e]$) have only been generated for one top mass ($M_t = 140$ GeV/c²). As noted above, the final efficiency for the “standard” channel is

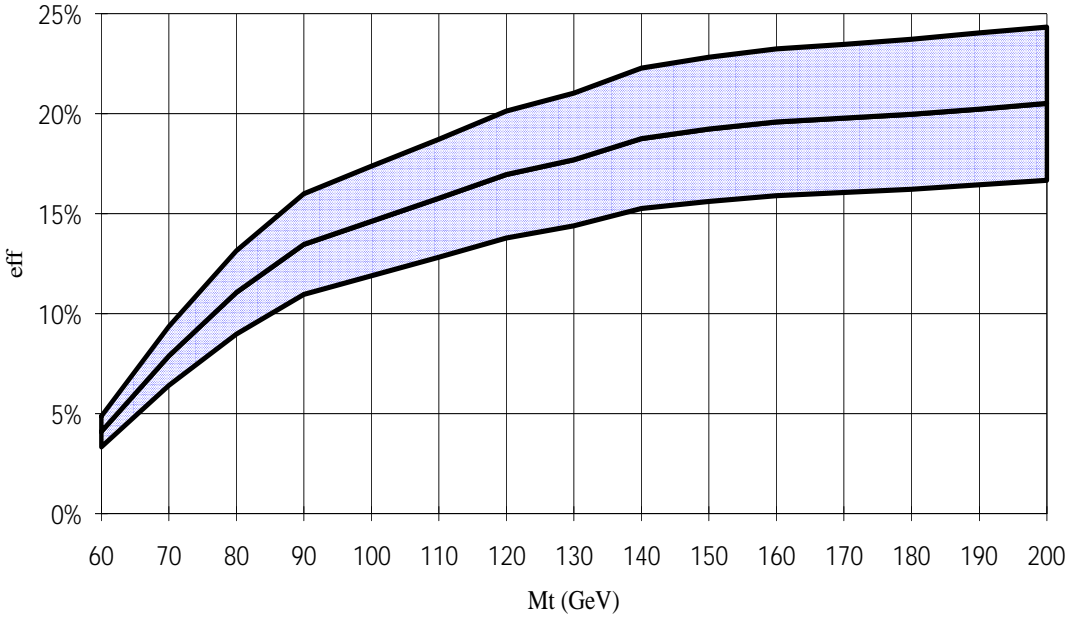


Figure 5.2: Efficiency as a function of M_t for standard contribution to $e\mu$ production (errors are RMS statistical plus systematic)

$18.77 \pm 0.06(\text{stat}) \pm 3.52(\text{sys})$ %. Combining events from both the “standard” and “tau” channels results in an efficiency of

$$15.81 \pm 0.59(\text{stat}) \pm 4.49(\text{sys}) \text{ %}.$$

The lower overall efficiency is indicative of the very low efficiency for the “tau” events and the larger statistical error is due to the fact that very small samples (~ 600 events) were used. Although the overall efficiency is less, the larger starting branching ratio results in a larger predicted number of events. In section 6.5 the number of “standard”, $M_t = 140$ GeV/ c^2 , events expected in run 1A (based on the luminosity defined in section 6.1.1) is $1.19 \pm 0.00(\text{stat}) \pm 0.25(\text{sys}) \pm 0.14(\text{lum})$. Inclusion of the “tau” channels raises this number to

$1.38 \pm 0.01(\text{stat}) \pm 0.25(\text{sys}) \pm 0.14(\text{lum})$. It is expected that the contribution from the “tau” channels will become more significant for larger top masses.

5.1.6 Backgrounds from *real* physics processes (mc)

For the purpose of $e\mu$ background studies, “physics” processes refer to those which can be simulated with standard Monte Carlo techniques. Initial ISAJET level studies guided the way for the full simulation studies which followed [147]. Nine such physics processes have been identified as being capable of producing a signature similar to that of a $t\bar{t} \rightarrow e\mu$ event:

- $QCD \rightarrow e\mu$

Due to the overwhelming cross sections associated with QCD multijet production it is of extreme importance to understand well the probability that such an event can produce an isolated electron or muon. Additionally, the exponentially falling jet P_T spectrum requires that Monte Carlo data samples be generated in P_T bins. That is, since the cross section is so strongly peaked at low P_T , a Monte Carlo sample generated in just one large P_T bin will have all the events clustered near zero. The $e\mu$ analysis generated 26,606 QCD events, each containing (at the ISAJET level) one electron and one muon, both with $P_T > 7 \text{ GeV}/c$ in nine jet P_T bins (10-20, 20-40, 40-60, 60-80, 80-100, 100-130, 130-160, 160-200, and 200-240 Gev/c) and processed them through full DØGEANT and DØRECO (a non-trivial task!). These events were generated in such a way that direct $b\bar{b}$ and $c\bar{c}$ and gluon bremsstrahlung to $b\bar{b}$ and $c\bar{c}$ were

included. These events contain only “prompt” electrons and muons, meaning only those from b and c decays. As such, isolation is the single most important factor in reducing this background. Since isolation is significantly influenced by the detector itself, reliable isolation studies cannot be performed at generator level.

- $Z \rightarrow \tau\tau \rightarrow e\mu$

The $e\mu$ analysis has generated three large (each in excess of 2000 events) samples (two ISAJET, one PYTHIA) of $Z \rightarrow \tau\tau \rightarrow e\mu$ and processed them through full DØGEANT and DØRECO. The last two samples required, at the generator level, that the electron and muon both have $P_T > 7$ GeV/c.

- $Z \rightarrow b\bar{b} \rightarrow e\mu$

Two large samples of $Z \rightarrow b\bar{b} \rightarrow e\mu$ were generated and processed through full DØGEANT and DØRECO. As with the QCD samples, one electron and one muon, both with $P_T > 5$ GeV/c were required at the generator level.

- $Z \rightarrow c\bar{c} \rightarrow e\mu$

ISAJET only studies indicate that the background contribution from $Z \rightarrow c\bar{c} \rightarrow e\mu$ events is minimal. Furthermore, since the leptons from c decay are of lower P_T than those from b decay, the contribution from $Z \rightarrow c\bar{c} \rightarrow e\mu$ will be less than that from $Z \rightarrow b\bar{b} \rightarrow e\mu$.

- $W^+W^- \rightarrow e\mu$

	Integrated cross section (pb)		events in 15.2 pb^{-1}
	No Cuts	Final Cuts	
$QCD \rightarrow e\mu$	28.4×10^6	$(0.0 \pm 2.0) \times 10^{-3}$	$(0.0 \pm 3.0 \pm 0.2) \times 10^{-2}$
$Z \rightarrow \tau\tau \rightarrow e\mu$	13.2	$(2.4 \pm 0.5) \times 10^{-2}$	$0.36 \pm 0.08 \pm 0.04$
$Z \rightarrow b\bar{b} \rightarrow e\mu$	53.9	$(0.0 \pm 1.4) \times 10^{-4}$	$(0.0 \pm 2.2 \pm 1.4) \times 10^{-3}$
$Z \rightarrow c\bar{c} \rightarrow e\mu$	10.9	$(0.0 \pm 7.1) \times 10^{-6}$	$(0.0 \pm 1.1 \pm 0.7) \times 10^{-5}$
$W^+W^- \rightarrow e\mu$	0.25	$(1.4 \pm 0.3) \times 10^{-2}$	$0.21 \pm 0.05 \pm 0.03$
DY $\rightarrow \tau\tau \rightarrow e\mu$	18.9	$(1.7 \pm 0.3) \times 10^{-4}$	$(2.6 \pm 0.5 \pm 0.3) \times 10^{-3}$
$WZ \rightarrow e\mu$	0.018	$(1.8 \pm 0.4) \times 10^{-3}$	$(2.7 \pm 0.6 \pm 0.3) \times 10^{-2}$
$W\gamma \rightarrow e\mu$	NA	$(4.5 \pm 0.9) \times 10^{-8}$	$(6.8 \pm 1.4 \pm 0.9) \times 10^{-7}$
$W + \text{jets} \rightarrow e\mu$	NA	$(0 \pm 1.4) \times 10^{-3}$	$(0.0 \pm 2.1 \pm 1.3) \times 10^{-2}$
Total:		$(3.9 \pm 0.6) \times 10^{-2}$	$0.60 \pm 0.09 \pm 0.05$

Table 5.2: $e\mu$ Physics backgrounds (errors on cross section are systematic; errors on number of events are systematic and luminosity)

Due to the great similarity with $t\bar{t} \rightarrow e\mu$ events, W pair production (with dileptonic decay) is the most difficult to background to distinguish from top. Three large samples (one ISAJET and two PYTHIA) were generated and processed through full DØGEANT and DØRECO. As with the other full simulation samples, lepton P_T cuts were made at the generator level. However, due to the high P_T of leptons from W decay, this requirement provided essentially no reduction (as is the case for $t\bar{t} \rightarrow e\mu$ events as well).

- DY: $\gamma^* \rightarrow \tau\tau \rightarrow e\mu$

ISAJET studies indicate that Drell-Yan dilepton production is not a serious background. The likelihood of obtaining one high P_T electron,

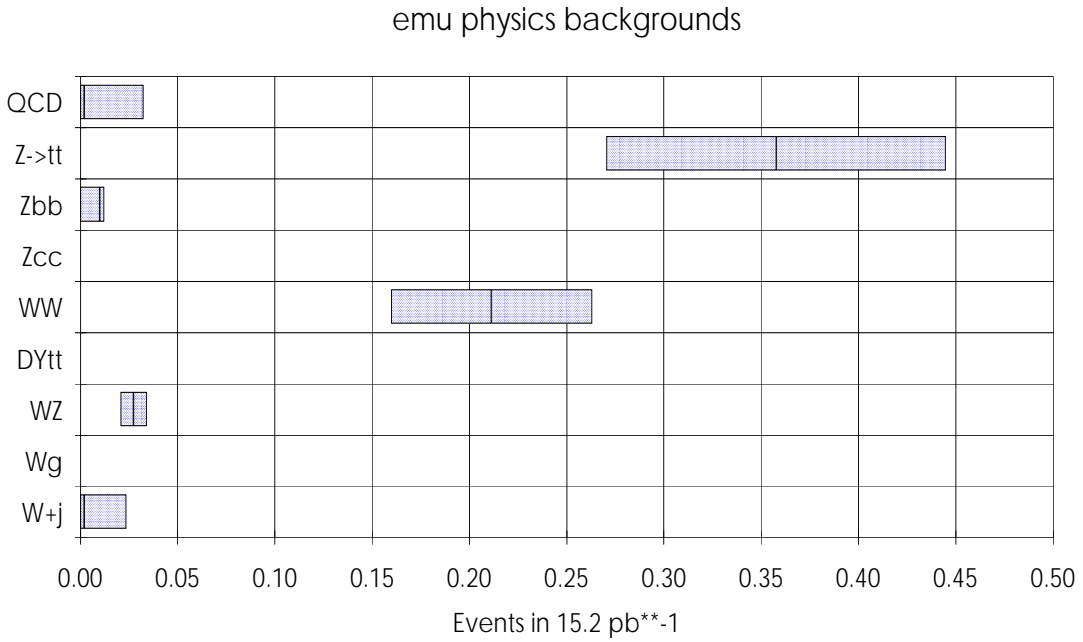


Figure 5.3: $e\mu$ Physics background events in 15.2 pb^{-1}

one high P_T muon, a large missing E_T , and one or more jets from a Drell-Yan $\rightarrow \tau\tau$ is vanishingly small.

- $WZ \rightarrow e\mu$

With a cross section ~ 10 times less than that for W pair production, $WZ \rightarrow e\mu$ events are not considered to be serious background for low mass top. However, due to the uncertainty in the theoretical cross sections for WW and WZ productions, and since both CDF and DØ have several WZ candidates, this background must be treated with care. To that end, two large samples (one ISAJET and one PYTHIA) were generated and processed through full DØGEANT and DØRECO. As usual, lepton P_T cuts were made at the generator level. However, due to the

high P_T of leptons from W and Z decay, this requirement provided no reduction.

- $W + \text{jets} \rightarrow e\mu$

Due to the fact that jets produced in association with W 's are primarily gluon jets, the probability of obtaining a $W + \text{jets} \rightarrow e\mu$ event where both leptons are prompt and isolated is very small. This conclusion is supported by a study done with $\sim 19,000$ $W + \text{jets}$ events which were put through the DØ Showerlibrary (a fast lookup table version of DØGEANT). It should be noted that this background is the primary background to the lepton + jets decay channels of $t\bar{t}$.

- $W\gamma \rightarrow e\mu$

Studies done with ISAJET, PYTHIA, and the Baur & Zepenfeld Monte Carlo (designed specifically for generating $W\gamma$ events) indicate that background from $W\gamma \rightarrow e\mu$ is negligible [148].

In an attempt to avoid some of the biases inherent in Monte Carlo studies all input cross sections are based on published values as opposed to those produced by the generator. As noted above, all samples which were sent through DØGEANT had lepton P_T cuts applied at the generator level. This was done to avoid wasting valuable CPU time by pushing uninteresting events through DØGEANT that later would certainly fail the selection criteria. Given in table 5.2 are the background cross sections and the number of events expected in $15.2 \pm 1.8 \text{ pb}^{-1}$ (Integrated luminosity for run 1A, see section 6.1.1). Due

to the large numbers of events in the Monte Carlo background samples, the statistical errors are negligible. The errors on the cross sections are systematic and the errors on the number of events are systematic and that due to luminosity uncertainty. The expected numbers of events for each type of background are also shown in figure 5.3. To appreciate the degree of rejection provided by the selection procedure discussed in chapter 6, the “no-cuts” cross sections for these backgrounds are given in the first column of table 5.2. These values are based on the numbers determined in Appendix A. Finally, the same correction factors and errors discussed for the $t\bar{t} \rightarrow e\mu$ acceptance in section 5.1.5 are assumed for the background calculations.

5.2 Instrumental Backgrounds (fakes)

Often physics and detector effects conspire to “fake” a prompt, isolated electron or muon. Such processes, frequently not fully understood during the detector design phase, are difficult to simulate accurately (being due to the tails of distributions) and must therefore be understood primarily from data studies. The next section discusses six sources of “fake” electrons and muons. The following sections describe how these “fake” electrons and muons conspire with “real” physics processes to contribute substantially to the $e\mu$ background.

5.2.1 Sources

- Jets which fake electrons/photons

For the D \emptyset detector the dominant “fake contributor” is that of jets which are misidentified as electrons or photons. Detailed studies of the probability that fluctuations in jet fragmentation fake an electron or photon have been completed [153]. These studies involve searches for isolated electrons and photons in unbiased QCD data. Of course, any such study is complicated by the different electron id definitions. The $e\mu$ analysis modified its final electron id criteria on the basis of these studies. These studies have been performed on monte carlo data with similar results [154]. As shown in figure 5.4, a value of 0.6×10^{-3} is used as the probability for a jet to fake an electron (as defined for the $e\mu$ analysis). [155].

- **Tau’s which fake electrons/photons**

Due to the narrowness of the produced jets, some fraction of hadronic tau decays will be misidentified as electrons or photons. Because of the difficulty in identifying taus, it is very difficult to determine the rate at which tau’s fake electrons from real data. Therefore 10,000 $Z \rightarrow \tau\tau \rightarrow$ anything events were generated with ISAJET and run through the Showerlibrary. A comparison of the number of muons and electrons/photons found was used to determine the rate at which tau’s fake electrons/photons in the D \emptyset detector. There was no $\pi/K \rightarrow \mu$ in Showerlibrary at the time this study was done. As shown in figure 5.4 a value of 0.01 is found as the probability for a tau to fake an electron (as defined for the $e\mu$ analysis).

- **Muons which produce bremsstrahlung**

As discussed in section 6.3.3, the majority of muon bremsstrahlung photons are produced very close (in $\eta\phi$) to the muon. As such, the photon will be matched to the track left by the muon in the central detector and may be misidentified as an electron. Monte carlo studies [156] indicate that the number of such fake electrons surviving the $\Delta R(e, \mu)$ cuts discussed in section 6.3.3 are negligible. As shown in figure 5.4 a value of 2.0×10^{-3} is used as the probability that a muon will produce a brem which will pass the electron criteria for the $e\mu$ analysis [148].

- $\pi/K \rightarrow \mu$

Although π/K decays to muons cannot truly be classified as “fakes”, due to the long decay length ($c\tau \sim 4 - 8$ m) they are certainly not prompt. DØ’s compactness (short distance from interaction vertex to calorimeter) is a major factor in minimizing this background. Two factors dominate the determination of the rate of high P_T muons from such decays: (1) The probability that a jet will give a detectable muon from π/K decay [149], and (2) the muon P_T spectrum [150]. For the high P_T leptons required by the $e\mu$ analysis, this is not a significant contribution to the background. As shown in figure 5.4 a value of 3.1×10^{-3} is used as the probability to get a detectable $\pi/K \rightarrow \mu$ [149] from QCD events and 4.0×10^{-4} is the additional rejection factor if the muon is required to have $P_T > 15$ GeV/c [150].

- **Punchthrough**

Due to the large number of radiation lengths in the DØ calorimeter and muon toroids, punchthrough which “fakes” a muon is very small. Nevertheless two studies have been done. The first study [151] is based on plate level (which is very CPU intensive) DØGEANT studies of punchthrough through the calorimeter with the muon system included. The results are that there is some probability of punchthrough to the muon A-layer but very little chance for a particle to penetrate the iron and get into the B and C-layers. In scanning, some events have been seen which punched through to the A-layer but it is difficult to distinguish a punchthrough to the B/C layers from a standard “ μ in jet” event. A second study [152], based on real data and other experiments, has results which are similar to the monte carlo study. Both studies indicate a higher punchthrough rate in the region between the toroids. However, as discussed in section 4.2.2, this region is excluded for the $e\mu$ analysis.

- **Cosmic Ray Muons**

As discussed in section 4.2.2, initial scanning studies led to the cosmic ray rejection code built into the TOP-LEPTONS package. These cuts were designed to reject all but the most pathological cosmics, which fortunately occur at a negligible rate. Since the $e\mu$ analysis also requires a good electron, the final event sample (see section 6.3.2) is expected to contain no cosmics.

5.2.2 Channels

The sources of fake electrons, $X(e)$, and fake muons, $Y(\mu)$, discussed above conspire with a number of physics processes to produce backgrounds to the $e\mu$ channel. Nine such contributions have been studied:

- $\text{QCD} \rightarrow \mu + X(e)$ - primarily standard $b\bar{b} \rightarrow \mu$ production accompanied by a fake electron coming from a jet.
- $\text{QCD} \rightarrow e + Y(\mu)$ - primarily standard $b\bar{b} \rightarrow e$ production accompanied by a muon coming from π/K decay in a jet.
- $\text{QCD} \rightarrow X(e) + Y(\mu)$ - multijet production where one of the jets is misidentified as an electron and another produces a muon through π/K decay.
- $Z + \text{jets} \rightarrow \tau\tau + \text{jets} \rightarrow \mu + \tau(e) + \text{jets}$ - where one τ decays to a μ ($\tau \rightarrow \mu\bar{\nu}_\mu\nu_\tau$) and the $\tau(e)$ is primarily a hadronic tau decay which is misidentified as an electron.
- $W + \text{jets} \rightarrow \mu + \text{jets}$ (brem) - where the muon has a bremsstrahlung photon which has an accidental track match with an unrelated track.
- $W + \text{jets} \rightarrow e + \text{jets} + Y(\mu)$ - where the muon is from π/K decay in a jet.
- $W + \text{jets} \rightarrow \mu + \text{jets} + X(e)$ - where one of the jets fakes an electron.
- $Z + \text{jets} \rightarrow \mu\mu + \text{jets} + X(e)$ - where one of the muons is lost and one of the jets fakes an electron.

- $Z + \text{jets} \rightarrow ee + \text{jets} + Y(\mu)$ - where one of the electrons is lost and the muon comes from π/K decay in a jet.

5.2.3 The “fakes” spreadsheet

The channels discussed in the previous section have been attacked in a number of ways. However, in order to maintain a close relationship with the critical (and changing) quantities which are determined from data studies (fake electron rate, etc) and to develop the ability to easily determine the fake background for any given choice of cuts, a “spreadsheet” method was adopted. This “fakes” spreadsheet has as input a number of quantities which are taken from data (both DØ and elsewhere) and uses these quantities to compute the cross section and expected number of events for each of the above channels. As shown in figure 5.4, a typical example ($\text{QCD} \rightarrow \mu + X(e)$) proceeds as follows: The cross section for $\text{QCD} \rightarrow \mu + X$ (6114 pb) is obtained from the b group. Since these are by nature 2 jet events, the requirement that there will be one fake electron and one jet means that the input cross section should be that for events with 3 or more jets. Therefore the cross section is scaled down by the ratio between 3 jet events and 2 jet events. Since the muon must be isolated, the cross section is further reduced by the isolation rejection factor (determined from looking at the fraction (0.08 [158]) of $b\bar{b} \rightarrow \mu + X$ events which survive the $e\mu$ isolation requirement. Since a fake electron is required the cross section must be further reduced by the fraction (1.5×10^{-3}) of (fake) electrons found in multijet data. To account for the missing E_T requirement

Int Lum +- syserr(pb**-1):	15.2	1.8		11/28/93	11:45			
			stat err	sys err	W+j -> e+j	crsec (pb)	stat err	sys err
Probability that a jet fakes an electron:	6.0E-4	3.0E-5	6.0E-5		W+0 jets	1956.00	7.27	391
Probability that a jet gives pi/K->mu:	3.1E-3	0	3.1E-3		W+1 jet	566.80	3.33	113
Isolation cut on mu:	0.08	0	0.04		W+2 jets	168.60	1.33	67.44
Pt cut on mu from pi/K:	4.0E-4	0	2.0E-4		W+3 jets	45.44	0.63	27.26
Branching Ratio for tau -> mu:	0.1758	0	0.0027		W+4 jets	11.50	0.25	9.20
Probability that RECO picks up tau as e:	0.01	0	0			2748.34	8.14	413.84
Probability that a mu brems:	0.002	0	0					
Crsec Ratio: QCD (n jet)/(2 jet)	0.15	0	0		W+nj -> e+nj (n>=1)	792.34	3.65	135.01
Missing Et cut (QCD):	7.0E-3	0	7.0E-4		W+nj -> e+nj (n>=2)	225.54	1.49	73.32
Missing Et cut (Z+jets):	0.2	0	0.02		W+nj -> e+nj (n>=3)	56.94	0.67	28.77
Detector Efficiency:	0.3	0	0.045					
Trigger Efficiency:	0.90	0	0.135		Z+nj -> ee+nj (n>=1)	74.40	0.34	12.68
					Z+nj -> ee+nj (n>=2)	21.18	0.14	6.88
					Z+nj -> ee+nj (n>=3)	5.35	0.06	2.70
					QCD -> mu+X	crsec (pb)	stat err	sys err
					Pt(mu) > 15 GeV	6114.0	0	1834.2
					QCD->njets (n>=2)	4.0E+7	0	2.0E+7
					QCD->njets (n>=3)	1.5E+7	0	7.5E+6
					QCD->njets (n>=4)	6.0E+6	0	3.0E+6
QCD->mu+X(e)								
			crsec (pb)	stat err (pb)	sys err (pb)	N evts in IntLum:	stat err	sys err
Crsec: QCD -> mu +X:	6114.0	0	1834.2		92932.8	0.0E+0	2.8E+4	1.1E+4
Scaledown by (3 jet)/(2 jet) ratio:	917.1	0.0	275.1		13939.9	0.0E+0	4.2E+3	1.7E+3
Isolation cut on mu:	73.4	0.0	42.8		1115.2	0.0	650.3	133.8
Require fake e:	0.04	0.0E+0	2.6E-2		0.67	0.00	0.4	0.08
Missing Et cut:	3.1E-4	0.0E+0	1.8E-4		4.7E-3	0.0E+0	2.8E-3	5.6E-4
Detector Efficiency:	9.2E-5	0.0E+0	5.7E-5		1.4E-3	0.0E+0	8.7E-4	1.7E-4
Trigger Efficiency:	8.3E-5	0.0E+0	5.3E-5		1.3E-3	0.0E+0	8.0E-4	1.5E-4
								quad tot 8.2E-4
QCD->e+Y(mu)								
			crsec (pb)	stat err (pb)	sys err (pb)	N evts in IntLum:	stat err	sys err
Crsec: QCD -> e +Y:	6114.0	0	1834.2		92932.8	0.0E+0	2.8E+4	1.1E+4
Scaledown by (4 jet)/(2 jet) ratio:	917.1	0.00	275.13		13939.9	0.0E+0	4.2E+3	1.7E+3
Crsec: Z+jets -> ee + njets (n>=3):	5.346	0.063	2.702		81.27	0.96	41.07	9.75
Require jet to pi/K->mu:	0.017	2.0E-4	1.9E-2		0.254	3.0E-3	2.8E-1	3.0E-2
Isolation cut on mu from pi/K:	1.3E-3	1.6E-5	1.6E-3		0.020	2.4E-4	2.5E-2	2.4E-3
Pt cut on mu from pi/K:	5.3E-7	6.3E-9	7.0E-7		8.1E-6	9.6E-8	1.1E-5	9.7E-7
Missing Et cut:	1.1E-7	1.3E-9	1.4E-7		1.6E-6	1.9E-8	2.1E-6	1.9E-7
Detector Efficiency:	3.2E-8	3.8E-10	4.3E-8		4.9E-7	5.7E-9	6.5E-7	5.8E-8
Trigger Efficiency:	2.9E-8	3.4E-10	3.9E-8		4.4E-7	5.2E-9	5.9E-7	5.2E-8
						stat err	sys err	Lum err
Total	Fake	Evts:			0.39	0.02	0.20	0.04

Figure 5.4: Partial view of the Fake's Spreadsheet

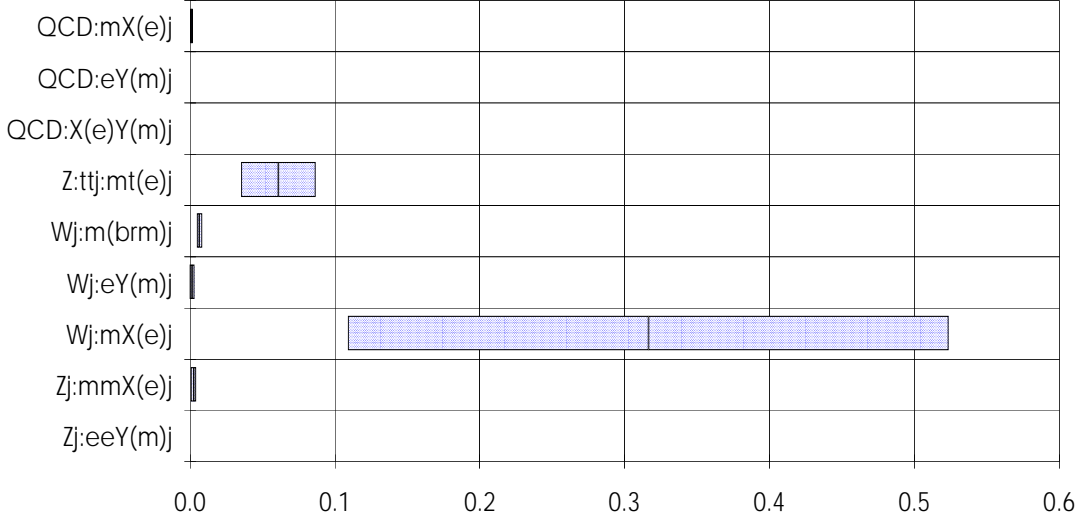


Figure 5.5: $e\mu$ fake background events in 15.2 pb^{-1}

an additional rejection factor obtained by studying the missing E_T content of multijet events (7.0×10^{-3} [159]). Finally, additional rejection factors are applied to account for detector and trigger efficiencies.

This “fakes” spreadsheet is actually only one of a set of 7 spreadsheets which are linked directly and through a macro and allow for a reliable and flexible study of the $t\bar{t} \rightarrow e\mu$ acceptances and backgrounds. The mechanics of these sheets are discussed in detail in [157]. Several of these channels have been approached with other “hand” calculations and Monte Carlo studies which give consistent results. The breakdown of the fake backgrounds is shown in table 5.3 and figure 5.5. Due to the nature of the calculations, the statistical errors are negligible. The errors on cross section are systematic and the errors on the number of events are systematic and that due to luminosity uncertainty.

	σ (pb)	events in 15.2 pb^{-1}
	Final Cuts	
$QCD \rightarrow \mu + X(e)$	$(8.3 \pm 5.3) \times 10^{-5}$	$(1.3 \pm 0.8 \pm 0.2) \times 10^{-3}$
$QCD \rightarrow e + Y(\mu)$	$(1.4 \pm 1.9) \times 10^{-8}$	$(2.1 \pm 2.9 \pm 0.3) \times 10^{-7}$
$QCD \rightarrow X(e) + Y(\mu)$	$(5.7 \pm 8.0) \times 10^{-7}$	$(8.6 \pm 12.0 \pm 1.0) \times 10^{-6}$
$Z \rightarrow \tau\tau \rightarrow e\mu$	$(4.0 \pm 1.6) \times 10^{-3}$	$(6.1 \pm 2.5 \pm 0.7) \times 10^{-2}$
$W + \text{jets} \rightarrow \mu + \text{jets}$ (brem)	$(4.5 \pm 1.0) \times 10^{-4}$	$(6.8 \pm 1.4 \pm 0.8) \times 10^{-3}$
$W + \text{jets} \rightarrow e + \text{jets} + Y(\mu)$	$(7.6 \pm 11.0) \times 10^{-5}$	$(1.2 \pm 1.6 \pm 0.1) \times 10^{-3}$
$W + \text{jets} \rightarrow \mu + \text{jets} + X(e)$	$(2.1 \pm 1.3) \times 10^{-2}$	$0.32 \pm 0.20 \pm 0.04$
$Z + \text{jets} \rightarrow \mu\mu + \text{jets} + Y(\mu)$	$(1.7 \pm 1.0) \times 10^{-4}$	$(2.6 \pm 1.5 \pm 0.3) \times 10^{-3}$
$Z + \text{jets} \rightarrow ee + \text{jets} + Y(\mu)$	$(2.9 \pm 3.9) \times 10^{-8}$	$(4.4 \pm 5.9 \pm 0.5) \times 10^{-7}$
Total:	$(2.6 \pm 1.5) \times 10^{-2}$	$0.39 \pm 0.20 \pm 0.04$

Table 5.3: $e\mu$ fake backgrounds ($X(e)$ and $Y(\mu)$) are fake electrons and fake muons respectively, $\tau(e)$ is a tau which fakes an electron (errors on cross section are systematic; errors on number of events are systematic and luminosity)

5.3 Summary

The results of the background studies in sections 5.1.6 to 5.2 give the expected number of events in run 1A:

- Physics Backgrounds:

$$0.60 \pm 0.02(\text{stat}) \pm 0.09(\text{sys}) \pm 0.05(\text{lum}) \text{ events}$$

- Fake Backgrounds:

$$0.39 \pm 0.02(\text{stat}) \pm 0.20(\text{sys}) \pm 0.04(\text{lum}) \text{ events}$$

- Total Background:

$$0.99 \pm 0.03(\text{stat}) \pm 0.22(\text{sys}) \pm 0.06(\text{lum}) \text{ events}$$

The primary physics backgrounds are $Z \rightarrow \tau\tau \rightarrow e\mu$ and $W^+W^- \rightarrow e\mu$ and the primary fakes background is $W + \text{jets} \rightarrow \mu + \text{jets} + X(e)$.

Chapter 6

Analysis of Collider data

This chapter summarizes the analysis of the collider data for run 1A. First, the data sample is defined and its corresponding integrated luminosity is determined. This is of utmost importance since this result is combined with the cross sections from chapter 4 to obtain the expected number of signal and background events. Second, the data selection process is reviewed (including a discussion of the trigger). Finally, the results are presented and used to determine an upper limit cross section curve. This result is then combined with a theoretical prediction for the $t\bar{t}$ cross section to obtain a lower limit on the mass of the top quark.

6.1 Data Sample

In the initial stage of event selection no restriction is made on either level 1 or level 2 triggers. The selection depends only on RECO objects. This is done to achieve the maximum possible sensitivity for “possible” top candidates.

6.1.1 Integrated Luminosity

The $e\mu$ search includes the full Run 1A luminosity from (Runs 50733 to 65879 inclusive) with the exclusion of runs which have been classified as having unrecoverable problems. Data from these “bad” runs is explicitly removed (see section 4.1) from the analysis during the STA selection process (see section 6.3.2). Typical reasons for inclusion in the bad run list are :

- corrupted trigger framework (level 1)
- no muon toroid field
- incorrect muon toroid field
- severe calorimeter readout problems (data from full octant lost/corrupted)
- tracking chamber and/or muon high voltage off
- proton only store
- runs logged by shift captain as bad
- special runs

For the full Run 1A sample this gives a total of 139 bad runs.

DØ data is stored in files (known as partitions) which are of a convenient size. A full run will typically produce 5-10 of these partitions. The $e\mu$ analysis analyzed 4101 unique express line partitions for Run 1A. An initial determination of the total integrated luminosity is obtained by summing the luminosity

corresponding to each of these 4101 partitions. After correction for multiple interactions ¹ this gives an total integrated luminosity of :

$$\text{Total Run 1A Integrated Luminosity} = 16.4 \text{ pb}^{-1}$$

Summing over the runs included in the bad run list gives a correction of :

$$\text{Bad Run Integrated Luminosity Correction} = 0.209 \text{ pb}^{-1}$$

This gives a net Integrated Luminosity of :

$$\text{Integrated Luminosity} = 16.2 \text{ pb}^{-1}$$

During the first 1.5 seconds of the main ring cycle (injection and transition), losses from the main ring result in many of the muon chambers seeing a large flux of unwanted particles (making data from these chambers very difficult to use). All of the analyses involving muons eliminate events taken during this period. The $e\mu$ analysis removes these events during the STA selection process (cutting on a bit set by the level 1 trigger framework). However, the luminosity must be corrected to reflect this change in the data sample. Fortunately, muon triggers typically are set to veto (not fire) during this period. Clearly, the integrated luminosity for a “blanked” trigger will be less than that of a “non-blanked” trigger by a factor which is equivalent to the correction needed above. The “blanked” and “non-blanked” triggers which were chosen were

¹multiple interactions is the condition where more than one hard scattering occurs during a bunch crossing. The rate of multiple interactions is itself a luminosity dependent quantity [160].

MU-ELE and ELE-JET-MAX respectively. These are two triggers used for the $e\mu$ analysis and are discussed in detail in section 6.2. The correction factor by this procedure is:

$$\frac{\text{Integrated Luminosity for MU - ELE}}{\text{Integrated Luminosity for ELE - JET - MAX}} = 0.940.$$

Therefore, the final corrected luminosity is:

$$\text{Integrated Luminosity} = 15.2 \pm 1.8 \text{ pb}^{-1},$$

where the standard DØ luminosity error of $\pm 12\%$ is assumed.

6.2 Triggers

To enable an accurate simulation (see section 5.1.3) of the trigger acceptance, the analysis is restricted to a logical OR of three express line level 2 filters (requiring also, of course, the corresponding level 1 trigger bits): “mu-ele”, “ele-jet-max” and “mu-jet” (see table 6.1). The analysis is restricted to these filters because they are the only appropriate non-preserved filters which get written to the express line. Studies using the trigger simulator and data show that the loss in acceptance by making this restriction is negligible (as compared to using all triggers).

6.3 Data Selection

The data selection/analysis proceeds through three stages :

Trigger	Level 1	Level 2
$e\mu$	≥ 1 EM tower, $E_T > 7$ GeV $\geq 1\mu$, $ \eta < 1.7$	≥ 1 EM cluster, $E_T > 7$ GeV $\geq 1\mu$, $P_T > 5$ GeV/c
$\mu + \text{jet}$	$\geq 1\mu$, $ \eta < 1.7$	Runs 50226 to 57711
	≥ 1 (HAD+EM) tower, $E_T > 5$ GeV	$\geq 1\mu$, $P_T > 5$ GeV/c $\not{E}_T > 12$ GeV ≥ 2 jets, $E_T > 15$ GeV ≥ 1 jet, $E_T > 25$ GeV (jet cone = 0.3)
		Runs 57712 to 65879
		$\geq 1\mu$, $P_T > 14$ GeV/c ≥ 1 jet, $E_T > 15$ GeV (jet cone = 0.7)
$e + \text{jet}$	≥ 1 EM tower, $E_T > 12$ GeV ≥ 2 (HAD+EM) towers, $E_T > 5$ GeV	≥ 1 EM cluster, $E_T > 12$ GeV ≥ 2 jets, $E_T > 16$ GeV $\not{E}_T > 20$ GeV

Table 6.1: $e\mu$ triggers (level 1 and level 2) for run 1A

- Loose express line DST filtering
- STA selection/filtering
- Final Data analysis cuts

6.3.1 Initial DST selection

During the run 1A data collection period (August 1992 - May 1993) there was typically a two day travel time for the expressline data to get from the detector, through DØRECO, and into the reserved DST storage area (a series of hard disks known as DØ\$DATA\$DST). Once every day or two the new

data was run through a filter which wrote out selected DST files to local disk. This filtering was done using the TOP-LEPTONS package with the following selection criteria:

Runrange : 50k – 56k

$P_T^\mu > 5 \text{ GeV}/c + \mu$ id cuts (standard CLEANMU except $\int B \cdot dl$ cut)

$E_T^{e/\gamma} > 5 \text{ GeV} + e$ id cuts (standard CLEANEM)

Runrange : 56k – 66k

$P_T^\mu > 10 \text{ GeV}/c + \mu$ id cuts (standard CLEANMU except $\int B \cdot dl$ cut)

$E_T^{e/\gamma} > 10 \text{ GeV} + e$ id cuts (standard CLEANEM)

These id cuts are discussed in detail in section 4.2. Note that at this stage no distinction is made between electrons and photons. The threshold change at run 56,000 was necessary to keep the volume of event processing manageable and at the same time still retain full acceptance. Note that the cuts at this stage are substantially less restrictive than those applied for the final selection (see section 6.3.3). This is to enable background studies of mis-identified/fake muons/electrons/photons.

This initial filtering resulted in 1388 events for run 1A.

6.3.2 STA selection

For each event selected by the above DST filter, a single STA file was fetched from the DØ data tape system (as noted in section 3.8, STA's are so large that it is difficult to keep many on disk) and copied to local disk. These files(events) were then put through a more restrictive TOP-LEPTONS filter

which added the following cuts:

- Bad Run rejection
- Software Microblank Veto
- Back-to-back mip trace in calorimetry

The effects of the software microblank veto and cosmic ray rejection were verified by hand scanning to ensure the accuracy of the software rejection/tagging algorithms. In cases for which the STA tapes were corrupted the raw data corresponding to the selected DST events were selected and the STA's regenerated by running DØRECO. All of these events were meticulously hand scanned and the observations/results were recorded. The recorded information includes: run/event number, TOP-LEPTONS selection flags, a scan code, and a brief comment about the event. While the scanning was not used to reject events, it proved to be an invaluable tool to improve the selection criteria in that it gave a very physical view of the behavior of the detector (i.e. isolation, shower shape, etc.).

A total of 713 events survive after this selection and are preserved for further analysis. The STA files corresponding to these events are run through each new version of DØRECO and the resulting DST and STA files are kept on local disk for easy access. These files are the basis of the final data selection sample.

6.3.3 Cuts/Motivation

The final selection cuts are applied to the above 713 event $e\mu$ candidate sample (based on version 11.17 of DØRECO). These cuts are applied on fully corrected quantities which include (see section 4.3.1):

- Muon dE/dx for isolated muon tracks taken from the observed calorimeter mip deposition. For non-isolated tracks the DØRECO default Geant expected correction is retained.
- Jets corrected for calorimeter response, energy scale, underlying event and minimum bias pileup.
- Electrons/Photons corrected for energy scale.
- \cancel{E}_T corrected for Energy scale effects from electrons, photons, jets and muon corrections.

It is at this stage that the requirement that each event satisfy at least one of the MU-ELE, MU-JET-MAX, or ELE-JET-MAX filters is imposed. Note also, that until this stage no distinction was made between electrons and photons. From this stage onwards the analysis requires only electrons (as defined in section 4.2.1). The event yield as a function of selection cut is summarized in table 6.2. Scatter plots for the first six cuts for data and $t\bar{t} \rightarrow e\mu$ Monte Carlo ($M_t = 140$ GeV/ c^2) are shown in figures 6.1, 6.2, 6.3, 6.4, 6.5, and 6.6.

These cuts are motivated to reduce the background as follows:

	evts in 15.2 pb^{-1}
(1) $P_T^\mu > 15 \text{ GeV}/c, \eta^\mu < 1.7$ $E_T^e > 15 \text{ GeV}, \eta^e < 2.5$ + id cuts	58
(2) Require Isolated μ 's : $\Delta R_{\mu,\text{jet}} > 0.5$ (for $E_T^{\text{jet}} > 10 \text{ GeV}$)	30
(3) additional μ isolation : $E^{0.4} - E^{0.2} < 4 \text{ GeV}$ (CC) $E^{0.4} - E^{0.2} < 5 \text{ GeV}$ (EC)	27
(4) $\cancel{E}_T > 20 \text{ GeV}$ (Calorimeter/ICD/masslessGap)	15
(5) $\cancel{E}_T > 20 \text{ GeV}$ (μ corrected)	8
(6) small angle μ brem cut : $\Delta R_{\mu,e} > 0.25$	5
(7) Require 1 jet (cone : 0.5), $E_T^{\text{jet}} > 15.0 \text{ GeV}$	1

Table 6.2: Final Analysis Cuts, cumulative effects

- Muon Isolation (cuts 2 and 3): Muons from W decay (as in the standard $t\bar{t}$ decay chain) are typically very isolated. A number of backgrounds, usually muons from b and c quark decay ($\text{QCD} \rightarrow e\mu, Z \rightarrow b\bar{b}, c\bar{c} \rightarrow e\mu$, etc.), produce relatively high P_T muons which are not isolated. These non isolated muons are rejected in two ways:

cut 2 $\Delta R_{\mu,\text{jet}} > 0.5$. Typically a non-isolated muon is very close to a jet, and requiring the muon and jet be well separated is sufficient.

cut 3 Occasionally there is not enough energy to satisfy the jet id criteria and a muon from a b or c decay will not appear near a reconstructed jet. There will, however, be some associated energy deposited in the calorimeter (in addition to the muon mip trace). Making a cut on the energy difference between a cone of $\Delta R = 0.4$

and of $\Delta R = 0.2$ is effective in eliminating such muons.

- Calorimeter missing E_T (cut 4): As noted in section 5.2, $W + \text{jets} \rightarrow \mu + \text{jets}$, where one of the jets then fakes an electron, is a serious background source. Since neither the muon nor the neutrino are seen by the calorimeter, a measurement of the Calorimeter missing E_T is equivalent to a measurement of the P_T of the W . A cut of 20 GeV on this quantity reduces the $W + \text{jets}$ cross section by a factor of 0.22 [161]. For $t\bar{t} \rightarrow e\mu$ events, the calorimeter \cancel{E}_T is derived from the high E_T electron and b jets. This is usually more than 20 GeV, so this cut has little effect on the $t\bar{t}$ acceptance.
- Muon corrected missing E_T (cut 5): For $t\bar{t} \rightarrow e\mu$ events the Muon corrected \cancel{E}_T is due to the two high P_T neutrinos and is usually more than 20 GeV. There are few other sources of $e\mu$ events which produce so much missing E_T . $Z \rightarrow \tau\tau \rightarrow e\mu$ is the primary contributor but its cross section is reduced substantially by this cut.
- Small angle brem cut (cut 6): A high P_T muon will occasionally be accompanied by initial state bremsstrahlung and the majority of these photons will be very close (in $\eta\phi$ space) to the parent muon. If this is the case the photon will be matched to the muon track in the central tracking system and will be labelled by DØRECO as an electron (thus creating an $e\mu$ event). Requiring $\Delta R_{\mu,e} > 0.25$ effectively eliminates such events while having no effect on the $t\bar{t}$ acceptance.

- Jet cut (cut 7): The above selection criteria significantly reduce the background. The remaining background sources ($Z \rightarrow \tau\tau \rightarrow e\mu$, $WW \rightarrow e\mu$, and $W + \text{jets} \rightarrow \mu + \text{jets}(e)$) are all reduced by requiring one or more high P_T jets.

6.3.4 The Candidate - event 417

Only one event survives the final stage of the analysis - event # 58796/417. As can be seen in figures 6.1, 6.2, 6.3, 6.4, 6.5, and 6.6, this is the event which is quite far from the cuts and from all other events. The DØ side view, end view, and a lego plot are shown in figures 6.7, 6.8, and 6.9 respectively.

The corrected event parameters for this event are as given below. The jet energy errors include both the terms from the high and low response jet corrections [162] and the calorimeter resolution (see section 3.5) added in quadrature. The response terms are taken from [163] and are specific to the η of the reconstructed jets. The 90 and 95 % CL lower limits on the missing E_T are derived from a fluctuation Monte Carlo calculation where all entities are randomly fluctuated with Gaussian error distributions [164]. Also, in figure 6.10 are various distributions of selection variables for good electrons from the DØ $W \rightarrow e\nu_e$ sample and arrows indicate the values for the electron in event 417 [165].

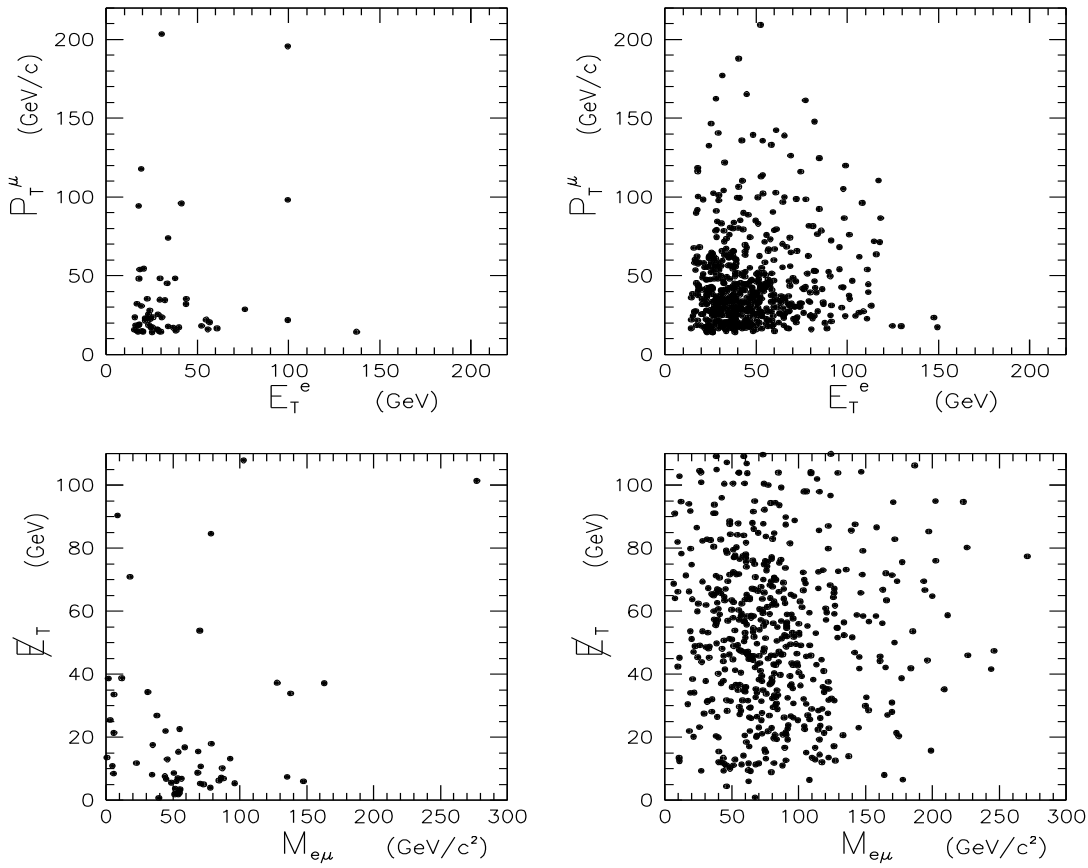


Figure 6.1: P_T^e vs P_T^μ [top] and $M_{e\mu}$ vs E_T [bottom] for data (15.2 pb^{-1}) [left] and $t\bar{t} \rightarrow e\mu$ Monte Carlo ($M_t = 140 \text{ GeV}/c^2$, 2416 pb^{-1}) [right]; cuts: P_T^e, P_T^μ , and id (58 events)

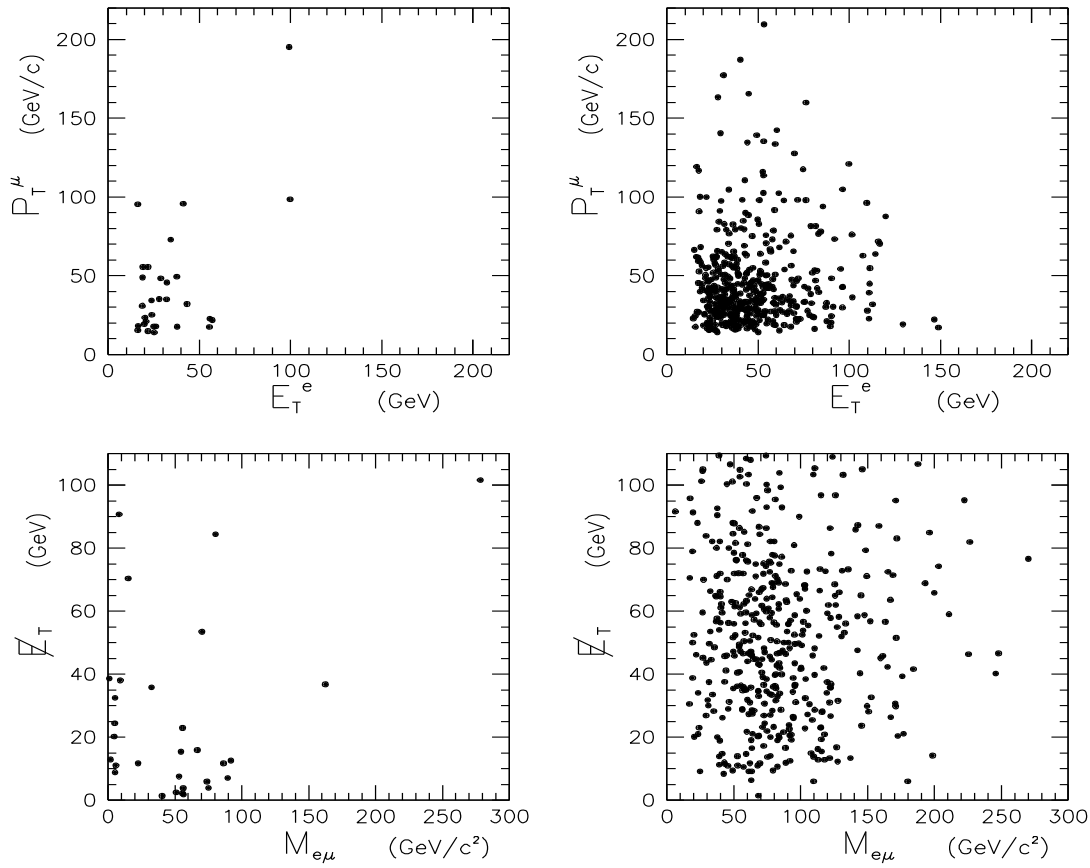


Figure 6.2: P_T^e vs P_T^μ [top] and $M_{e\mu}$ vs E_T^μ [bottom] for data (15.2 pb^{-1}) [left] and $t\bar{t} \rightarrow e\mu$ Monte Carlo ($M_t = 140 \text{ GeV}/c^2$, 2416 pb^{-1}) [right]; cuts: P_T^e, P_T^μ , and Initial μ isolation (30 events)

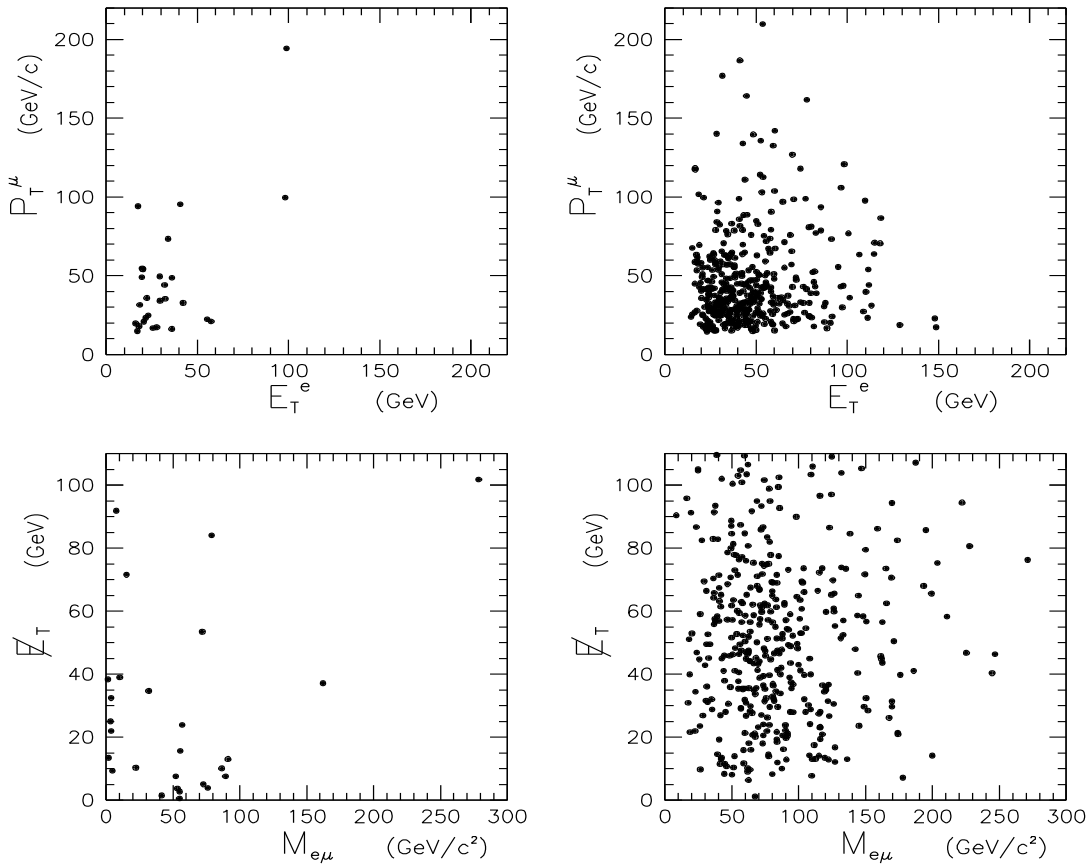


Figure 6.3: P_T^e vs P_T^μ [top] and $M_{e\mu}$ vs E_T^μ [bottom] for data (15.2 pb^{-1}) [left] and $t\bar{t} \rightarrow e\mu$ Monte Carlo ($M_t = 140 \text{ GeV}/c^2$, 2416 pb^{-1}) [right]; cuts: P_T^e, P_T^μ , Initial μ isolation, and Secondary μ isolation (27 events)

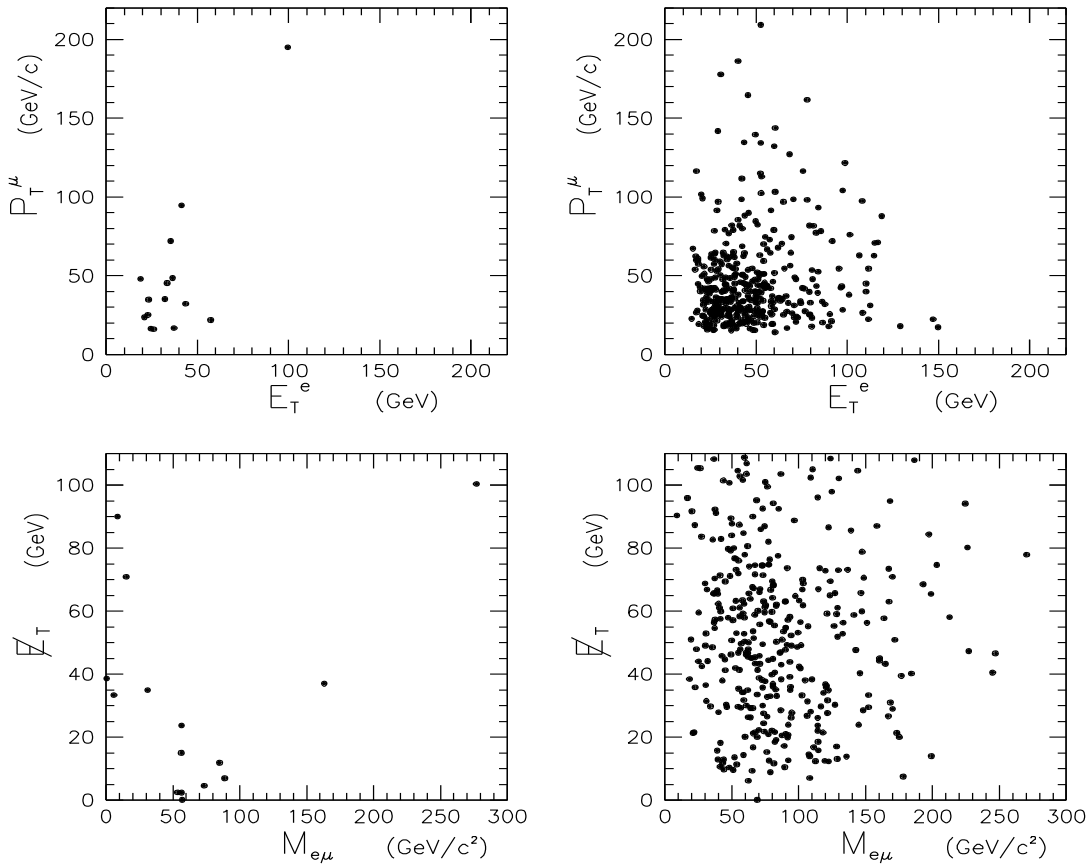


Figure 6.4: P_T^e vs P_T^μ [top] and $M_{e\mu}$ vs \cancel{E}_T [bottom] for data (15.2 pb^{-1}) [left] and $t\bar{t} \rightarrow e\mu$ Monte Carlo ($M_t = 140 \text{ GeV}/c^2$, 2416 pb^{-1}) [right]; cuts: P_T^e, P_T^μ, μ isolation, and \cancel{E}_T (Calorimeter/ICD/masslessGap) (15 events)

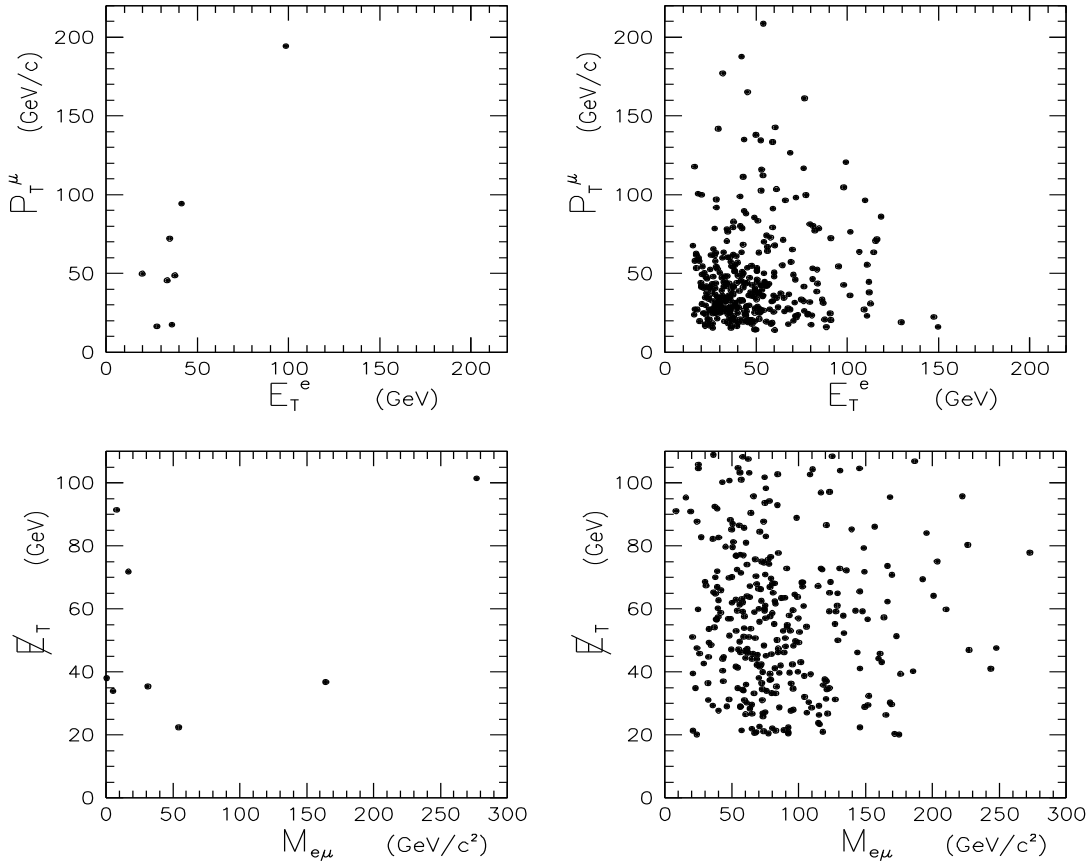


Figure 6.5: P_T^e vs P_T^μ [top] and $M_{e\mu}$ vs \cancel{E}_T [bottom] for data (15.2 pb^{-1}) [left] and $t\bar{t} \rightarrow e\mu$ Monte Carlo ($M_t = 140 \text{ GeV}/c^2, 2416 \text{ pb}^{-1}$) [right]; cuts: P_T^e, P_T^μ , μ isolation, \cancel{E}_T (Calorimeter/ICD/masslessGap), and \cancel{E}_T (μ corrected) (8 events)

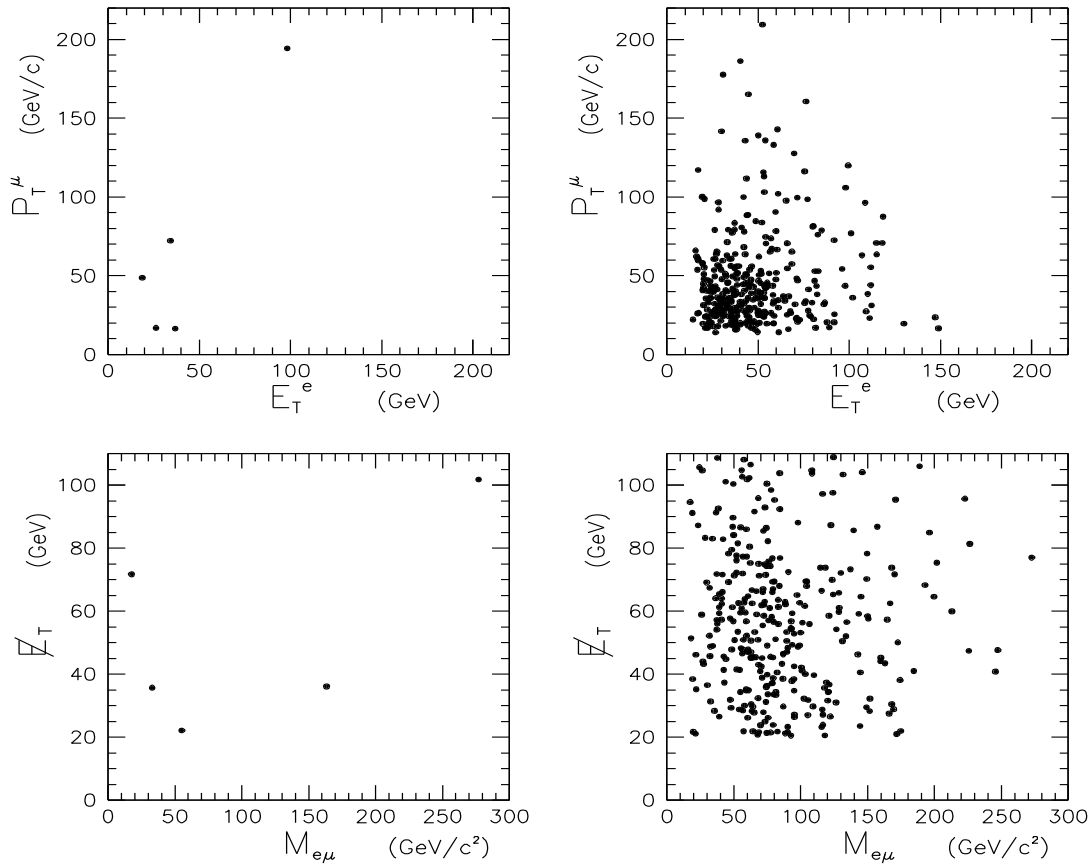


Figure 6.6: P_T^e vs P_T^μ [top] and $M_{e\mu}$ vs E_T^μ [bottom] for data (15.2 pb^{-1}) [left] and $t\bar{t} \rightarrow e\mu$ Monte Carlo ($M_t = 140 \text{ GeV}/c^2$, 2416 pb^{-1}) [right]; cuts: P_T^e, P_T^μ, μ isolation, E_T^μ , and small angle brem (5 events)

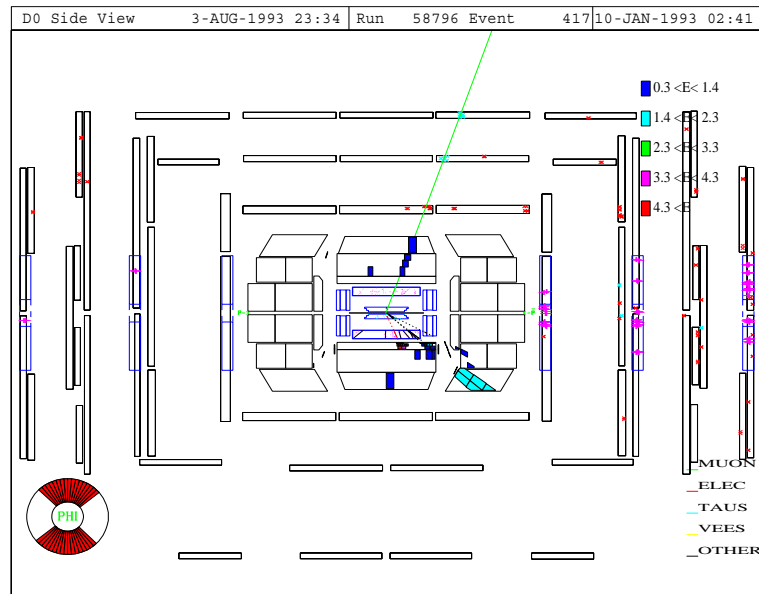


Figure 6.7: Event 417 side view

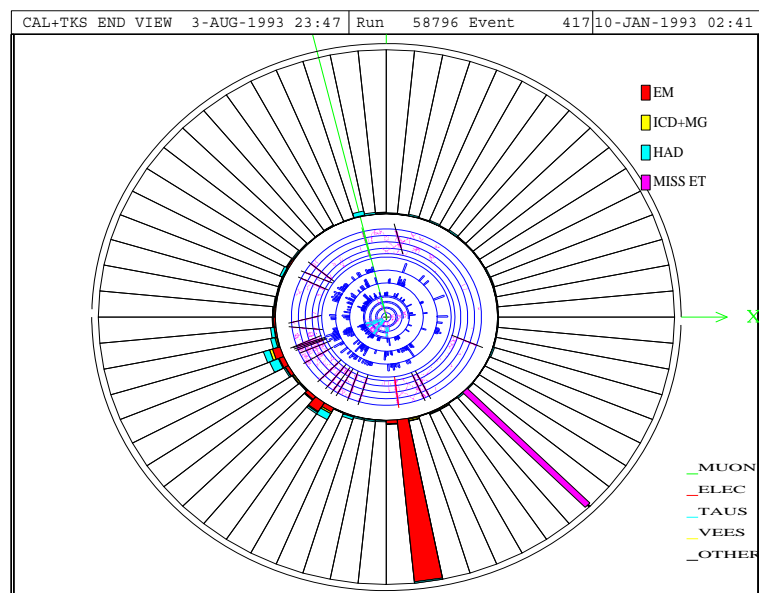


Figure 6.8: Event 417 end view

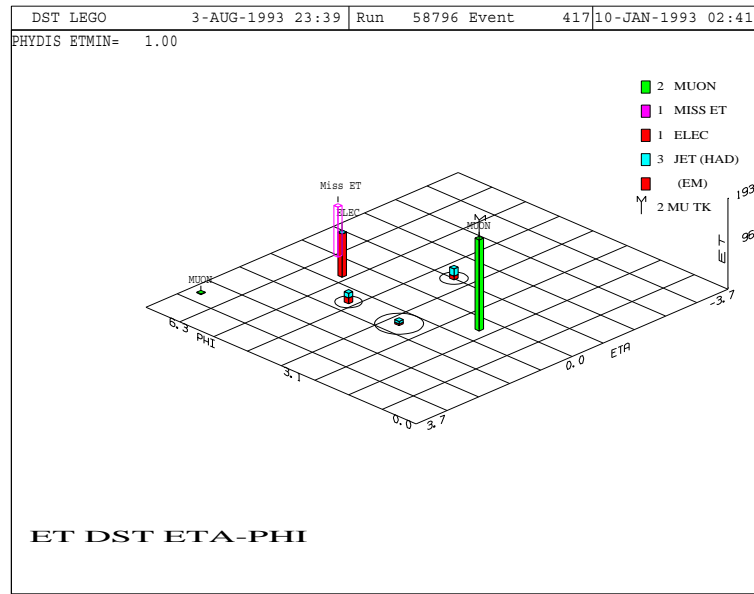


Figure 6.9: Event 417 Lego plot

Muon :

$P_T^\mu = 194.6 \text{ GeV}/c$	$\delta(1/p) = 1/106 \text{ (GeV}/c)^{-1}$
$P_T^\mu > 50.6 \text{ GeV}/c \text{ at } 90\% \text{ cl}$	$P_T^\mu > 40.2 \text{ GeV}/c \text{ at } 95\% \text{ cl}$
$\eta^\mu = 0.33$	$\phi^\mu = 1.82$
$\Delta R^{\min}(\mu, \text{jet}) = 1.40$	global fit $\chi^2 = 14.8$
xy impact parameter = 5.7 cm	floating t0 offset = 39 ns
CDC track match	$dE/dx = 1.0 \text{ mip}$

Electron :

$E_T^e = 98.8 \pm 1.6 \text{ GeV}$	
$\eta^e = 0.40$	$\phi^e = 4.84$
$\Delta R^{\min}(e, \text{jet}) = 1.03$	EM fraction = 0.99
H Matrix $\chi^2 = 51$	Isolation = 0.02
CDC track match	$dE/dx = 1.0 \text{ mip}$
VTX track match	$dE/dx = 0.7 \text{ mip}$

Jet1 :

$$E_T^{\text{jet1}} = 26.1 \pm 4.1 \text{ GeV}$$

$$\eta^{\text{jet1}} = -0.70, \phi^{\text{jet1}} = 3.50$$

no. cells above 1 Gev = 3

rms width : $\Delta\eta = 0.20, \Delta\phi = 0.15$

EM fraction = 0.34

ICD + MG fraction = 0.13 CH fraction = 0.08

Hottest/next Hottest cell ratio = 1.1

Jet2 :

$$E_T^{\text{jet2}} = 23.0 \pm 2.4 \text{ GeV}$$

$$\eta^{\text{jet2}} = 1.10, \phi^{\text{jet2}} = 4.08$$

no. cells above 1 Gev = 5

rms width : $\Delta\eta = 0.17, \Delta\phi = 0.16$

EM fraction = 0.55

ICD + MG fraction = 0.17 CH fraction = 0.15

Hottest/next Hottest cell ratio = 1.3

Jet3 :

$$E_T^{\text{jet3}} = 7.9 \pm 1.2 \text{ GeV}$$

$$\eta^{\text{jet3}} = 1.20, \phi^{\text{jet3}} = 2.92$$

no. cells above 1 Gev = 0

rms width : $\Delta\eta = 0.27, \Delta\phi = 0.32$

EM fraction = 0.44

ICD + MG fraction = 0.18 CH fraction = 0.02

Hottest/next Hottest cell ratio = 2.2

Missing E_T :

Calorimeter Missing E_T : $\cancel{E}_T^{\text{cal}} = 120.0 \text{ GeV}$

Muon corrected Missing E_T : $\cancel{E}_T = 100.7 \text{ GeV}$

$\cancel{E}_T > 56.5 \text{ GeV}$ at 90% cl

$\cancel{E}_T > 53.5 \text{ GeV}$ at 95% cl

Muon – Electron :

$\Delta\phi(\mu, e) = 173^\circ$ $\text{Mass}(\mu, e) = 277 \text{ GeV}/c^2$

$\Delta R(\mu, e) = 3.02$

Muon – \cancel{E}_T :

$\Delta\phi(\mu, \cancel{E}_T) = 147^\circ$

$M_T(\mu, \cancel{E}_T) = 269 \text{ GeV}/c^2$ $P_T(\mu, \cancel{E}_T) = 123 \text{ GeV}/c$

Electron – \cancel{E}_T :

$\Delta\phi(e, \cancel{E}_T) = 40^\circ$

$M_T(e, \cancel{E}_T) = 68 \text{ GeV}/c^2$ $P_T(e, \cancel{E}_T) = 44 \text{ GeV}/c$

Jet – Jet :

$\Delta\phi(\text{jet1}, \text{jet2}) = 34^\circ$ $M(\text{jet1}, \text{jet2}) = 53 \text{ GeV}/c^2$

$\Delta\phi(\text{jet1}, \text{jet3}) = 33^\circ$ $M(\text{jet1}, \text{jet3}) = 33 \text{ GeV}/c^2$

$\Delta\phi(\text{jet2}, \text{jet3}) = 67^\circ$ $M(\text{jet2}, \text{jet3}) = 17 \text{ GeV}/c^2$

6.4 Expected number of Background events

In sections 5.1.6 and 5.2 the cross sections for all expected backgrounds are presented. These cross sections correspond to the final set of cuts discussed in section 6.3.3 (from which only one data event survives). Combined with the luminosity determination in section 6.1.1, the expected numbers of events

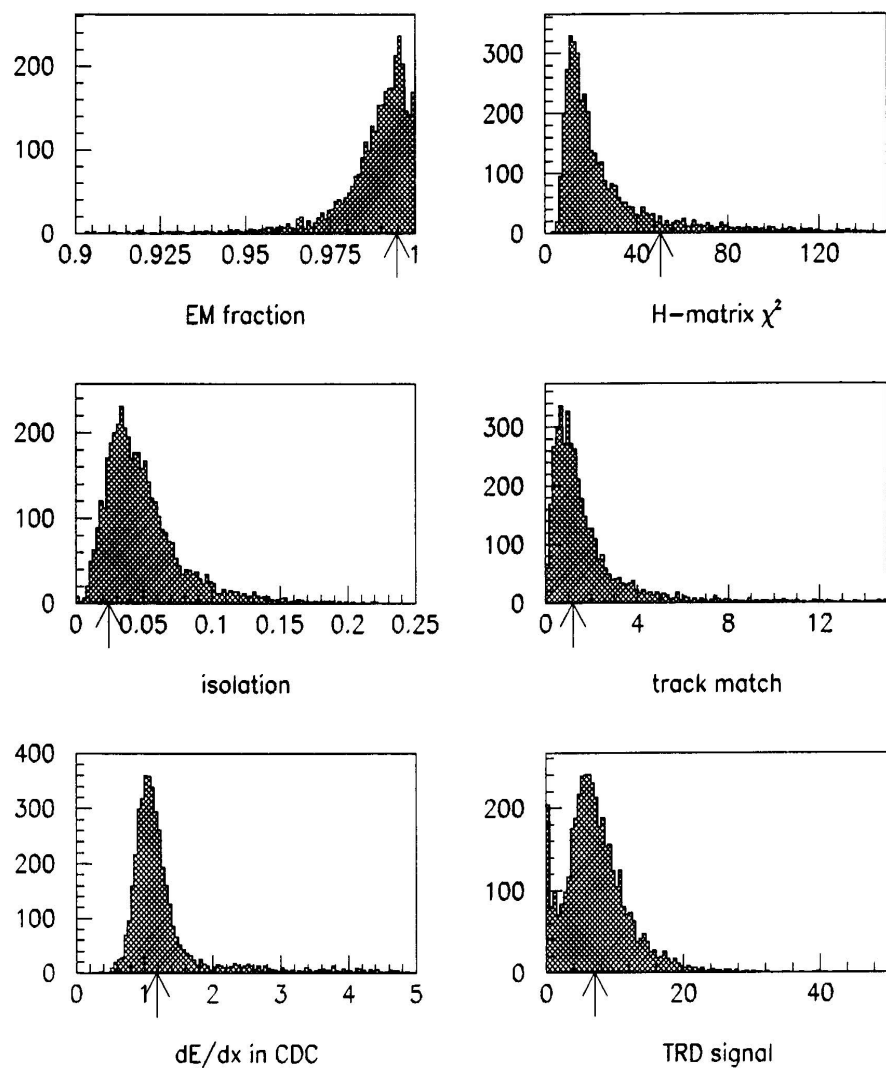


Figure 6.10: Various distributions of selection variables for good electrons from the DØ $W \rightarrow e\nu_e$ sample; arrows indicate the values for the electron in event 417

from each background channel are presented in tables 5.2 and 5.3. Summing the “real” and “fake” contributions (see section 5.3) gives a total background of

$$0.99 \pm 0.03(\text{stat}) \pm 0.22(\text{sys}) \pm 0.06(\text{lum}) \text{ events,}$$

where the standard DØ systematic error of $\pm 12\%$ on the luminosity is assumed.

6.5 Expected $t\bar{t} \rightarrow e\mu$ event yield

In section 5.1.5 the $t\bar{t} \rightarrow e\mu$ efficiencies for ten top masses are presented. As stated, these efficiencies are for the final set of cuts discussed in section 6.3.3. When combined with the luminosity (section 6.1.1) the expected $t\bar{t} \rightarrow e\mu$ event yield is obtained. These efficiencies and their associated event yields are given in table 6.3. The standard DØ systematic error of $\pm 12\%$ on the luminosity is assumed. These results together with the total background given in section 6.4 are shown in figure 6.11.

6.6 The Cross Section Limit

In the absence (and even in the presence) of a top discovery, a determination of the cross section upper limit is of major significance. This is because the cross section limit leads to a lower limit on M_t , which, as discussed in section 1.3, is one of the few missing pieces of the Standard Model. The cross section limit can be based on one or more channels. In the next section the cross section limit based only on the $e\mu$ analysis is presented. This is followed

M_t (GeV/c ²)	$\sigma \cdot \text{BR}_{e\mu}$ (pb)	efficiency(total)	events in 15.2 pb ⁻¹
70	16.79	$7.88 \pm 0.05 \pm 1.48$	$20.10 \pm 0.12 \pm 4.27 \pm 2.41$
80	8.27	$11.06 \pm 0.03 \pm 2.07$	$13.91 \pm 0.03 \pm 2.95 \pm 1.67$
90	4.44	$13.48 \pm 0.03 \pm 2.52$	$9.11 \pm 0.02 \pm 1.93 \pm 1.09$
100	2.54	$14.63 \pm 0.04 \pm 2.74$	$5.66 \pm 0.01 \pm 1.20 \pm 0.68$
110	1.52	$15.78 \pm 0.03 \pm 2.96$	$3.65 \pm 0.01 \pm 0.77 \pm 0.44$
120	0.96	$16.96 \pm 0.04 \pm 3.18$	$2.48 \pm 0.01 \pm 0.53 \pm 0.30$
140	0.42	$18.77 \pm 0.06 \pm 3.52$	$1.19 \pm 0.00 \pm 0.25 \pm 0.14$
160	0.20	$19.59 \pm 0.05 \pm 3.67$	$0.60 \pm 0.00 \pm 0.13 \pm 0.07$
180	0.10	$19.97 \pm 0.05 \pm 3.74$	$0.32 \pm 0.00 \pm 0.07 \pm 0.04$
200	0.06	$20.51 \pm 0.05 \pm 3.84$	$0.17 \pm 0.00 \pm 0.04 \pm 0.02$

Table 6.3: $t\bar{t} \rightarrow e\mu$ efficiency (errors: stat, sys) and expected event yield (errors: stat, sys, lum)

by the cross section limit utilizing the available dilepton channels and finally by the cross section limit based on all available channels.

6.6.1 $e\mu$ only

The number of events, N_{exp} , expected in a single channel is given by

$$N_{\text{exp}} = \sigma \cdot (\varepsilon \pm \Delta\varepsilon) \cdot \left(\int \mathcal{L} dt \pm \Delta \int \mathcal{L} dt \right)$$

where σ is the cross section for that channel, ε is the efficiency, and $\int \mathcal{L} dt$ is the integrated luminosity. Therefore the upper limit on the cross section (σ_{ul}) is given by

$$\sigma_{\text{ul}} = \frac{N}{(\varepsilon - \Delta\varepsilon) \cdot (\int \mathcal{L} dt - \Delta \int \mathcal{L} dt)}.$$

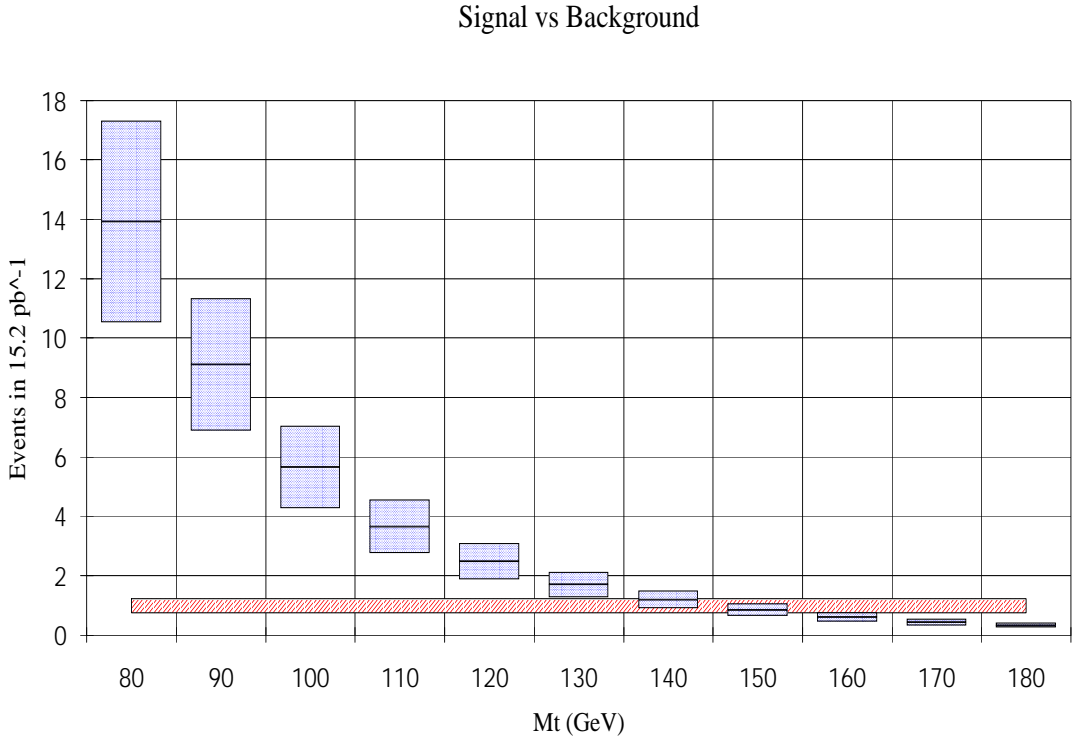


Figure 6.11: Expected number of $t\bar{t} \rightarrow e\mu$ signal events as a function of M_t and total expected background

For 1 event observed, $N = 4.74$ at 95 % CL [166]. Zero background events are assumed since that gives the most conservative limit. As shown in section 6.1.1, the luminosity for the $e\mu$ analysis is $\int \mathcal{L} dt = 15.2 \text{ pb}^{-1}$ with an uncertainty of $\Delta \int \mathcal{L} dt = 1.8 \text{ pb}^{-1}$ (12%). The efficiencies are given in table 6.3. Scaling each value of σ_{ul} thus obtained by a factor of 81/2 gives the upper limit on the total top production cross section ($\sigma_{\text{ul}}^{\text{Total}}$). These values are shown in table 6.4 and figure 6.12.

M_t (GeV/c ²)	$\sigma_{\text{ul}}^{e\mu}$ at 95 % CL	$\sigma_{\text{ul}}^{\text{Total}}$ at 95 % CL
70	5.54	224.2
80	3.94	159.7
90	3.46	140.2
100	2.98	120.7
110	2.76	111.9
120	2.57	104.2
140	2.32	94.1
160	2.22	90.1
180	2.18	88.4

Table 6.4: cross section limit from $e\mu$ channel only

6.6.2 Combining channels

To correctly determine a limit based on more than one channel requires more sophisticated methods. The D \emptyset top group makes use of two such methods [167] which give identical results. The first method is an analytical calculation (as in section 6.6.1) which convolutes the Poisson probability for the number of events with Gaussian distributions for uncertainties in luminosity, efficiency, and background level. The second method is a Monte Carlo method which determines the probability of the actual experimental outcome for a given cross section. The results for the combined $e\mu$ and ee channels are given in table 6.5 and for the combined $e\mu, ee, e + \text{jets}$, and $\mu + \text{jets}$ channels are given in table 6.6.

M_t (GeV/c ²)	$\sigma_{\text{ul}}^{\text{dilepton}}$ at 95 % CL
90	108.7
100	80.9
120	68.7
140	65.2
160	61.6
180	57.3

Table 6.5: Combined $e\mu$ and ee cross section upper limit

M_t (GeV/c ²)	$\sigma_{\text{ul}}^{\text{Total}}$ at 95 % CL
90	65.7
100	45.5
120	24.4
140	18.8
160	16.4

Table 6.6: Combined $e\mu, ee, e + \text{jets}$, and $\mu + \text{jets}$ cross section upper limit

6.6.3 What can we say about a limit on M_t

The most conservative top mass lower limit is obtained by determining where the cross section upper limit curves presented in section 6.6 cross the theoretical cross section lower limit. These curves are shown in figures 6.12 and 6.13. The errors on the theoretical cross section are due primarily to uncertainties in the renormalization scale and structure functions. As can be seen, the $e\mu$ channel alone gives a limit of

$$M_t > 92 \text{ GeV}/c^2 \text{ @ 95\%CL.}$$

Combining the $e\mu$ analysis with the ee , $e + \text{jets}$, and $\mu + \text{jets}$ analyses gives a limit of $M_t > 132 \text{ GeV}/c^2$ [168].

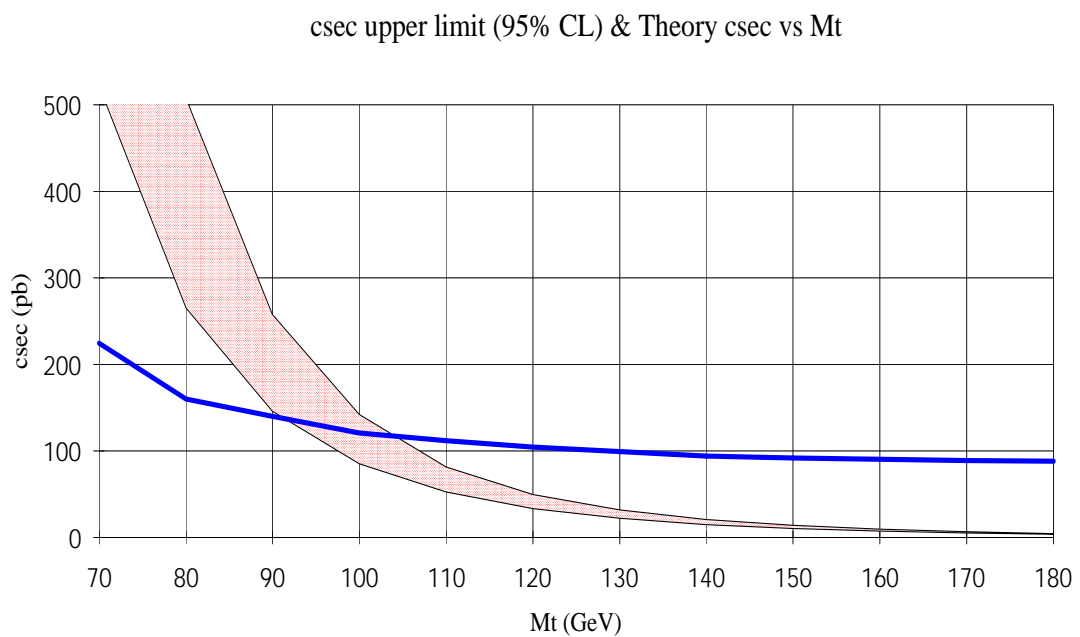


Figure 6.12: DØ cross section upper limit (95 % CL) and Laenen *et al.* cross section vs M_t – $e\mu$ channel only

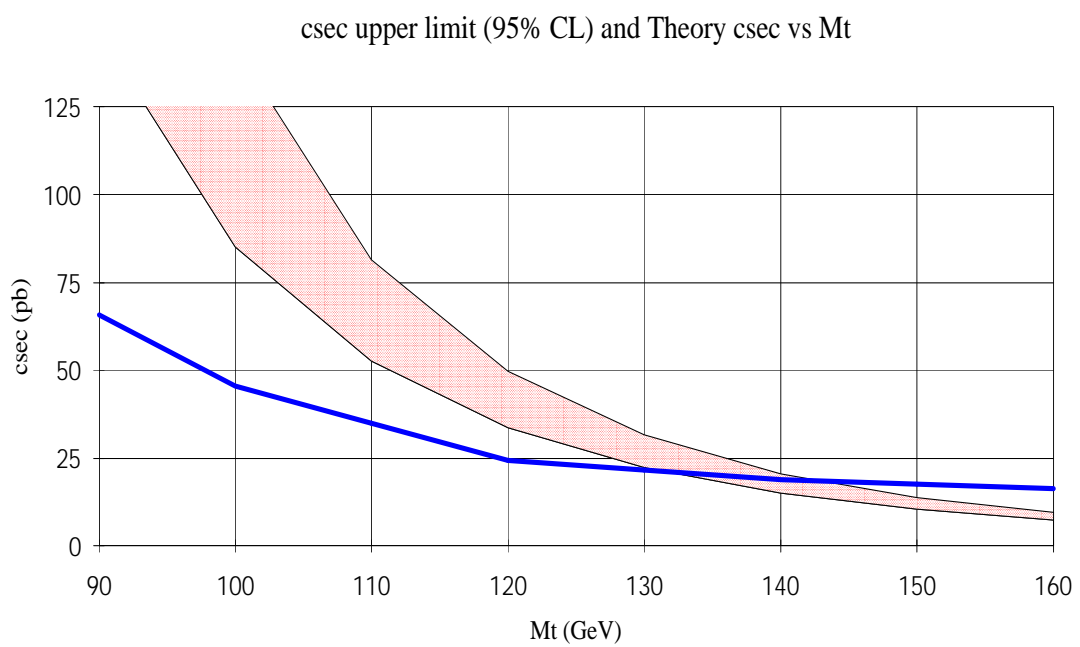


Figure 6.13: DØ cross section upper limit (95 % CL) and Laenen *et al.* cross section vs M_t - $e\mu, ee, e + \text{jets}$, and $\mu + \text{jets}$ channels combined

Chapter 7

Conclusion

A search for evidence of $t\bar{t}$ production through the subsequent decay to $e\mu+X$ has been performed. The analysis presented assumes standard model couplings and branching ratios and is based on an integrated luminosity of $15.2 \pm 1.8 \text{ pb}^{-1}$ acquired by the DØ detector during its first collider run. The data analysis is summarized in table 7.1. The goal of any such analysis is to minimize the background contributions while maximizing the acceptance for the expected signal. As described in table 6.3 and section 5.3, the expected run 1A yield for $t\bar{t} \rightarrow e\mu$ varies from $0.17 \pm 0.00(\text{stat}) \pm 0.04(\text{sys}) \pm 0.02(\text{lumsys})$ events at $M_t = 200 \text{ GeV}/c^2$ to $20.10 \pm 0.12(\text{stat}) \pm 4.27(\text{sys}) \pm 2.41(\text{lumsys})$ events at $M_t = 70 \text{ GeV}/c^2$, with an expected background (with current selection cuts) of $1.09 \pm 0.03(\text{stat}) \pm 0.34(\text{sys}) \pm 0.07(\text{lumsys})$ events. A single event survives from all the selection criteria. While this event is quite interesting and unusual, it cannot be considered as conclusive evidence for top. On the basis of this one candidate event, a lower top mass limit of $92 \text{ GeV}/c^2$ at the 95% CL is obtained (using NNLO cross section calculations).

	evts in 15.2 pb^{-1}
$P_T^\mu > 5, 10 \text{ GeV}/c, \eta^\mu < 1.7$	1388
$E_T^{\text{em}} > 5, 10 \text{ GeV}, \eta^{\text{em}} < 2.5 + \text{loose id cuts}$	
$P_T^\mu > 15 \text{ GeV}/c, \eta^\mu < 1.7$	713
$E_T^{\text{em}} > 15 \text{ GeV}, \eta^{\text{em}} < 2.5 + \text{loose id cuts}$	
+ bad run and μ blank rejection	
$P_T^\mu > 15 \text{ GeV}/c, \eta^\mu < 1.7$	58
$E_T^e > 15 \text{ GeV}, \eta^e < 2.5 + \text{id cuts} + \text{trigger}$	
Require Isolated μ 's : $\Delta R_{\mu, \text{jet}} > 0.5$ (for $E_T^{\text{jet}} > 10 \text{ GeV}$)	30
additional μ isolation : $E^{0.4} - E^{0.2} < 4 \text{ GeV}$ (CC) $E^{0.4} - E^{0.2} < 5 \text{ GeV}$ (EC)	27
$E_T^\mu > 20 \text{ GeV}$ (Calorimeter/ICD/massless Gap)	15
$E_T^\mu > 20 \text{ GeV} (\mu \text{ corrected})$	8
small angle μ brem cut : $\Delta R_{\mu, e/\gamma} > 0.25$	5
Require 1 jet(cone : 0.5), $E_T^{\text{jet}} > 15.0 \text{ GeV}$	1

Table 7.1: Run 1A analysis summary

Ongoing are several studies connected to the present analysis. A log likelihood technique is being developed with the goal of assigning a probability that a given event is due to $t\bar{t}$ production. Such a technique will be very useful as more candidates appear in future runs. Studies to correlate the expected background and data over the full set of cuts are well underway. Early indications are that there is good agreement. The results of these studies are expected to lead to more sophisticated multidimensional cuts which will result in greater signal acceptance and background rejection.

A new collider run is set to begin in January 1994 and is expected to collect

$\sim 100 \text{ pb}^{-1}$. With no changes in the cuts a total of 7 background events are expected. As an exercise it may be assumed that more sophisticated cuts will remove these events without reducing the efficiency. In this case, if there is no evidence for top this will push the mass limit from the $e\mu$ channel to $\sim 145 \text{ GeV}/c^2$ at the 95% CL (assuming that event 417 remains as the only candidate).

Appendix A

Cross Sections and Branching Ratios

A.1 Total Cross Sections: σ_{tot}

M_t (GeV)	$\sigma_{p\bar{p} \rightarrow t\bar{t}} =$		
	lower(pb)	central(pb)	upper(pb)
70	521	680	1102
80	265	335	507
90	145	180	258
100	85.2	103	142
110	52.7	61.6	81.4
120	33.7	38.9	49.7
140	15.1	16.9	20.5
160	7.41	8.16	9.53
180	3.86	4.21	4.78
200	2.09	2.26	2.52

[42]

.....

$$\begin{aligned}
\sigma_{p\bar{p} \rightarrow Z} &= 6257.5 \text{ pb}^1 \\
\sigma_{p\bar{p} \rightarrow W+X} &= 20,857 \text{ pb}^2
\end{aligned}
\tag{169}$$

.....

$$\begin{aligned}
\sigma_{p\bar{p} \rightarrow W+n\text{jets}}(n \geq 0) &= 1956.00 \pm 7.27 \pm 391.00 \text{ pb} \\
(n \geq 1) &= 566.80 \pm 3.33 \pm 113.00 \text{ pb} \\
(n \geq 2) &= 168.60 \pm 1.33 \pm 67.44 \text{ pb} \\
(n \geq 3) &= 45.44 \pm 0.63 \pm 27.26 \text{ pb} \\
(n \geq 4) &= 11.50 \pm 0.25 \pm 9.20 \text{ pb}
\end{aligned}
\tag{171}$$

.....

$$\sigma_{p\bar{p} \rightarrow W^+ W^-} \approx 10 \text{ pb}
\tag{172}$$

.....

$$\sigma_{p\bar{p} \rightarrow W^+ Z} \approx 1.2 \text{ pb}
\tag{173}$$

$$\implies \sigma_{p\bar{p} \rightarrow W^\pm Z} \approx 2.4 \text{ pb}$$

.....

$$\sigma_{p\bar{p} \rightarrow W^+ \gamma} \approx 30.3 \text{ pb}
\tag{174}$$

$$\implies \sigma_{p\bar{p} \rightarrow W^\pm \gamma} \approx 60.6 \text{ pb}$$

¹data are 5% over this (central values averaged over e, μ , & τ channels). [170]

²data are 1% over this. [170]

.....

$$\sigma_{QCD \rightarrow b\bar{b}} \approx 25,000,000 \text{ pb}$$

[175]

.....

$$\sigma_{QCD \rightarrow c\bar{c}} \approx 300,000,000 \text{ pb}$$

[175]

.....

$$\sigma_{p\bar{p} \rightarrow \gamma \rightarrow ee} \approx 300 \text{ pb}^1$$

$$\sigma_{p\bar{p} \rightarrow \gamma \rightarrow \mu\mu} \approx 300 \text{ pb}^2$$

$$\sigma_{p\bar{p} \rightarrow \gamma \rightarrow \tau\tau} \approx 300 \text{ pb}^3$$

[176]

A.2 Branching Ratios: $(BR)_i$

$$BR(W \rightarrow e\nu_e, \mu\nu_\mu)^4 = 1/9 \approx 11.1\%$$

$$BR(Z \rightarrow ee, \mu\mu, \tau\tau) \approx 3.34\%$$

$$BR(Z \rightarrow u\bar{u}, c\bar{c}) \approx 11.8\%$$

$$BR(Z \rightarrow d\bar{d}, s\bar{s}, b\bar{b}) \approx 15.2\%$$

[177]

$$^1 M_{ee} > 25 \text{ GeV}$$

$$^2 M_{\mu\mu} > 25 \text{ GeV}$$

$$^3 M_{\tau\tau} > 25 \text{ GeV}$$

¹Ignoring $W \rightarrow \tau \rightarrow e\nu_e$ and $W \rightarrow \tau \rightarrow \mu\nu_\mu$

$$\implies \begin{aligned} \text{BR}(W^+W^- \rightarrow ee + X, \mu\mu + X) &= 1/81 \approx 1.23\% \\ \text{BR}(W^+W^- \rightarrow e\mu + X) &= 2/81 \approx 2.47\% \end{aligned}$$

.....

$$\begin{aligned} \text{BR}(\tau \rightarrow \mu\bar{\nu}_\mu\nu_\tau) &\approx 17.8\% \\ \text{BR}(\tau \rightarrow e\bar{\nu}_e\nu_\tau) &\approx 17.7\% \end{aligned}$$

[52]

$$\implies \begin{aligned} \text{BR}(\tau^+\tau^- \rightarrow ee + X, \mu\mu + X) &\approx 3.1\% \\ \text{BR}(\tau^+\tau^- \rightarrow e\mu + X) &\approx 6.3\% \\ \text{BR}(\tau^+\tau^- \rightarrow e^+\mu^- + X) &\approx 3.1\% \end{aligned}$$

.....

$$\begin{aligned} \text{BR}(c \rightarrow s e \nu_e, s \mu \nu_\mu) &\approx 8.6\% \\ \text{BR}(b \rightarrow c e \bar{\nu}_e, c \mu \bar{\nu}_\mu) &\approx 10.3\% \end{aligned}$$

[178]

$$\implies \begin{aligned} \text{BR}(c\bar{c} \rightarrow ee, \mu\mu) &= [\text{BR}(c \rightarrow e, \mu)]^2 &\approx 0.74\% \\ \text{BR}(c\bar{c} \rightarrow e\mu) &= 2 \cdot [\text{BR}(c \rightarrow e, \mu)]^2 &\approx 1.48\% \\ \text{BR}(b\bar{b} \rightarrow ee, \mu\mu) &= [\text{BR}(b \rightarrow e, \mu)]^2 \\ &\quad + 2 \cdot [\text{BR}(b \rightarrow e, \mu) \cdot \text{BR}(c \rightarrow e, \mu)] &\approx 2.83\% \\ \text{BR}(b\bar{b} \rightarrow e\mu) &= 2 \cdot [\text{BR}(b \rightarrow e, \mu)]^2 \\ &\quad + 4 \cdot [\text{BR}(b \rightarrow e, \mu) \cdot \text{BR}(c \rightarrow e, \mu)] &\approx 5.67\% \end{aligned}$$

A.3 Relevant Cross Sections: $\sigma_i = \sigma_{tot} \cdot (\text{BR})_i$

$M_t(\text{GeV})$	$\sigma_{p\bar{p} \rightarrow t\bar{t} \rightarrow e\mu} = \sigma_{t\bar{t}} \cdot \text{BR}(W^+W^- \rightarrow e\mu + X)$		
	lower(pb)	central(pb)	upper(pb)
70	12.86	16.79	27.21
80	6.54	8.27	12.52
90	3.58	4.44	6.37
100	2.10	2.54	3.51
110	1.30	1.52	2.01
120	0.83	0.96	1.23
140	0.37	0.42	0.51
160	0.18	0.20	0.24
180	0.095	0.104	0.118
200	0.052	0.056	0.062
.....			
$\sigma_{QCD \rightarrow e\mu}$	$= \sigma_{QCD \rightarrow b\bar{b}} \cdot \text{BR}(b\bar{b} \rightarrow e\mu) +$ $\sigma_{QCD \rightarrow c\bar{c}} \cdot \text{BR}(c\bar{c} \rightarrow e\mu)$		$\approx 28,375,000 \text{ pb}$
$\sigma_{Z \rightarrow \tau\bar{\tau} \rightarrow e\mu}$	$= \sigma_Z \cdot \text{BR}(Z \rightarrow \tau\bar{\tau}) \cdot \text{BR}(\tau\bar{\tau} \rightarrow e\mu)$		$\approx 13.24 \text{ pb}$
$\sigma_{Z \rightarrow b\bar{b} \rightarrow e\mu}$	$= \sigma_Z \cdot \text{BR}(Z \rightarrow b\bar{b}) \cdot \text{BR}(b\bar{b} \rightarrow e\mu)$		$\approx 53.93 \text{ pb}$
$\sigma_{Z \rightarrow c\bar{c} \rightarrow e\mu}$	$= \sigma_Z \cdot \text{BR}(Z \rightarrow c\bar{c}) \cdot \text{BR}(c\bar{c} \rightarrow e\mu)$		$\approx 10.92 \text{ pb}$
$\sigma_{\gamma \rightarrow \tau\bar{\tau} \rightarrow e\mu}$	$= \sigma_{\gamma \rightarrow \tau\bar{\tau}} \cdot \text{BR}(\tau\bar{\tau} \rightarrow e\mu)$		$\approx 18.9 \text{ pb}$
$\sigma_{W^+W^- \rightarrow e\mu}$	$= \sigma_{W^+W^-} \cdot 2 \cdot \text{BR}(W \rightarrow \mu) \cdot \text{BR}(W \rightarrow e)$	$\approx 0.25 \text{ pb}$	
$\sigma_{WZ \rightarrow e\mu}$	$= \sigma_{WZ} \cdot [\text{BR}(W \rightarrow e) \cdot \text{BR}(Z \rightarrow \mu\mu) +$ $\text{BR}(W \rightarrow \mu) \cdot \text{BR}(Z \rightarrow ee)]$		$\approx 0.018 \text{ pb}$

Bibliography

- [1] F. Kafka (translated by T. and J. Stern), “The Top” in *Franz Kafka: The Complete Stories*, edited by N. Glatzer (Schocken Books Inc., New York, 1971), p. 444.
- [2] V. Barger and R. Phillips, *Collider Physics*, (Addison-Wesley Publishing Co., New York, 1987), p. 3.
- [3] A. Einstein, *The Principle of Relativity*, (Methuen, 1923) reprinted by Dover, New York (1952)
- [4] J. C. Maxwell, *Treatise on Electricity and Magnetism*, 3rd edition (1891), 2 vols. reprint by Dover, New York (1954)
- [5] P. A. M. Dirac, *Proc. R. Soc. London A* **114**, p. 243,710 (1927)
- [6] R. P. Feynman, *Phys. Rev.* **76**, p. 749,769 (1949)
- [7] R. P. Feynman, *QED*, (Princeton University Press, Princeton, New Jersey, 1985) p. 7.
- [8] E. Fermi, *Z. Phys.* **88**, p. 161 (1934)

- [9] R. Crease and C. Mann, *The Second Creation*, (MacMillian Publishing Co., New York, 1986), p. 211.
- [10] C. S. Wu *et al.*, *Phys. Rev.* **105**, p. 1413 (1957)
- [11] M. Gell-Mann and R. P. Feynman, *Phys. Rev.* **109**, p. 193 (1958)
- [12] E. C. G. Sudarshan and R. E. Marshak, *Phys. Rev.* **109**, p. 1860 (1958)
- [13] T. P. Cheng and L. F. Li, *Gauge Theory of Elementary Particle Physics*, (Oxford University Press, New York, 1984) p. 401-409.
- [14] R. Cahn and G. Goldhaber, *The Experimental Foundations of Particle Physics*, (Cambridge University Press, New York, 1989), p. 379.
- [15] UA1 Collaboration, *Phys. Lett.*, **122B**, p. 103 (1983)
- [16] UA2 Collaboration, *Phys. Lett.*, **122B**, p. 476 (1983)
- [17] UA1 Collaboration, *Phys. Lett.*, **126B**, p. 398 (1983)
- [18] UA2 Collaboration, *Phys. Lett.*, **129B**, p. 130 (1983)
- [19] M. Gell-Mann, *Phys. Lett.* **8**, p. 214. (1964)
- [20] R. Crease and C. Mann, *The Second Creation*, (MacMillian Publishing Co., New York, 1986) p. 328.
- [21] H. Fritzsch and M. Gell-Mann, *Proceedings of the XVI International Conference on High Energy Physics*, Fermilab, September 1972, p. 135.
- [22] D. J. Gross and F. Wilczek, *Phys. Rev. Lett.* **30**, p. 1343 (1973)

- [23] H. D. Politzer, *Phys. Rev. Lett.* **30**, p. 1346 (1973)
- [24] R. Crease and C. Mann, *The Second Creation*, (MacMillian Publishing Co., New York, 1986) p. 329.
- [25] M. Kaku, *Quantum Field Theory*, (Oxford University Press, New York, 1993) p. 13.
- [26] T. P. Cheng and L. F. Li, *Gauge Theory of Elementary Particle Physics*, (Oxford University Press, New York, 1984), pp. 347-348.
- [27] Particle Data Group, “Review of Particle Properties”, *Phys. Rev. D* **45**, *Part II*, p. III.65 (1992)
- [28] J. Donoghue, E. Golowich, and B. Holstein, *Dynamics of the Standard Model*, (Cambridge University Press, New York, 1992) p. 1.
- [29] A. S. Kronfeld and P. B. Mackenzie, *Progress in QCD using Lattice Gauge Theory*, FERMILAB-Pub-93/058-T, 1993 (unpublished)
- [30] R. Marshak, *Conceptual Foundations of Modern Particle Physics*, (World Scientific Press, Singapore, 1993) p. 403.
- [31] I. Hinchliffe, “Supersymmetric Models of Particle Physics and their Phenomenology” in *Ann. Rev. Nuc. Sci.*, Vol. 36, (Annual Reviews Inc., Palo Alto, 1986) pp. 505-543.
- [32] P. D. B. Collins, A. D. Martin, and E. J. Squires, *Particle Physics and Cosmology*, (John Wiley & Sons, New York, 1989) p. 311-368.

- [33] M. B. Green, J. H. Schwarz, and E. Witten, *Superstring Theory, Vols I, II*, (Cambridge University Press, New York, 1987)
- [34] F. Abe *et al.* (CDF Collaboration), *Phys. Rev. D* **45**, 3921 (1992)
- [35] M. Shapiro and J. L. Siegrist, “Hadron Collider Physics” in *Ann. Rev. Nuc. Sci.*, Vol. 41, (Annual Reviews Inc., Palo Alto, 1991) p. 125.
- [36] E. Laenen, J. Smith, and W. L. van Neerven, *Top Quark Production Cross Section*, FERMILAB-Pub-93/270-T, August 1993, figure 2. (unpublished)
- [37] E. Laenen, J. Smith, and W. L. van Neerven, *Top Quark Production Cross Section*, FERMILAB-Pub-93/270-T, August 1993, p. 3. (unpublished)
- [38] R. K. Ellis and W. J. Stirling, *QCD and Collider Physics*, FERMILAB-Conf-90/164-T, August 1990, p. 98-105. (unpublished)
- [39] W. Beenakker, H. Kuijf, W. L. van Neerven, and J. Smith, *Phys. Rev. D* **40**, p. 54 (1989)
- [40] R. K. Ellis, *Phys. Lett. B* **259**, p. 492 (1991)
- [41] E. Laenen, Private communication.
- [42] E. Laenen, J. Smith, and W. L. van Neerven, *Top Quark Production Cross Section*, FERMILAB-Pub-93/270-T, August 1993 (unpublished)
- [43] J. Gunion, H. Haber, G. Kane, and S. Dawson, *Higgs Hunter’s Guide*, (Addison-Wesley Publishing Co., New York, 1990) p. 11.

- [44] M. E. Peskin, "Theory of Precision Electroweak Measurements" in *Physics at the 100 GeV Mass Scale*, (Proceedings of the Seventeenth SLAC Summer Institute on Particle Physics, Stanford, 1989) edited by E. C. Brennan, p. 105. (unpublished)
- [45] G.L. Kane, "Top Quark Topics" in *Gauge Bosons and Heavy Quarks*, (Proceedings of the Eighteenth SLAC Summer Institute on Particle Physics, Stanford, 1990) edited by J. Hawthorne, p. 126. (unpublished)
- [46] J. Donoghue, E. Golowich, and B. Holstein, *Dynamics of the Standard Model*, (Cambridge University Press, New York, 1992) p. 457.
- [47] G.L. Kane, "Top Quark Topics" in *Gauge Bosons and Heavy Quarks*, (Proceedings of the Eighteenth SLAC Summer Institute on Particle Physics, Stanford, 1990) edited by J. Hawthorne, p. 125. (unpublished)
- [48] M. Contreras, Ph. D. Thesis, Brandeis University, *Search for the Top Quark in Electron-Muon Events in the Collider Detector at Fermilab*, April 1990, p. 4. (unpublished)
- [49] G. L. Kane and M. Peskin, *Nucl. Phys. B* **195** p. 29. (1982)
- [50] CLEO Collaboration, *Phys. Rev. D* **35** p. 3733. (1987)
- [51] J. Donoghue, E. Golowich, and B. Holstein, *Dynamics of the Standard Model*, (Cambridge University Press, New York, 1992) pp. 389-390.
- [52] Particle Data Group, "Particle Properties Data Booklet" from *Phys. Rev. D* **45**, *Part II*, p. 12. (1992)

- [53] F. Close, M. Martin, and C. Sutton, *The Particle Explosion*, (Oxford University Press, New York, 1987) pp. 102-172.
- [54] R. Fernow, *Introduction to Experimental Particle Physics*, (Cambridge University Press, Cambridge, 1986) pp. 93-123.
- [55] “Fermilab III: Building for the Future” in *Fermilab Annual Report, 1990*, p. 61. (unpublished)
- [56] H. T. Edwards, “The Tevatron Energy Doubler: A Superconducting Accelerator” in *Ann. Rev. Nuc. Sci.*, Vol. 35, (Annual Reviews Inc., Palo Alto, 1985) pp. 605-659.
- [57] L. M. Lederman, “The Tevatron” in *Sci. Am.*, Vol. 264, Num. 3, (Scientific American, Inc., New York, March 1991) p. 52.
- [58] R. Fernow, *Introduction to Experimental Particle Physics*, (Cambridge University Press, Cambridge, 1986) pp. 96.
- [59] L. M. Lederman, “The Tevatron” in *Sci. Am.*, Vol. 264, Num. 3, (Scientific American, Inc., New York, March 1991) p. 53.
- [60] “Collider Run Sets World Luminosity Records” in *Fermilab Annual Report, 1992*, p. 9. (unpublished)
- [61] J. Thompson, *The Accelerator*, DØ Internal note in preparation
- [62] “Fermilab III: Building for the Future” in *Fermilab Annual Report, 1990*, p. 65. (unpublished)

- [63] "The Fermilab Upgrade - An Overview", January 9, 1989 (unpublished)
- [64] "Main Injector Construction Begins" in *Fermilab Annual Report, 1992*, p. 42. (unpublished)
- [65] M. Tuts, "DØ Announces First Physics Results" in *Fermilab Annual Report, Winter 1993*, p. 27. (unpublished)
- [66] P. Grannis, "DØ Collaboration prepares for first run" in *Fermilab Annual Report, Fall 1991*, p. 9. (unpublished)
- [67] H. Williams, "Design Principles of Detectors at Colliding Beams" in *Ann. Rev. Nuc. Sci.*, Vol. 36, (Annual Reviews Inc., Palo Alto, 1986) p. 366.
- [68] H. Williams, "Design Principles of Detectors at Colliding Beams" in *Ann. Rev. Nuc. Sci.*, Vol. 36, (Annual Reviews Inc., Palo Alto, 1986) pp. 368-369.
- [69] The DØ Collaboration, *The DØ Detector*, FERMILAB-PUB-93/179, 1993, p. 6. (submitted to Nucl. Instr. and Meth.)
- [70] F. Sauli, "Principles of Operation of Multiwire Proportional and Drift Chambers" in *Experimental Techniques in High Energy Physics*, edited by T. Ferbel (Addison-Wesley Publishing Co., Menlo Park, 1987) pp. 79-188.
- [71] R. Fernow, *Introduction to Experimental Particle Physics*, (Cambridge University Press, Cambridge, 1986) pp. 205-258.

- [72] W. R. Leo, *Techniques for Nuclear and Particle Physics Experiments*, (Springer-Verlag, Berlin, 1987) pp. 107-148.
- [73] H. Williams, "Design Principles of Detectors at Colliding Beams" in *Ann. Rev. Nuc. Sci.*, Vol. 36, (Annual Reviews Inc., Palo Alto, 1986) p. 383.
- [74] A. R. Clark *et al.*, *DØ Vertex Drift Chamber, Construction and Test Results*, LBL-31070, p. 1. May 1991 (unpublished)
- [75] A. R. Clark *et al.*, *Nucl. Instrum. and Meth.* **A279** (1989) pp. 243-248.
- [76] The DØ Collaboration, *The DØ Detector*, FERMILAB-PUB-93/179, 1993, p. 7. (submitted to *Nucl. Instr. and Meth.*)
- [77] A. R. Clark *et al.*, *Nucl. Instrum. and Meth.* **A279** (1989) pp. 245.
- [78] J. Butler, *Progress Report from DØ*, DØ internal note # 1559, October 1992 (unpublished)
- [79] G. Finocchiaro, Private communication
- [80] T. Behnke, Ph. D. Thesis, SUNY at Stony Brook, *The Central Drift Chamber for the DØ Experiment: Design, Construction, and Test*, August 1989 (unpublished)
- [81] Dominico Pizzuto, Ph.D. Thesis, SUNY at Stony Brook, *DØ Central Tracking Chamber Performance Studies*, December 1991 (unpublished)
- [82] The DØ Collaboration, *The DØ Detector*, FERMILAB-PUB-93/179, 1993, pp. 10-11. (submitted to *Nucl. Instr. and Meth.*)

- [83] S. Rajagopalan, Ph.D Thesis , Northwestern University. *The dE/dx capabilities of the $D\emptyset$ Tracking System*, June 1992 (unpublished)
- [84] J. Bantly, Ph.D. Thesis, Northwestern University. *The $D\emptyset$ Detector Forward Drift Chamber Performance and Physics Capability in the 1990 FNAL Testbeam Run*, June 1992 (unpublished)
- [85] H. Williams, "Design Principles of Detectors at Colliding Beams" in *Ann. Rev. Nuc. Sci.*, Vol. 36, (Annual Reviews Inc., Palo Alto, 1986) p. 394-396.
- [86] F. Feinstein, Ph.D. Thesis, A'l'Universite de Paris-Sud, Centre d'Orsay. *Etude d'un Detecteur a Rayonnement de Transition pour l'Experience $D\emptyset$ au FNAL*, December 1987 (unpublished)
- [87] R. Yarema, *IEEE Trans. Nucl. Sci. NS-33* (1986) p. 933.
- [88] The $D\emptyset$ Collaboration, *The $D\emptyset$ Detector*, FERMILAB-PUB-93/179, 1993, pp. 11-12. (submitted to Nucl. Instr. and Meth.)
- [89] S. Rajagopalan, Ph.D Thesis , Northwestern University. *The dE/dx capabilities of the $D\emptyset$ Tracking System*, June 1992, p. 43. (unpublished)
- [90] S. Rajagopalan, Ph.D Thesis , Northwestern University. *The dE/dx capabilities of the $D\emptyset$ Tracking System*, June 1992, p. 41-45. (unpublished)
- [91] R. Fernow, *Introduction to Experimental Particle Physics*, (Cambridge University Press, Cambridge, 1986) p. 259.
- [92] C. Fabjan, "Calorimetry in High-Energy Physics" in *Experimental Techniques in High Energy Physics*, edited by T. Ferbel (Addison-Wesley Pub-

- lishing Co., Menlo Park, 1987) pp. 257-324.
- [93] R. Wigmans, *On the Energy Resolution of Uranium and Other Hadron Calorimeters*, CERN/EF 86-18, September 1986 (unpublished)
- [94] J. Yu, Ph.D thesis, SUNY at Stony Brook. *Determination of the Strong Coupling Constant (α_s) and a Test of Perturbative QCD Using $W+Jets$ Processes in the DØ Detector*, August 1993, p. 19. (unpublished)
- [95] The DØ Collaboration, *The DØ Detector*, FERMILAB-PUB-93/179, 1993, p. 15-24. (submitted to Nucl. Instr. and Meth.)
- [96] R. Fernow, *Introduction to Experimental Particle Physics*, (Cambridge University Press, Cambridge, 1986) p. 270.
- [97] S. Rajagopalan, Ph.D Thesis , Northwestern University. *The dE/dx capabilities of the DØ Tracking System*, June 1992, p. 27. (unpublished)
- [98] S. Rajagopalan, Ph.D Thesis , Northwestern University. *The dE/dx capabilities of the DØ Tracking System*, June 1992, p. 26. (unpublished)
- [99] J. Yu, Ph.D thesis, SUNY at Stony Brook. *Determination of the Strong Coupling Constant (α_s) and a Test of Perturbative QCD Using $W+Jets$ Processes in the DØ Detector*, August 1993, p. 22. (unpublished)
- [100] S. Rajagopalan, Ph.D Thesis , Northwestern University. *The dE/dx capabilities of the DØ Tracking System*, June 1992, p. 30. (unpublished)
- [101] S. Rajagopalan, Ph.D Thesis , Northwestern University. *The dE/dx capabilities of the DØ Tracking System*, June 1992, p. 29. (unpublished)

- [102] J. Yu, Ph.D thesis, SUNY at Stony Brook. *Determination of the Strong Coupling Constant (α_s) and a Test of Perturbative QCD Using $W+Jets$ Processes in the $D\emptyset$ Detector*, August 1993, p. 25. (unpublished)
- [103] J. Yu, Ph.D thesis, SUNY at Stony Brook. *Determination of the Strong Coupling Constant (α_s) and a Test of Perturbative QCD Using $W+Jets$ Processes in the $D\emptyset$ Detector*, August 1993, p. 28. (unpublished)
- [104] The $D\emptyset$ Collaboration, *The $D\emptyset$ Detector*, FERMILAB-PUB-93/179, 1993, p. 25. (submitted to Nucl. Instr. and Meth.)
- [105] C. Brown, et al., *Nucl. Instrum. and Meth.* **A279** (1989) p. 331.
- [106] The $D\emptyset$ Collaboration, *The $D\emptyset$ Detector*, FERMILAB-PUB-93/179, 1993, p. 27. (submitted to Nucl. Instr. and Meth.)
- [107] J. M. Butler *et al.*, *Nucl. Instrum. and Meth.* **A290** (1990) pp. 122-130.
- [108] Particle Data Group, “Review of Particle Properties”, *Phys. Rev. D45*, *Part II*, p. III.84 (1992)
- [109] S. Rajagopalan, Ph.D Thesis , Northwestern University. *The dE/dx capabilities of the $D\emptyset$ Tracking System*, June 1992, p. 45-53. (unpublished)
- [110] The $D\emptyset$ Collaboration, *The $D\emptyset$ Detector*, FERMILAB-PUB-93/179, 1993, pp. 32-42. (submitted to Nucl. Instr. and Meth.)
- [111] J. Bantly, Private communication.

- [112] J. Yu, Ph.D thesis, SUNY at Stony Brook. *Determination of the Strong Coupling Constant (α_s) and a Test of Perturbative QCD Using $W+Jets$ Processes in the DØ Detector*, August 1993, p. 31. (unpublished)
- [113] A. Milder, Ph.D thesis, University of Arizona, *Dijet Angular Distributions at $\sqrt{s} = 1800$ GeV Using the DØ Detector*, 1993, p. 53. (unpublished)
- [114] M. Goosens *et al.*, CERN Library Program No. Q100 (Nov. 1991)
- [115] The DØ Collaboration, *The DØ Detector*, FERMILAB-PUB-93/179, 1993, p. 58. (submitted to Nucl. Instr. and Meth.)
- [116] N. Graf, Private communication.
- [117] S. Youssef, “Clustering with Local Equivalence Relations” in *Computer Physics Comm.* **45**(1987) pp. 423-426.
- [118] M. Narain for the DØ Collaboration, *Electron Identification in the DØ Detector*, FERMILAB-Conf-93/054-E, 1993 (unpublished)
- [119] R. Engelmann *et al.*, *Nucl. Instr. Meth.* **216** (1983), p. 45.
- [120] D. Hedin, *D0\$MUON\$UTIL:MUON-ANALYSIS.MEM*, DØ documentation file, March 1992 (unpublished)
- [121] T. Hu, *How to Find the Most Important Measurement in Least-Squares Fit - And Its Application in Muon Momentum Determination at DØ*, DØ internal note # 1811, July 1993 (unpublished)

- [122] S. J. Wimpenny, *The TOP-LEPTONS Analysis Package, Version 5.02*, DØ internal note # 1690, July 1993 (unpublished)
- [123] M. Paterno, *A Monte Carlo Study of the DØ Calorimeter Missing E_T Resolution*, DØ internal note # 1374, March 1992 (unpublished)
- [124] M. Paterno, *A Study of the DØ Calorimeter E_T Resolution Using Low E_T Jet Triggers*, DØ internal note # 1782, July 1993 (unpublished)
- [125] F. Abe *et al.*, (the CDF collaboration), *Dijet Angular Distribution in $p\bar{p}$ collisions at $\sqrt{s} = 1.8$ TeV*, FERMILAB-Pub-92/182-E, 1992 (Submitted to Phys. Rev. Lett.)
- [126] A. Milder, Ph.D thesis, University of Arizona, *Dijet Angular Distributions at $\sqrt{s} = 1800$ GeV Using the DØ Detector*, 1993, p. 76-108. (unpublished)
- [127] U. Heintz, “*Standard*” EM Energy Scale Correction for RECO V10, DØ internal note # 1758, June 1993 (unpublished)
- [128] J. D. Bjorken, “Particle Physics - Where do we go from here?” in *Beam Line*, Vol 22, Num. 4, p. 11. (1992)
- [129] S. Protopopescu, *Event Simulation for Hadron Colliders*, University of DØ proceedings, August 8, 1991 (unpublished)
- [130] V. Barger and R. Phillips, *Collider Physics*, (Addison-Wesley Publishing Co., New York, 1987), p. 399.

- [131] J. C. Collins and T. D. Gottschalk, *Assessment of Perturbative Monte Carlos for Hadron-Hadron Scattering*, Proceedings of Snowmass 86, p. 303.
- [132] T. Sjöstrand, *QCD Monte Carlos*, ?, p. 151.
- [133] G. Altarelli and G. Parisi, *Nucl. Phys.* **B126**, p. 298. (1977)
- [134] H. U. Bengtsson and T. Sjöstrand, *Pythia: The Lund Monte Carlo for Hadronic Processes*, Proceedings of Snowmass 86, p. 311.
- [135] B. Anderson, G. Gustafson, G. Ingelman, and T. Sjöstrand, *Phys. Rep.* **97**, p. 33. (1983)
- [136] R. D. Field and R. P. Feynman, *Nucl. Phys.* **B136**, p. 1. (1978)
- [137] B. R. Webber, “Monte Carlo Simulation of Hard Hadronic Processes” in *Ann. Rev. Nuc. Sci.*, Vol. 36, (Annual Reviews Inc., Palo Alto, 1986) pp. 279.
- [138] T. Sjöstrand, *Z. Phys.* **C26**, p. 93. (1984); *Phys. Lett.* **142B**, p. 420. (1984)
- [139] R. Brun *et al.*, GEANT 3.15 program manual, CERN.
- [140] The DØ Collaboration, *The DØ Detector*, FERMILAB-PUB-93/179, 1993, pp. 56. (submitted to Nucl. Instr. and Meth.)
- [141] J. Womersley, *The DØ Monte Carlo*, DØinternal note # 1520, August 1992 (unpublished)

- [142] J. T. Linnemann, "Triggering the DØ Experiment", in *The Fermilab Meeting DPF92*, Vol. 2, p. 1642. (1992)
- [143] T. Diehl, *Mu Smear Package Documentation*, March 1993 (unpublished)
- [144] A. I. Mincer, P. Nemethy, and A. Boehnlein, *NOISY.DOC* June 1992 (unpublished)
- [145] J. Thompson, Private communication.
- [146] U. Heintz and M. Narain, *A Study of Electron ID Efficiencies Using $Z \rightarrow ee$ Decays*, DØ internal note # 1814, July 1993 (unpublished)
- [147] J. Cochran, *$t\bar{t} \rightarrow dileptons: The Background Bible, Vol. 1.1$* , DØ internal note in preparation (unpublished)
- [148] A. Klatchko *et al.*, *Backgrounds to the top in the $e\mu$ Signature from $W\gamma$* , DØ internal note # 1815, July 1993 (unpublished)
- [149] S. Protopopescu, Private communication.
- [150] T. Huehn, Private communication.
- [151] V. Bhatnagar and J. B. Singh, *Study of Hadron Punchthrough in DØ*, DØ internal note # 1858, August 1993 (unpublished)
- [152] D. Hedin, *Preliminary DØ Punchthrough Rates*, DØ internal note # 1738, June 1993 (unpublished)
- [153] M. Fatyga and D. Chakraborty, *QCD Backgrounds to electroweak signals. A study of fake electron and fake photon probability*, DØ internal

- note # 1753, June 1993 (unpublished)
- [154] M. Fatyga, *A Comparison of Fake Electron Rates in Data and the ISAJET Monte Carlo. Comparison of Multi-jet Triggers with ISAJET Monte Carlo.*, DØ internal note # 1850, September 1993 (unpublished)
- [155] based on: M. Fatyga, Private communication.
- [156] A. Klatchko and S. Youssef, *Backgrounds from External μ -Bremsstrahlung to the $e\mu$ -top Signature in DØ*, DØ internal note # 1769, July 1993 (unpublished)
- [157] J. Cochran, S. J. Wimpenny, and V. Bhatnagar, *Status of Top $\rightarrow e + \mu$ search, 10/4/93*, DØ internal note in preparation (unpublished)
- [158] J. Thompson, Private communication.
- [159] M. Narain, Private communication.
- [160] G. Eppley, *Multiple Interactions, A Primer*, DØ internal note # 1856, August 1993 (unpublished)
- [161] J. Cochran, *$t\bar{t} \rightarrow e\mu$ background studies*, DØ internal note in preparation (unpublished)
- [162] R. Astur, *New Jet Standards: Cuts and Energy Calibration (QCD-JET-CORRECTION routine)*, DØ News, General Folder, Message #1528, July 15, 1993 (unpublished)
- [163] A. Milder, Ph.D thesis, University of Arizona, *Dijet Angular Distributions at $\sqrt{s} = 1800$ GeV Using the DØ Detector*, 1993 (unpublished)

- [164] R. Raja, Private communication.
- [165] U. Heintz, Private communication.
- [166] Particle Data Group, “Review of Particle Properties”, *Phys. Rev. D* **45**, *Part II*, p. III.40 (1992)
- [167] R. Partridge, *Top Limit Calculation*, DØ internal note # 1806, July 1993 (unpublished)
- [168] S. Abachi *et al.* (DØ Collaboration), *Search for the Top Quark in $p\bar{p}$ collisions at $\sqrt{s} = 1.8$ TeV*, (to be submitted Phys. Rev. Lett.)
- [169] F. Abe *et al.* (CDF Collaboration), *Phys. Rev. D* **44**, 30 (1991)
- [170] S. J. Wimpenny, Private communication.
- [171] J. Yu, Private communication.
- [172] J. Ohnemus, *Phys. Rev. D* **44**, 1403 (1991)
- [173] J. Ohnemus, *Phys. Rev. D* **44**, 3477 (1991)
- [174] J. Smith, D. Thomas, W.L. van Neerven, *Zeit. Phys. C* **44**, 267 (1989)
- [175] V. Barger and R. Phillips, *Collider Physics*, (Addison-Wesley Publishing Co., New York, 1987), p. 380.
- [176] F. Abe *et al.* (CDF Collaboration), *Measurement of the e^+e^- Invariant Mass Distribution in $\bar{p}p$ Collisions at $\sqrt{s} = 1.8$ TeV*, FERMILAB-PUB-91/169-E, 1991 (unpublished)

[177] R. K. Ellis and W. J. Sterling, *QCD and Collider Physics*, FERMILAB-Conf-90/164-T, 1990, p. 84,85 (unpublished)

[178] B. Adeva *et al.*, *Phys. Lett.* **261B**, 177 (1991)